The Thesis Committee for Fiona S. Cheung
certifies that this is the approved version of the following thesis:

Diffusion of Airborne Sound Using Acoustic Metamaterials

APPROVED BY

SUPERVISING COMMITTEE:

Michael R. Haberman, Supervisor

Preston S. Wilson, Co-Supervisor

Diffusion of Airborne Sound Using Acoustic Metamaterials

by

Fiona S. Cheung

THESIS

Presented to the Faculty of the Graduate School of

The University of Texas at Austin

in Partial Fulfillment

of the Requirements

for the Degree of

MASTER OF SCIENCE IN ENGINEERING

THE UNIVERSITY OF TEXAS AT AUSTIN

August 2018

Acknowledgments

First, I would like to thank my advisor, Dr. Michael Haberman, for his guidance, insight, and advice throughout this process, and for allowing me the opportunity to learn from him and work with him. I would like to thank my co-advisor, Dr. Preston Wilson, for his advice and encouragement throughout my graduate school career. If he hadn't planted the seed during his undergraduate acoustics class, I most likely would not have pursued a graduate education in acoustics. Thank you for that, and for encouraging me to apply to the acoustics program when I was considering graduate school.

Thank you to my fellow classmates in the UT Acoustics program for their friendship and encouragement, and for keeping me sane through all the stressful assignments and exams. Shout out to Ben Goldsberry for all the fun discussions in the office and for always helping me with my COMSOL models when I was banging my head against the wall. A very special thank you to Brian McCrory for all his love, support, encouragement, and patience through all the stressful times in graduate school, and for always supporting me in all my endeavors. I couldn't have done it without you.

Finally, I would like to acknowledge financial support from the Multidisciplinary University Research Initiative of the Office of Naval Research (Grant No. N00014-13-1-0631), which allowed me to complete this research.

Diffusion of Airborne Sound Using Acoustic Metamaterials

Fiona S. Cheung, M.S.E.
The University of Texas at Austin, 2018

Supervisors: Michael R. Haberman
Preston S. Wilson

Acoustic surface treatments, such as absorbers and diffusers, are used to control unwanted reflections in rooms. These reflections, when excessive, can create an unpleasant experience for both audiences and performers in any space, not just performance spaces. Existing acoustic absorbers, including Helmholtz resonators, quarter-wave resonators, and panel absorbers, are discussed in this thesis. The most common diffuser, the Quadratic Residue Diffuser (QRD), is also explored in detail. While QRDs are well known for their predictability and ease of design, they suffer from two main drawbacks: size and aesthetics. This thesis explores the use of acoustic metamaterials, specifically coiled space metamaterials, to replace the QRD. These metamaterials seek to address these specific problems with QRD designs while replicating its ability to scatter acoustic waves in a predictable fashion. Two specific coiled space metamaterial designs are discussed in detail, and their responses

are compared to that of the QRD to determine whether they can be viable replacements. The results of the comparisons, while unable to replicate the response of the standard QRD exactly, did show modest improvements. More validation must be done before a definitive answer can be given as to whether either of these designs are able to be successful replacements for the QRD.

Table of Contents

List of Tables

List of Figures

Chapter 1

Introduction

In enclosed spaces such as rooms, sound can arrive at a listener from all directions. In these spaces, a listener hears a combination of sound coming directly from a source and sound that has been reflected back by other objects. This sometimes results in unwanted echoes caused by sound reflecting off the walls, floors, or ceiling of the room. For example, large rectangular rooms, such as gymnasiums, suffer from an abundance of echoes that are a result of reflections bouncing between the various rigid surfaces in the room, making it extremely hard to understand speech in the room. Another example would be a performance venue where artists perform in front of their audience. Behind the audience, one often finds a curved back wall which focuses the reflected waves back to the performer, as shown in Fig. 1.1. Other than taking the costly step of changing the shape of the rooms in both these examples, how can these issues be fixed?

A large flat surface, such as a wall, is known to produce a specular reflection of any acoustic signal that encounters it. When the wall is rigid, it reflects the same amount of energy back into the space, and follows the law of specular reflection, which states that the angle of reflection, θ_r, must equal

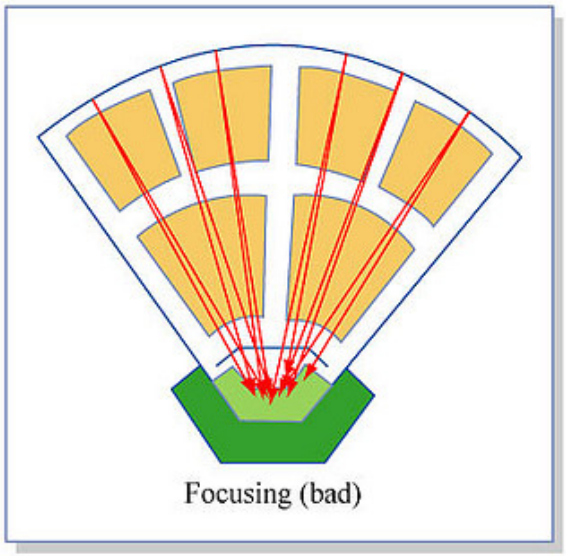

Figure 1.1: Focusing effect in an auditorium with a curved back wall. Figure adapted from [2].

the angle of incidence, θ_i [1]. The incident angle is defined as the angle of the incident wave relative to a line normal to the surface, as shown in Fig. 1.2. An excess amount of specular reflections is one of the root causes of the undesirable sound quality associated with the previous examples. The most common way to fix these issues are to add acoustic surface treatments to the surfaces of the room. These treatments usually fall in one of two categories: absorbers and diffusers. While both can be used to control unwanted reflections, their method of doing so is different, as illustrated in Figure 1.3.

An acoustic absorber reduces the amount of sound reflected into the room from an incident wave, but does not change the angle of reflection. Absorbers are used most often in noise control situations, such as the gymnasium

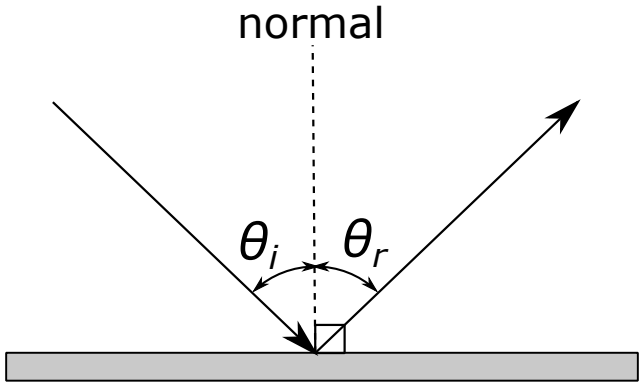

Figure 1.2: Law of specular reflection: $\theta_i = \theta_r$.

described above, where the primary objective is to reduce the reverberation and sound level when many sources of noise are present in the space.

In contrast, an ideal acoustic diffuser will reflect the same amount of sound back into the room, but will scatter the sound in multiple directions instead of specularly, thereby reducing unwanted reflections caused by flat surfaces, such as walls or ceilings. Diffusers use spatial variations on the surface to change the phase of reflected sound as a function of position on the surface. A diffuser would be used in the auditorium example where a smooth wall focused sound towards the performer on stage. Adding a diffusing surface would reduce or eliminate focusing without decreasing the amount of sound in the room.

This thesis will attempt to answer whether coiled space metamaterials are capable of replicating the performance of a standard Quadratic Residue Diffuser (QRD) while addressing the drawbacks of the design. Chapter 2 provides an overview of acoustic surface treatments, starting with absorbers

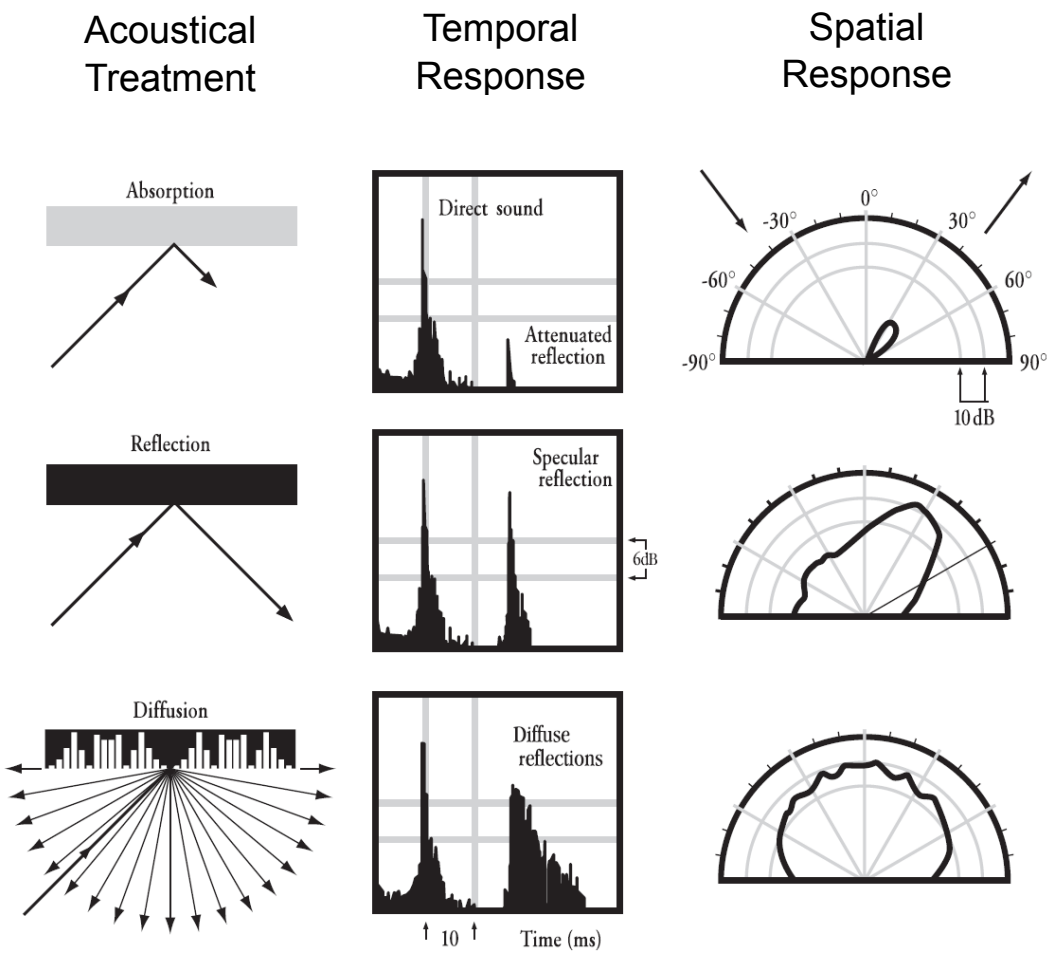

Figure 1.3: Temporal and spatial characteristics of absorbing, specularly reflecting, and diffusing surfaces. Figure adapted from Cox and D'Antonio [3].

and followed by a discussion on diffusion and the most common diffuser: the Quadratic Residue Diffuser. QRDs struggle with certain issues - namely, they must be very large in order for them to work at low frequencies. They can also be aesthetically displeasing, and thus may not always fit in with the decor of a specific room due to their blocky and uneven surface. The work reported in this thesis begins to address these issues using acoustic metamaterials, which are artificially structured materials that are engineered to produce properties that are not found in nature. Current metamaterials absorber and diffuser designs will be discussed at the beginning of Chapter 3, before delving into two specific designs that will attempt to replicate the response of the QRD. These two designs are used to design a metamaterial QRD, and a finite element simulation was used to determine the response of each metamaterial QRD. These responses are compared against the simulated response of the standard QRD. While neither metamaterial QRD is able to replicate exactly the response of the standard QRD, both metamaterial QRDs responses show improvements over the standard QRD response. In addition, 3D printed unit cells are tested experimentally in a plane wave impedance tube, which captured the reflected field of each individual metamaterial unit cell. These results are compared to simulated results to determine the accuracy of the simulations, which show that significant losses are present in the experiment that are not captured accurately in the simulations. Chapter 4 presents a set of conclusions from the results discussed in Chapter 3, and provides a set of recommendations for future work.

Chapter 2

Acoustic Surface Treatments

There are two main types of acoustic surface treatment: absorbers and diffusers. Absorbers remove energy from a room, whereas diffusers scatter the energy in multiple directions without removing significant energy. Before considering types of absorbers, it is useful to discuss how their performance is measured. An absorption coefficient, (α), defined as the ratio of absorbed acoustic power divided by the incident acoustic power, is used to represent the amount of absorption, from no absorption ($\alpha = 0$) to complete absorption ($\alpha = 1$). Absorption varies by frequency, thus absorption coefficient is also a function of frequency.

Absorbers can usually be separated into two categories: porous absorbers and resonant absorbers. This chapter will give a brief overview of porous absorbers, while focusing more in depth on resonant absorbers. The last section will be devoted to diffusion and the most common diffuser: the Quadratic Residue Diffuser.

2.1 Porous Absorbers

Porous absorbers are the most common type of absorber. These absorbers are made of materials that have holes that are tiny compared to a wavelength, and produce losses through friction as sound waves propagate through the material due to viscous boundary layer effects, decreasing the amount of energy being reflected back into the room [4]. The most common types of porous materials include fiberglass, mineral fiber (Fig. 2.1), and fiberboard, though there are many others.

Because it is rather complicated to measure the exact impedance of a porous absorber, a metric called flow resistance, r_f, is used to determine the resistive component of the impedance [4]. While r_f is dependent on thickness of the material, specific flow resistance, r_s, is not and is thus a fundamental property of the material. Materials can be compared using this metric.

Because a porous absorber uses friction to generate loss, it is most effective when placed where the particle velocity is high. A rigid-backed absorber will generate little absorption close to the rigid boundary, as the particle velocity there vanishes. Thus, a thicker panel will be more effective than a thin one, as illustrated in Fig. 2.2. According to [3], a material must be at least "a tenth of a wavelength thick to cause significant absorption and a quarter of a wavelength to absorb all the incident sound."

Since the material closest to the rigid backing is ineffective, a simple way to increase the absorption is by merely moving the absorber further from

Figure 2.1: Mineral Fiber Insulation - Figure adapted from Aurelex Acoustics, Inc. website (www.auralex.com).

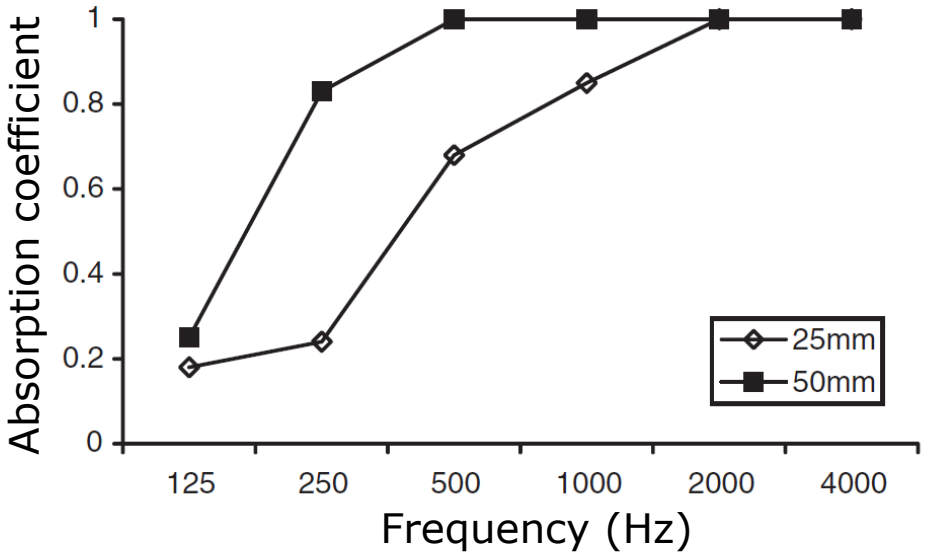

Figure 2.2: Random incidence absorption coefficient for mineral wool of two different thicknesses with a rigid backing. Figure adapted from Cox and D'Antonio [3].

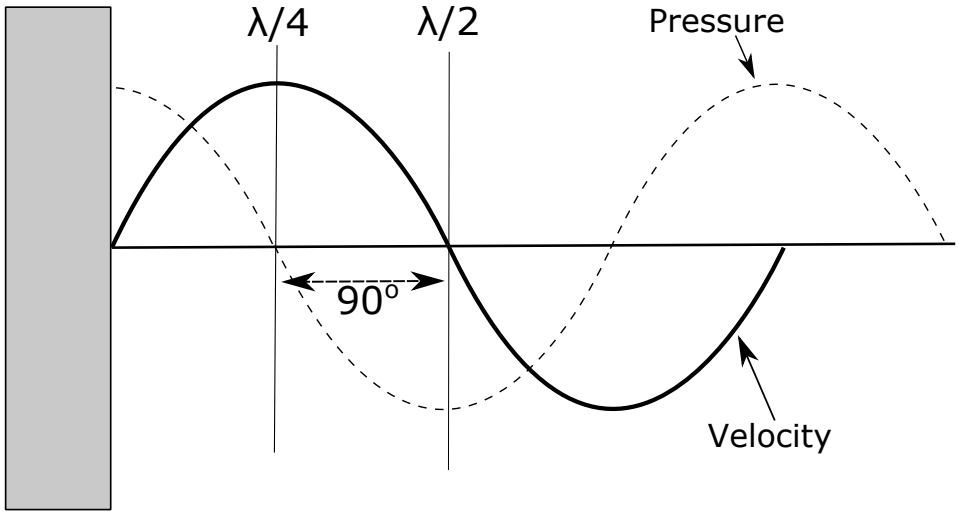

Figure 2.3: Pressure and velocity waveform near a rigid surface. At $\lambda/4$, the velocity is at a maximum, and thus the absorption of a porous absorber will be at a maximum.

the backing. As shown in Fig. 2.3, the velocity is at a maximum a quarter of a wavelength from a rigid surface. Placing a porous absorber a quarter wavelength away from the wall will produce the most absorption.

While porous absorbers are able to produce broadband absorption over higher frequencies (Fig. 2.2), they are ineffective absorbers at low frequencies. In order for porous absorbers to be effective at low frequencies, they must either be quite thick, or placed a significant distance from the wall. For this reason, porous absorbers are not generally used as low frequency absorbers. They can, however, be used in conjunction with resonant absorbers. Their effect on the performance of resonant absorbers is discussed in the next section.

2.2 Resonant Absorbers

Resonance is a phenomenon that is commonly used to absorb sound or mechanical energy. Two main types of resonant absorbers will be discussed: Helmholtz resonators, and quarter-wave resonators. Helmholtz resonators can come in different forms, some of which will be discussed here.

2.2.1 Helmholtz Resonators

The Helmholz resonator was named after German physicist Hermann von Helmhotz. The most general case consists of a closed cavity with a neck (Fig. 2.4). In the limit where the neck length, l, and the descriptive length of the cavity, $L = \sqrt[3]{V}$, are much smaller than the wavelength of sound in air, the closed cavity acts as a spring, and the air in the neck acts as a mass, creating a simple oscillator. The equation for the input impedance of a Helmholtz resonator is [1]:

$$Z_{\mathrm{HR}} = \rho_0 c_0 (ka)^2 + j\omega\rho_0 \left(l' - \frac{S_{\mathrm{HR}} c_0^2}{\omega^2 V} \right), \tag{2.1}$$

where ρ_0 is the density of air, c_0 is the speed of sound in air, w is the angular frequency ($\omega = 2\pi f$), k is the wavenumber ($k = \omega/c_0$), S_{HR} is the cross-sectional area of the neck, and l' is the effective length of the neck.

Notice that the impedance of the Helmholz resonator depends on the term l', defined as the effective length of the neck. A short open tube, such as the neck of the Helmholtz resonator, may be approximated as having a pressure release termination at the end of the tube. However, the effect of

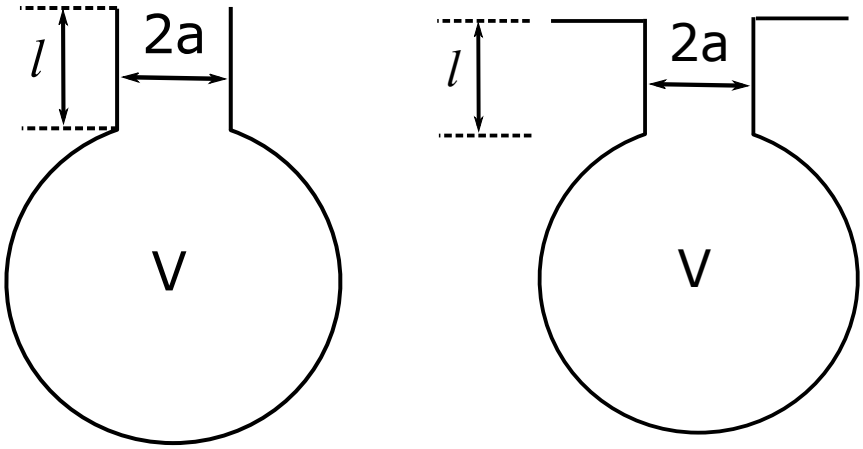

(a) unflanged (b) flanged

Figure 2.4: Helmholtz resonators configurations.

radiation must be considered. Though most of the pressure at the end of the tube is reflected back down the tube as in a pressure release boundary, some of it is radiated into the outside fluid, which can be approximated as a small layer of fluid oscillating at the end of the tube like a mass. This is the end correction for an open tube. For a tube with radius a, the effective length of the tube, l', is the length of the tube plus the end correction: [1]

$$l' = l + \Delta l, \tag{2.2}$$

where

$$\Delta l = 0.6133a \tag{2.3}$$

for an unflanged tube (Fig. 2.4a), and

$$\Delta l = 0.85a \tag{2.4}$$

for a flanged tube (Fig. 2.4b).

Now that the effective length of the neck has been calculated, the resonance frequency can be found when the reactive part of the impedance in Eq 2.1 equals zero [1],

$$f_{\text{res}} = \frac{c_0}{2\pi}\sqrt{\frac{S_{\text{HR}}}{l'V}}. \tag{2.5}$$

Thus, the resonance frequency depends on the cross-sectional area of the neck, the length of the neck, and the volume of the cavity.

The reflection coefficient, R, is related to the normal incidence input impedance, Z_{n}, by

$$R = \frac{Z_{\text{n}} - \rho_0 c_0}{Z_{\text{n}} + \rho_0 c_0}, \tag{2.6}$$

and the absorption coefficient, α, is related to R by [4]

$$\alpha_{\text{n}} = 1 - |R|^2, \tag{2.7}$$

which can be written in terms of its components as [4]

$$\alpha_{\text{n}} = \frac{4\rho_0 c_0 w_{\text{n}}}{(w_{\text{n}} + \rho_0 c_0)^2 + x_{\text{n}}^2}, \tag{2.8}$$

where w_n is the real part of the impedance, and x_n is the imaginary part of the impedance given in Eq. 2.1:

$$Z_{\text{n}} = w_{\text{n}} + jx_{\text{n}}. \tag{2.9}$$

The absorption of a Helmholz resonator is at its peak at its resonance frequency and decreases sharply away from resonance. However, placing porous material inside the cavity of the resonator changes the response. Figure 2.5 shows the effect that damping has on the absorption. The flow resistivity

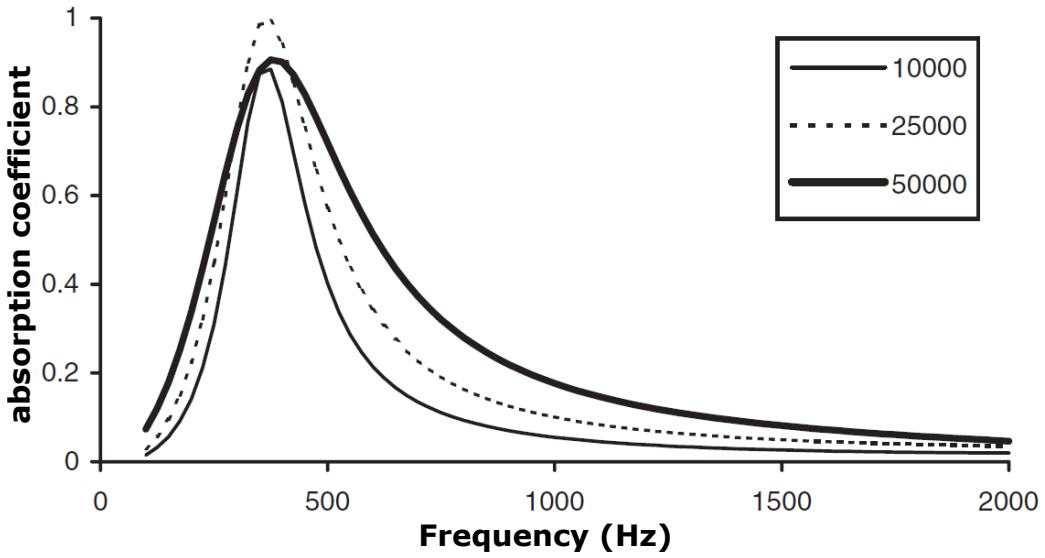

Figure 2.5: Effect of damping on the absorption of a Helmholtz resonator. Values in the legend are in Rayls $\cdot$ m^{-1}. Figure adapted from Cox and D'Antonio [3].

of 25,000 Nm^{-4}s produces the most damping due to the fact that it is closest to the characteristic impedance of air [3]. Values above it produce a more broadband response but reduce the maximum absorption, whereas values under it reduce both the bandwidth and maximum absorption.

One common approach to increase the absorption coefficient in rooms over a narrow frequency band is to create walls that contain arrays of Helmholtz resonators (HR). A schematic of such a wall is shown in Fig. 2.6. The HRs have an opening area of $S = \pi a^2$, a neck length of h, and a volume, V. The HR openings cover an area fraction of the wall defined as $\phi = S_{\text{HR}}/L^2$. The input impedance for just the HR is given in Eq. 2.1.

Assuming that the area averaged pressure for all y and z is constant,

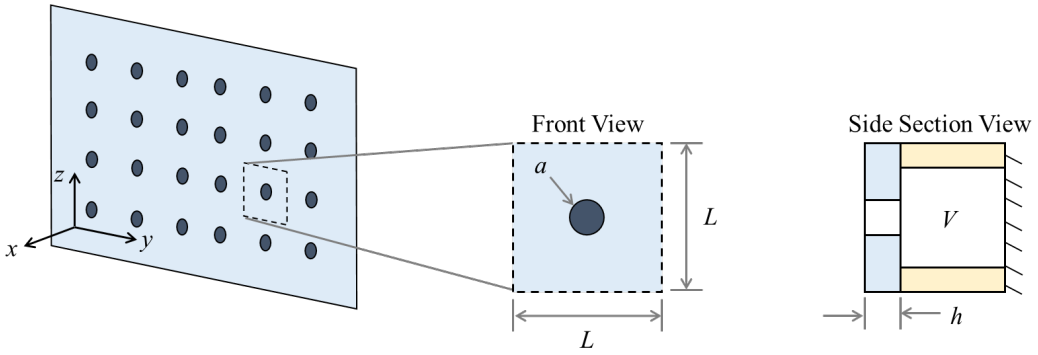

Figure 2.6: Schematic of a wall containing an array of Helmholtz resonators.

the approximate normal incidence input impedance for the system at $x = 0$ is simply

$$Z_{\mathrm{n}} = \frac{1}{\phi} Z_{\mathrm{HR}}. \tag{2.10}$$

The real and imaginary components are thus

$$w_{\mathrm{n}} = \frac{\rho_0 c_0 (ka)^2}{\phi} \tag{2.11}$$

and

$$x_{\mathrm{n}} = \frac{\omega \rho_0 l'}{\phi} \left(1 - \frac{S_{\mathrm{HR}} c_0^2}{\omega^2 V l'} \right), \tag{2.12}$$

which can be substituted into Eq. 2.8 to obtain the absorption coefficient. The resonance frequency occurs when $x_{\mathrm{n}} = 0$:

$$f_0 = \frac{c_0}{2\pi} \sqrt{\frac{S}{l'V}}. \tag{2.13}$$

Let this wall contain an array of HRs with a radius of $a = 1.5$ cm, a neck length of $h = 6.3$ cm, and volume of $V = 1.56\mathrm{E}{-5}$ m^3. Let the HR opening cover an area fraction of the wall, $\phi = 12.5\%$. Figure 2.7 shows the absorption coefficient of the wall normalized to the resonance frequency.

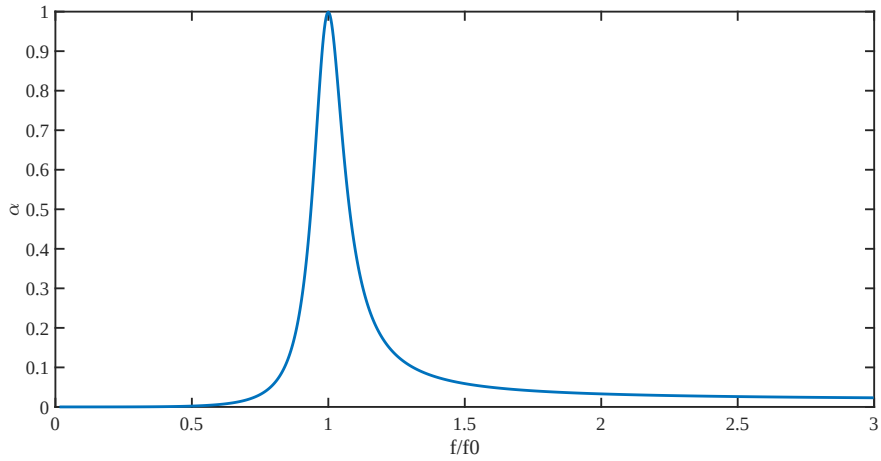

Figure 2.7: Absorption coefficient versus normalized frequency of a wall containing an array of HRs.

Clearly, this wall produces perfect absorption at resonance, but the absorption drops sharply away from resonance. One example of a situation in which this type of wall would be used is in a room that has a unwanted standing wave at a specific frequency or narrow range of frequencies. If tuned correctly, this HR wall could absorb and remove the standing wave from the room.

As shown in this section, Helmholtz resonators are versatile absorbers that can be used in a variety of situations and configurations. The most general case of the HR was shown in Fig. 2.4, but there are many other configurations that act in a similar manner. The following sections will examine several other common configurations of Helmholtz resonators.

2.2.1.1 Panel Absorbers

Panel absorbers refer to nonporous panels used as absorbers, which absorb sound simply due to induced motion. A sound wave incident on a panel absorber causes the panel to move by transferring part of its energy to the panel. For this reason, even walls and windows can act as absorbers, though their absorption is typically small [4].

Like porous absorbers, panel absorbers are often placed in front of an air gap backed by a solid surface, as shown in Fig. 2.8. As long as the panel is allowed to move freely without coming into contact with the surface, this system acts as a mass-spring damper, similar to a Helmholtz resonator, in which the panel as the mass and the air gap behind it as the spring. When the depth, d, of the airspace is small compared to a wavelength, the impedance of a panel absorber placed in front of a rigid surface with no contact between the panel and the surface is [4]

$$z = r_f + j\left[\omega m - \frac{\rho_0 c_0^2}{\omega d}\right], \tag{2.14}$$

where m is the mass of the panel. The resonance frequency can be calculated from this equation, which occurs when the imaginary terms are equal [4]:

$$\omega_0 = \sqrt{\frac{\rho_0 c_0^2}{md}} \tag{2.15}$$

This equation looks very similar to the resonance frequency equation for Helmholtz resonators, implying that panel absorbers act similarly. Like HRs, panel absorbers are able to produce significant absorption close to the resonance fre-

quency, but the absorption decreases significantly away from it. Porous material can be added behind the panel in the air gap to increase damping, which in turn broadens the absorption peak, as seen with Helmholtz resonators.

Bass traps are a common form of panel absorbers. They consist of wood panels mounted over an air cavity with a porous material inside. They are used most often in small spaces to control standing waves by converting the high pressure fluctuations in the corners and near the walls into absorption for specific frequency ranges. The resonance frequency is often hard to predict, however, for many reasons. For instance, in [3], Cox and D'Antonio state that "the physical mass of the membrane is often different from the vibrating acoustic mass due to mounting conditions." Figure 2.9 shows the measured and predicted absorption coefficient of a bass trap placed in the corner of a small studio room.

In the previous sections, it has been shown that porous absorbers excel as high frequency broadband absorbers. Helmholtz resonators can produce high absorption around the resonance frequency, but panel absorbers are more typically used as low frequency absorbers due to its greater mass, which lowers the resonance frequency. This next section will discuss perforated panels, which when backed by porous materials and a rigid surface, act as decent mid-frequency absorbers [4].

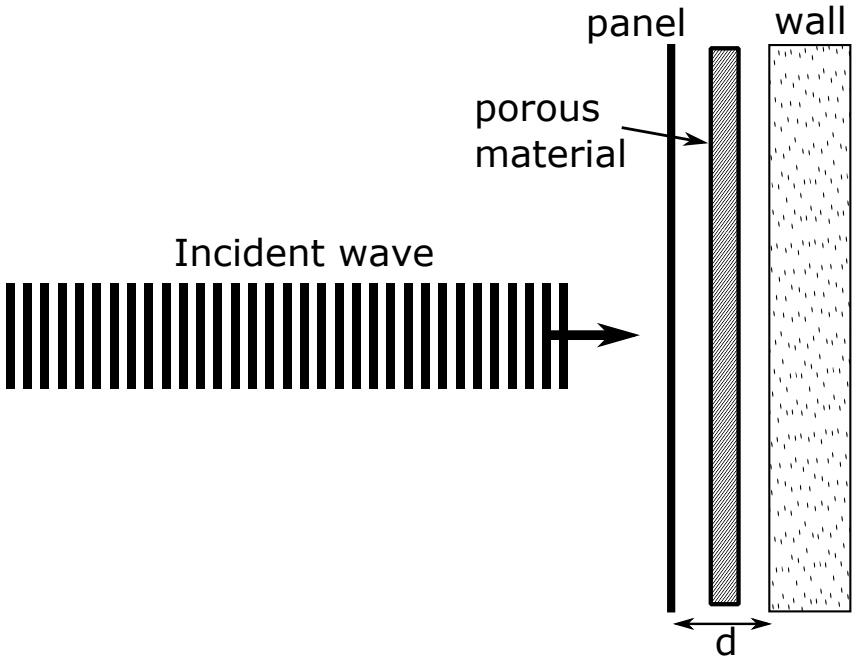

Figure 2.8: Diagram of a panel absorber with an air gap backed by a wall.

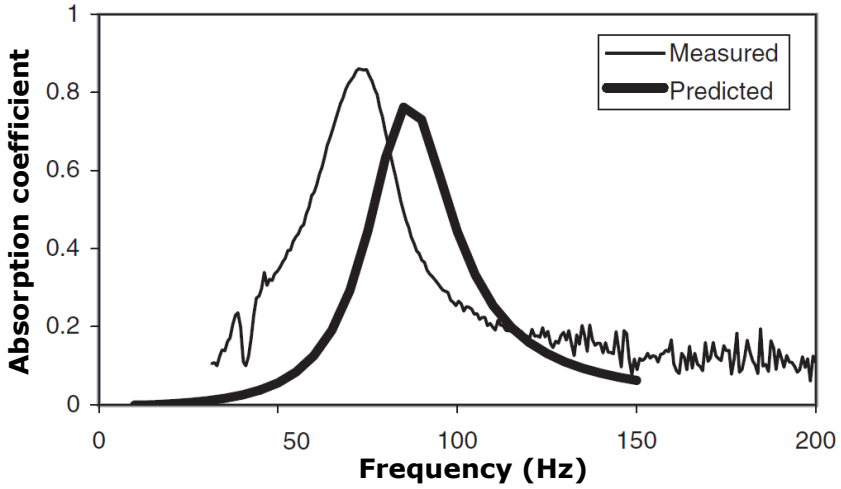

Figure 2.9: Absorption coefficient of a bass trap showing the absorption peak due to resonance. This figure also illustrates the difficulty in predicting the resonance frequency by comparing the predicted and measured absorption coefficients. Figure adapted from Cox and D'Antonio [3].

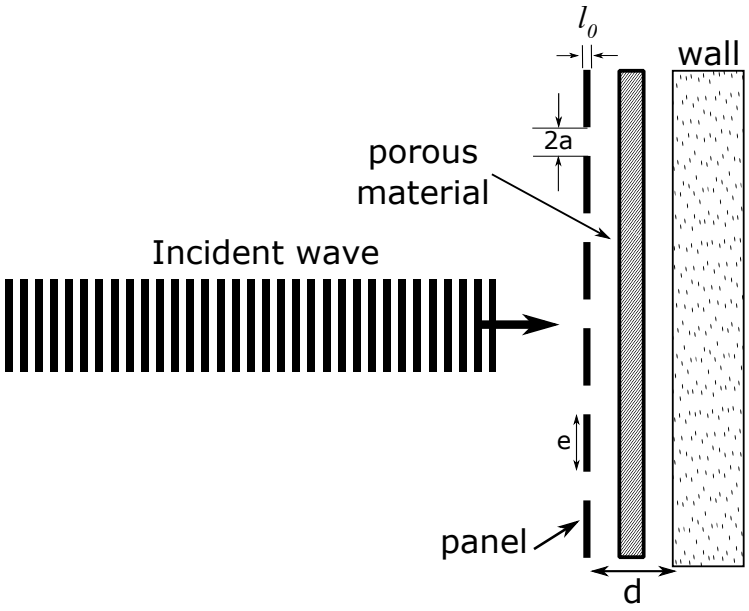

Figure 2.10: Diagram of a panel absorber with an air gap backed by a wall.

2.2.1.2 Perforated Panel Absorbers

Perforated panels (Fig. 2.10) act much the same as non-perforated panels, except that the added mass of the air moving through the perforations must also be considered. This added mass can be viewed as little tubes of air. Figure 2.10 shows a perforated plate with holes that are spaced a distance e apart with radii of a. From [4], the mass per unit area is

$$m_c = \frac{\rho_0 l'}{\sigma}, \tag{2.16}$$

where σ is porosity of the plate,

$$\sigma = \frac{\pi a^2}{e^2}. \tag{2.17}$$

Notice again that the mass depends on the term l', the effective length. This is the same end correction as discussed before in the Helmholz resonator section.

Since holes in a perforated plate are flanged on both sides, the effective length is [1]

$$l' = l_0 + 2(0.85). \tag{2.18}$$

Equation 2.16 assumes that the air mass is much smaller than the mass of the panel. If the perforations are large and the panel mass is small, the air mass must then be taken into consideration, and the combined mass, m_c is thus

$$m_c = m\frac{M}{M+m}, \tag{2.19}$$

where M is the mass of the panel, and m is the mass of the air in the perforations.

For a perforated panel with porous material backed by a rigid surface, the impedance is the same as a regular panel, except the mass, m, is replaced with m_c in Eq. 2.14. This yields [4]

$$z = r_f + j\left[\omega m_c - \frac{\rho_0 c_0^2}{\omega d}\right]. \tag{2.20}$$

Since the only difference is the combined mass term, the resonance frequency is similar to that of the panel absorber [4]:

$$\omega_0 = \sqrt{\frac{\rho_0 c_0^2}{m_c d}}. \tag{2.21}$$

Recall that m_c in Eq. 2.16 is related to the tube length when the air mass is much smaller than the panel mass. If Eq. 2.16 is replaced with Eq. 2.17, then [4]

$$m_c = \frac{\rho_0 l'}{\sigma} = \frac{\rho_0 l' e^2}{\pi a^2} = \frac{\rho_0 l' V}{Sd}, \tag{2.22}$$

and the resonance frequency, Eq. 2.21, becomes [4]

$$\omega_0 = c_0\sqrt{\frac{S}{l'V}}, \tag{2.23}$$

where $S = \pi a^2$ and $V = e^2 d$. This is the same equation for the resonance frequency of a Helmholtz resonator, shown in the previous section, implying that a perforated plate behaves like a Helmholtz resonator.

Comparing the equations for the resonance frequencies of the solid and perforated plates (Eq. 2.15 and Eq. 2.21), it is clear that they are the same. The main difference lies in their mass. The addition of the perforations creates a much ligher panel, thus moving the resonance frequency higher, making a perforated plate more useful for absorption in the mid-frequency range.

A special type of perforated panel absorber is the micro-perforated panel absorber. These panels have very small holes, such that the boundary layer viscous losses must be considered. They therefore provide absorption through these viscous losses [3]. Because they have built-in damping, they eliminate the need for absorptive material between the perforated plate and the backing, and enable things like transparent absorbers. Micro-perforated absorbers also seem to be more robust than porous absorbers, and the vibrating air in their pores makes it less likely to become clogged in dusty environments [5].

Helmholtz resonators are one of the most common types of resonators used in acoustic surface treatments. Another type of resonator which produces absorption in a very different matter, the quarter-wave resonator, will

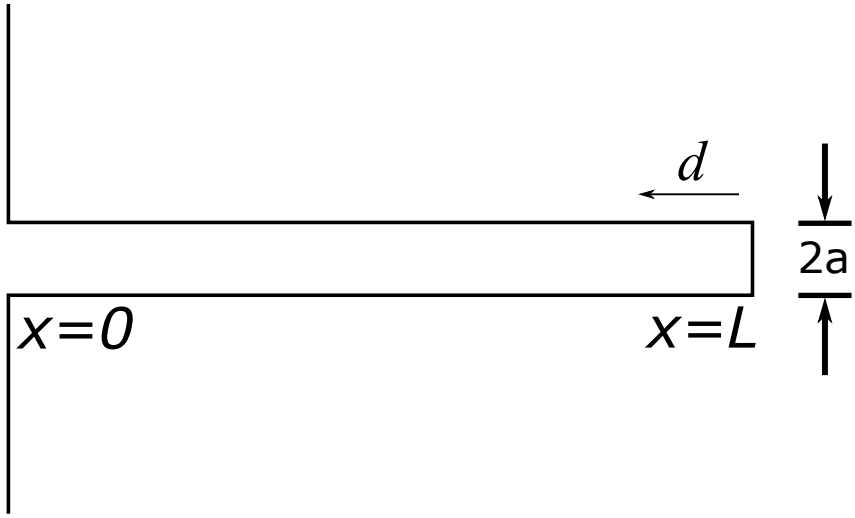

Figure 2.11: Geometry of a quarter-wave resonator.

be discussed in the following section.

2.2.2 Quarter-Wave Resonators

A quarter-wave resonator absorbs sound by radiating a wave that is 180° out of phase with the incident wave, thus canceling it out. The depth of the well is a quarter of the wavelength of the incident wave, thus causing the reflected wave to be exactly half a wavelength out of phase from the incident wave, creating a perfect absorber. The quarter-wave resonator in Fig. 2.11 has a length, L, and radius, a. Assume that it has rigid walls, that the cross sectional area, $S = \pi a^2$, is small compared to the wavelength, λ, of the incident wave, and that thermoviscous losses are ignored. Let the distance, d, represent an arbitrary point some distance from the termination.

$$d = L - x. \tag{2.24}$$

Let [1]

$$p(x,t) = P(x)e^{jwt} \tag{2.25}$$

and

$$u(x,t) = U(x)e^{jwt}, \tag{2.26}$$

where the amplitudes P and U are complex phasors. A tube with a rigid termination, where $u(x = L, t) = 0$, has a reflection coefficient, $R = 1$. Thus, the expressions for P and U become [1]:

$$P = P_i(e^{jkd} + e^{-jkd}) \tag{2.27}$$

and

$$U = U_i(e^{jkd} - e^{-jkd}), \tag{2.28}$$

where P_i and U_i refer to the incident pressure and particle velocity, respectively. By dividing Eq. 2.27 by Eq. 2.28, the impedance of the closed tube is found to be

$$Z = -jZ_0\cot(kL), \tag{2.29}$$

where $Z_0 = \rho_0 c_0$ is the impedance of the background fluid, air. Combining Eq. 2.25 with Eq. 2.27,

$$p = P_i(e^{jkd} + e^{-jkd})e^{jwt}. \tag{2.30}$$

From Euler's formula, it is well known that

$$\cos(x) = \frac{e^{jx} + e^{-jx}}{2}, \tag{2.31}$$

thus Eq. 2.30, combined with Eq. 2.24, can be rewritten as

$$p(x) = 2P_i \cos[k(L - x)]. \tag{2.32}$$

At the other end of the tube, a pressure release boundary exists, which requires that

$$p(x = 0, t) = 0. \tag{2.33}$$

In order to satisfy this boundary condition, Eq. 2.32 becomes

$$p(0, t) = 0 = 2P_i \cos(kL). \tag{2.34}$$

In order for this to be true,

$$\cos(kL) = 0, \tag{2.35}$$

which occurs when

$$kL = \frac{(2n-1)\pi}{2}, \tag{2.36}$$

where $n = 1, 2, 3...$ Solving for the values of L at which this occurs,

$$\begin{aligned} k &= \frac{2\pi}{\lambda}, \\ \frac{2\pi L}{\lambda} &= \frac{(2n-1)\pi}{2}, \\ L &= \frac{(2n-1)\lambda}{4}. \end{aligned} \tag{2.37}$$

Resonance therefore occurs at odd integral multiples of a quarter wavelength of the incident wave frequency. At these lengths, the impedance everywhere in the tube is purely reactive and the intensity is zero, because the intensity of the backwards traveling wave is equal and opposite to that of the

incident wave, creating a situation where the net energy flow is zero [1]. No sound is reflected back out of the tube, creating a perfect absorber at those frequencies.

2.3 Quadratic Residue Diffusers

Before considering diffusers, it is useful to describe the notion of "diffuse." First, consider a room that is not diffuse. A rectangular room often has dimensions such that standing waves, or normal modes, develop at resonance frequencies. These are self-reinforcing waves that combine in phase as they bounce from one wall to an opposite wall. Other frequencies are not nearly as strongly amplified, and hence are present, but at significantly lower amplitude than the standing waves, which can persist long after the sound source is removed. These modes can persist in multiple directions, depending on the dimensions of the room.

In contrast, a room that is diffuse has a sufficient density of modes, and is referred to as a diffuse field. In [4], Long describes a diffuse field as "one in which there is an equal energy density at all points in the room... [and] implies that there is an equal probability that sound will arrive from any direction." One way to accomplish this is to use diffusers.

Diffusers aim to break up reflections by scattering the energy over an area instead of directly back in the direction of the incident wave. They are useful in controlling standing waves and echoes, but they are most often used in concert halls, where the desire is to limit discrete reflections, and instead

scatter them to fill the hall. An ideal diffuser distributes the sound evenly in all directions, and diffusers can come in all shapes and sizes. In the past, ornate architectural details on the walls of some concert halls, such as the Musikverein in Vienna, contributed to the diffusion of sound, and has made the Musikverein world-renowned as one of the best sounding concert halls in the world. However, the biggest problem with this was that it wasn't predictable; these ornate details were different for every hall, and there was no way to predict how they would work.

M.R. Schroeder invented the diffuser that is now named after him, the Schroeder diffuser, in the 1970s. Using number theory, Schroeder created diffusers that are based on a mathematical sequence, and are thus both predictable and easy to design. While there are many mathematical sequences that can be used for the Schroeder diffuser, such as the maximum length sequence, the primitive root sequence, and a complex Legendre sequence based on the index function [3], this thesis will focus on the most common sequence: the quadratic residue sequence, on which the Quadratic Residue Diffuser is based.

Quadratic Residue Diffusers (QRDs), like all of Schroeder's diffusers, consist of a series of blocks of same width but heights that vary with in-plane position. These can also be considered a series of wells instead of blocks, where the depths of the wells are determined by the quadratic residue sequence, s_n. QRDs are periodic devices; they use periodicity to achieve the optimal scattering effect; this will be discussed in greater detail later in this chapter.

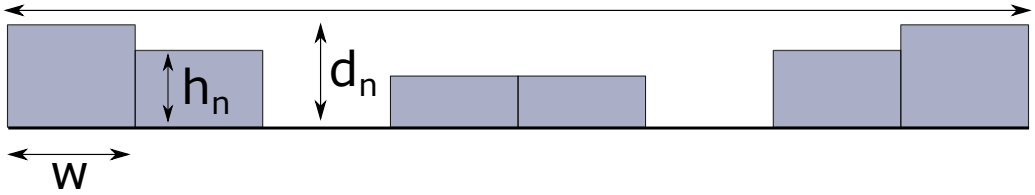

Figure 2.12: Cross section of 1 period of a 1D QRD with N=7.

Because the QRD is a periodic device, the letter N is used to describe the number of wells per period. A $N = 7$ QRD has 7 blocks or wells per period, as shown in the cross sectional view of a QRD in Fig. 2.12. Due to the periodic nature of the QRD, the width of the individual well must be chosen such that total width of one period of the QRD is greater than the wavelength of the design frequency, λ_0. In other words,

$$wN \geq \lambda_0. \tag{2.38}$$

Additionally, as the well width becomes narrower, viscous losses start to become significant and absorption can occur. In order to avoid this, practically, the well width must be at least 25 mm to avoid viscous losses and absorption for any QRD [3].

A 1D QRD (Fig. 2.13a) diffuses sound in only a single plane; in the other direction, the QRD behaves as a flat surface and generates a specular reflection of the incident plane wave. Because of this, it is typical to only consider a cross section of a 1D QRD, as shown in Fig. 2.12. A 2D QRD scatters in 2 planes (Fig. 2.13b). These will be discussed in detail in the following sections. Inverse QRDs, which scatter sound that is 180° out of phase with a normal QRD, will also be considered.

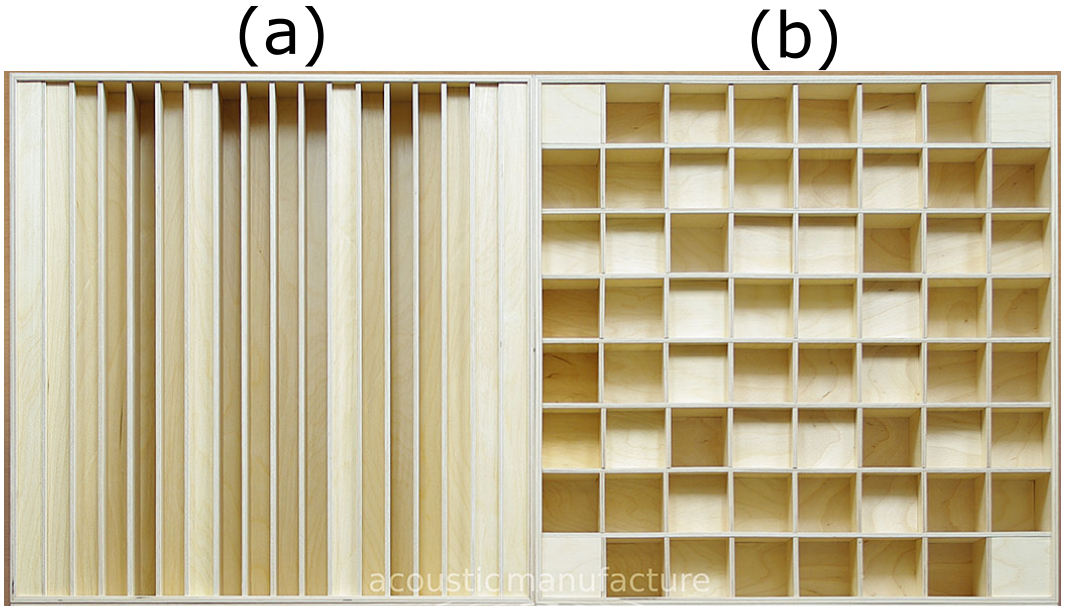

Figure 2.13: (a) 1D vs (b) 2D QRD geometries. Figure adapted from *Acoustic Manufacture* website (www.acousticmanufacture.com.pl/en/).

2.3.1 1D QRDs

The design frequency of the QRD, f_0, is the lowest frequency at which the QRD will diffuse. The wavelength at the design frequency, λ_0, is given by

$$\lambda_0 = \frac{c_0}{f_0} \tag{2.39}$$

where $c = 343$ m/s, the assumed speed of sound in air. The depth of the n^{th} well for a QRD is then found through the relation [4]

$$d_n = \frac{\lambda_0}{2N} s_n, \tag{2.40}$$

where

$$s_n = n^2 \text{mod} N. \tag{2.41}$$

Here,"mod" indicates the modulo operation, which gives the remainder when the first number is divided by the second; in other words,

$$\begin{aligned} s_1 &= \text{remainder}\left(\frac{1^2}{7} = 1\right), \\ s_2 &= \text{remainder}\left(\frac{2^2}{7} = 4\right) ... \end{aligned} \tag{2.42}$$

For an $N = 7$ 1D QRD, as shown in Fig. 2.12, the sequence for well depth is

$$s_n = [0 \quad 1 \quad 4 \quad 2 \quad 2 \quad 4 \quad 1]. \tag{2.43}$$

Block height can be calculated in a similar way. To determine the block heights, one would simply take the well depth sequence and subtract each number from the greatest number in the sequence, which for this case, is 4. This gives the following sequence for block height for a $N = 7$ QRD:

$$s_{n,\text{height}} = [4 \quad 3 \quad 0 \quad 2 \quad 2 \quad 0 \quad 3]. \tag{2.44}$$

Consider the example of a 1D QRD with a design frequency of 5000 Hz. For this case, Eqs. 2.39 and 2.40 become the following for the design wavelength and well depth:

$$\lambda_0 = \frac{c_0}{5000 \text{ Hz}} = 0.0686 \text{ m}$$

and

$$d_n = \frac{0.0686}{(2)(7)} s_n, \tag{2.45}$$

where s_n is given in Eq. 2.43. The depth in millimeters for this example case is thus

$$d_n = [0 \quad 5 \quad 20 \quad 10 \quad 10 \quad 20 \quad 5], \tag{2.46}$$

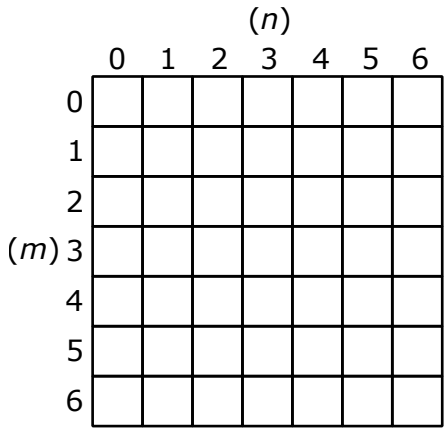

Figure 2.14: Example of a 7x7 grid used to determine the height of the blocks in a 2D QRD. Here, n and m are the indices of the sequence provided in Eq. 2.48.

and the block height, h_n, is

$$h_n = [20 \quad 15 \quad 0 \quad 10 \quad 10 \quad 0 \quad 15]. \tag{2.47}$$

2.3.2 2D QRDs

As mentioned in the previous section, a 1D QRD only diffuses sound in one plane. To diffuse sound in all directions that are not co-planar with the diffuser, a 2D QRD is needed. The design of well depths for 2D QRDs, provided by Eq. 2.48, is determined by a sequence that closely follows that of its 1D analogue [3]:

$$s_{nm} = (n^2 + m^2) \mathrm{mod} N, \tag{2.48}$$

where n and m index the sequence for the n^{th} and m^{th} wells, as shown in Fig. 2.14. Since $(0, 0)$ starts in the top left corner, the sequence for a $N =$

$M = 7$ QRD is

$$s_{nm} = \begin{bmatrix} 0 & 1 & 4 & 2 & 2 & 4 & 1 \\ 1 & 2 & 5 & 3 & 3 & 5 & 2 \\ 4 & 5 & 1 & 6 & 6 & 1 & 5 \\ 2 & 3 & 6 & 4 & 4 & 6 & 3 \\ 2 & 3 & 6 & 4 & 4 & 6 & 3 \\ 4 & 5 & 1 & 6 & 6 & 1 & 5 \\ 1 & 2 & 5 & 3 & 3 & 5 & 2 \end{bmatrix}. \tag{2.49}$$

In order to make the QRD symmetrical about the center, the sequence can be shifted 3 units to the right and 3 units down. The sequence for well depths and block heights now look like this:

$$s_{nm,\text{depth}} = \begin{bmatrix} 4 & 6 & 3 & 2 & 3 & 6 & 4 \\ 6 & 1 & 5 & 4 & 5 & 1 & 6 \\ 3 & 5 & 2 & 1 & 2 & 5 & 3 \\ 2 & 4 & 1 & 0 & 1 & 4 & 2 \\ 3 & 5 & 2 & 1 & 2 & 5 & 3 \\ 6 & 1 & 5 & 4 & 5 & 1 & 6 \\ 4 & 6 & 3 & 2 & 3 & 6 & 4 \end{bmatrix}, \tag{2.50}$$

$$s_{nm,\text{height}} = \begin{bmatrix} 2 & 0 & 3 & 4 & 3 & 0 & 2 \\ 0 & 5 & 1 & 2 & 1 & 5 & 0 \\ 3 & 1 & 4 & 5 & 4 & 1 & 3 \\ 4 & 2 & 5 & 6 & 5 & 2 & 4 \\ 3 & 1 & 4 & 5 & 4 & 1 & 3 \\ 0 & 5 & 1 & 2 & 1 & 5 & 0 \\ 2 & 0 & 3 & 4 & 3 & 0 & 2 \end{bmatrix}. \tag{2.51}$$

For a 2D QRD, with the same design frequency as considered for the 1D QRD example above, 5000 Hz, the well depths and block heights, in millimeters,

become

$$d_{nm} = \begin{bmatrix} 20 & 30 & 15 & 10 & 15 & 30 & 20 \\ 30 & 5 & 25 & 20 & 25 & 5 & 30 \\ 15 & 25 & 10 & 5 & 10 & 25 & 15 \\ 10 & 20 & 5 & 0 & 5 & 20 & 10 \\ 15 & 25 & 10 & 5 & 10 & 25 & 15 \\ 30 & 5 & 25 & 20 & 25 & 5 & 30 \\ 20 & 30 & 15 & 10 & 15 & 30 & 20 \end{bmatrix}, \tag{2.52}$$

$$h_{nm} = \begin{bmatrix} 10 & 0 & 15 & 20 & 15 & 0 & 10 \\ 0 & 25 & 5 & 10 & 5 & 25 & 0 \\ 15 & 5 & 20 & 25 & 20 & 5 & 15 \\ 20 & 10 & 25 & 30 & 25 & 10 & 20 \\ 15 & 5 & 20 & 25 & 20 & 5 & 15 \\ 0 & 25 & 5 & 10 & 5 & 25 & 0 \\ 10 & 0 & 15 & 20 & 15 & 0 & 10 \end{bmatrix}. \tag{2.53}$$

2.3.3 Inverse QRDs

Remember that QRDs are periodic devices; they behave optimally when multiple periods of QRDs are placed together on a surface [3]. As shown in Fig. 2.15, however, there are lobes where the energy is concentrated; this is caused by the periodicity of the QRD, which leads to spatial aliasing, also known as grating lobes. This is due to the constructive interference associated with Bragg scattering by the periodic arrangements of the QRD units. Cox and D'Antonio call this the "curse of periodicity." Specifically, they state that "a QRD needs periodicity to form its optimum diffusion of even energy lobes, yet the periodicity lobes cause uneven scattering" [3]. To mitigate this, it is useful to make the device aperiodic. One way to do this is by creating the inverse QRD, as shown in Fig. 2.16a. The inverse produces the same scattering

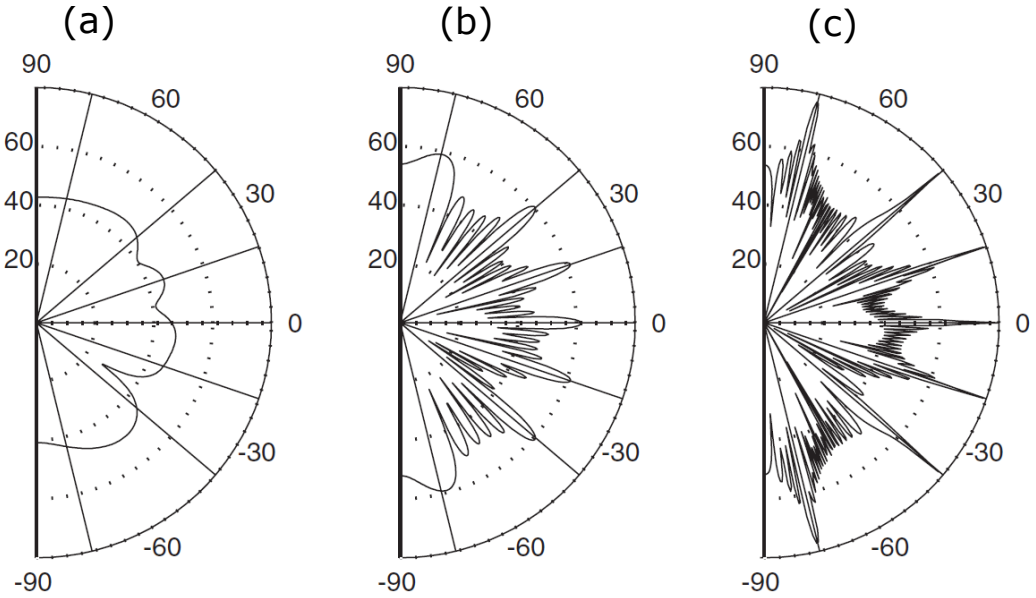

Figure 2.15: The effect of periodicity on the scattering from a N=7 QRD at 3000 Hz. (a) 1 period, (b) 6 periods, (c) 50 periods. Figure adapted from Cox and D'Antonio [3].

as the normal panel, but is 180° out of phase. Creating a QRD with a normal panel and an inverse panel in an aperiodic or pseudo-random arrangement helps to reduce the periodicity lobes that plague a QRD with just a periodic arrangement of normal panels.

The inverse sequence simply takes the normal sequence and subtracts it from N:

$$s_{n,inverse} = N - s_n. \tag{2.54}$$

Thus, the well depth and block height inverse sequences for a 1D $N = 7$ QRD look like this:

$$s_{n,\text{inverse,depth}} = [7 \quad 6 \quad 3 \quad 5 \quad 5 \quad 3 \quad 6], \tag{2.55}$$

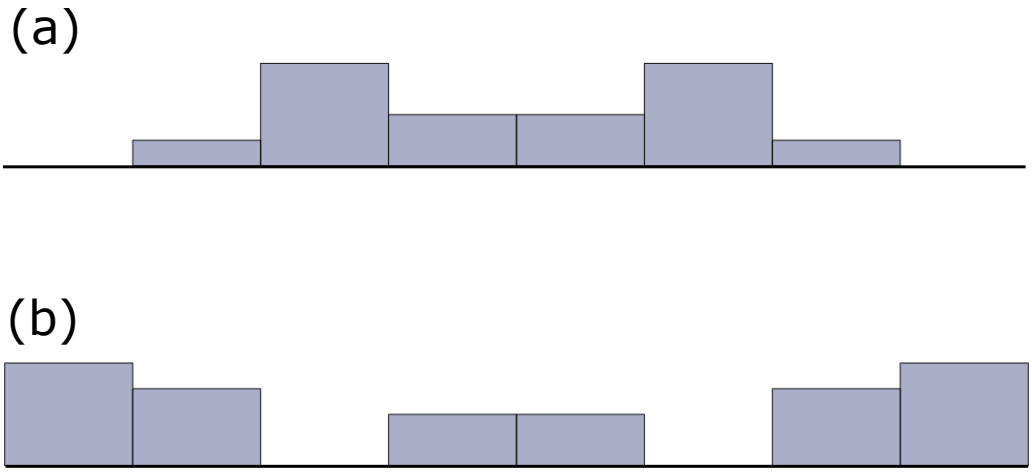

Figure 2.16: 1D (a) Inverse QRD versus (b) Normal QRD.

$$s_{n,\text{inverse,height}} = [0 \quad 1 \quad 4 \quad 2 \quad 2 \quad 4 \quad 1]. \tag{2.56}$$

The well depth inverse sequence for a 2D QRD looks like this:

$$s_{n,\text{inverse,depth}} = \begin{bmatrix} 3 & 1 & 4 & 5 & 4 & 1 & 3 \\ 1 & 6 & 2 & 3 & 2 & 6 & 1 \\ 4 & 2 & 5 & 6 & 5 & 2 & 4 \\ 5 & 3 & 6 & 0 & 6 & 3 & 5 \\ 4 & 2 & 5 & 6 & 5 & 2 & 4 \\ 1 & 6 & 2 & 3 & 2 & 6 & 1 \\ 3 & 1 & 4 & 5 & 4 & 1 & 3 \end{bmatrix}. \tag{2.57}$$

The well depths and block heights are calculated the same way as before, as given in Eq. 2.40. The 1D well depths and block heights in millimeters are

$$d_{n,\text{inverse}} = [35 \quad 30 \quad 15 \quad 25 \quad 25 \quad 15 \quad 30], \tag{2.58}$$

$$h_{n,\text{inverse}} = [0 \quad 5 \quad 20 \quad 10 \quad 10 \quad 20 \quad 5]; \tag{2.59}$$

and the 2D well depths are

$$d_{n,\text{inverse}} = \begin{bmatrix} 15 & 5 & 20 & 25 & 20 & 5 & 15 \\ 5 & 30 & 10 & 15 & 10 & 30 & 5 \\ 20 & 10 & 25 & 30 & 25 & 10 & 20 \\ 25 & 15 & 30 & 0 & 30 & 15 & 25 \\ 20 & 10 & 25 & 30 & 25 & 10 & 20 \\ 5 & 30 & 10 & 15 & 10 & 30 & 5 \\ 15 & 5 & 20 & 25 & 20 & 5 & 15 \end{bmatrix}, \tag{2.60}$$

which makes the block heights

$$h_{n,\text{inverse}} = \begin{bmatrix} 15 & 25 & 10 & 5 & 10 & 25 & 15 \\ 25 & 0 & 20 & 15 & 20 & 0 & 25 \\ 10 & 20 & 5 & 0 & 5 & 20 & 10 \\ 5 & 15 & 0 & 30 & 0 & 15 & 5 \\ 10 & 20 & 5 & 0 & 5 & 20 & 10 \\ 25 & 0 & 20 & 15 & 20 & 0 & 25 \\ 15 & 25 & 10 & 5 & 10 & 25 & 15 \end{bmatrix}. \tag{2.61}$$

2.4 Summary

This chapter has discussed the most common types of acoustic absorbers and diffusers in detail. Porous absorbers, which use friction to generate loss, can be used on their own in porous panels, or used to add damping in resonant absorbers. Helmholtz resonators are a large class of absorbers that involve a mass vibrating against a spring. In addition to the typical structure of a Helmholz resonator, which is shown in Fig. 2.4, porous and perforated panels are also considered to be part of the Helmholtz absorber category, as they also use the mass-spring resonance to produce absorption. In the case of the panel resonators, the mass is the panel, and spring is the volume behind the panel.

Quarter-wave resonators are interesting absorbers. When the depth of the tube is exactly a quarter of the wavelength or multiples of a quarter wavelength of the incident sound, the reflected wave is exactly 180° out of phase with the incident, which produces perfect absorption.

Schroeder's Quadratic Residue Diffuser are the most common type of diffuser. They consist of a periodic series of blocks, with their heights determined by the quadratic residue sequence and the wavelength of the design frequency. 1D diffusers diffuses only in one plane, whereas 2D diffusers diffuse in all directions that are not co-planar with the diffuser. However, the QRD has some downsides. Because their size is determined by the wavelength of the design frequency, they must be fairly large in order to diffuse at low frequencies. Its periodic nature causes grating lobes, and requires it to take up a large amount of wall space to be effective. In addition, the different block heights may not be aesthetically pleasing to some, and may not fit in well with the decor of some rooms.

One way to address these issues is to use acoustic metamaterials. The next chapter will discuss some current metamaterial absorber and diffuser designs, before delving into two specific metamaterial diffuser designs that will attempt to replicate the response of the QRD. Their responses will be compared to that of the QRD to determine whether they are viable replacement options.

Chapter 3

Coiled Space Metamaterials

Acoustic metamaterials (AMM) are a relatively new field of research in applied physics that have the potential to realize physical phenomenon that do not exist in naturally occurring media as a means to address existing engineering challenges [6] [7]. AMMs have the ability to realize exotic behavior because their characteristics are derived from their engineered structure instead of the properties of the materials of which they are comprised. AMM have now been created that display extreme parameters such as negative effective mass density and negative bulk modulus [8] [9], known as double negative materials. AMMs have even been created that can be used as invisibility cloaks [10] [11] and flat lenses that are capable of focusing or steering an acoustic beam [12] [13].

Coiled space metamaterials fall into a class of structured media called acoustic metasurfaces (AMS), which are acoustically thin (small with respect to a wavelength) interfaces that generate "arbitrary" control of reflected and transmitted phase and permit improved control of reflected and transmitted fields. Coiled space metamaterials have been used to modulate both phase and amplitude of acoustic fields that are reflected from or transmitted through an

interface between two media [14]. Recent examples of AMS relevant to the present study include Li et al. designed a gradient index (GRIN) lens using coiled space metamaterials [12]. Xie et al. demonstrated a broadband negative refractive index from a coiled space metamaterial [15]. While these previously demonstrated behaviors are interesting from a purely scientific standpoint, one of the more practical applications of coiled space AMS is in the design of acoustically thin absorbing and diffusing surfaces.

In this chapter, some current designs of AMS absorbers and diffusers are reviewed, before taking an in-depth look at two specific coiled space metamaterial designs that will be used to mimic the response of a Schroeder QRD.

3.1 Acoustic Metamaterial Surface Treatments

3.1.1 Metamaterial Absorbers

Metatmaterial absorbers have recently become a topic of interest to address practical problems in acoustics, such as the absorption of air-borne acoustic energy. As seen in the previous chapter, current absorber designs are often impractical as they can be quite bulky and their performance is often limited to narrowband operations, especially at low frequencies. Recent research has shown that coiled space metamaterial absorbers can be designed to function as low frequency sound absorbers that are thinner (compared to a wavelength) by employing unique coiled space designs. These absorbers take the length of a quarter-wave resonator and coil it to create a much smaller absorber. An example of this is shown in Fig. 3.1, where the red line shows

the pathlength that waves would propagate along, called the effective length. For this example, the coiled space metamaterial is 1/7th the size of a quarter-wave resonator with the same depth.

In this section, three coiled space metamaterial absorber designs are explored to provide some perspective on this approach. The first was by Yang, et al., who create a thin broadband perfect absorber by combining several folded quarter-wave resonators into a single unit cell [16]. The next structure was proposed by Li et al., who describe an even thinner, but narrowband, perfect absorber by coiling the space behind a perforated plate [17]. The final design was proposed by Zhang et al., who create a similar structure to Li's, but coil the space differently [18].

The work of Yang et al. is of specific interest because it applies the principle of causality to design an absorbing structure that will produce near perfect absorption over a wide range of frequencies. Using the bounds determined using the causality relation, they consider the tradeoffs between three parameters: sample thickness, frequency bandwidth, and absorption coefficient [16]. By specifying two of the parameters, they are able to optimize the third in order to achieve optimal absorption over a wide range of frequencies. The structure they created, which is shown in Fig. 3.2, was experimentally proven to produce almost perfect absorption at frequencies from 400 Hz to 3000 Hz. The structure consists of 16 channels, with the colors representing the number of foldings in that channel: blue channels have three foldings, pink channels have two foldings, orange channels have one folding, and green channels are

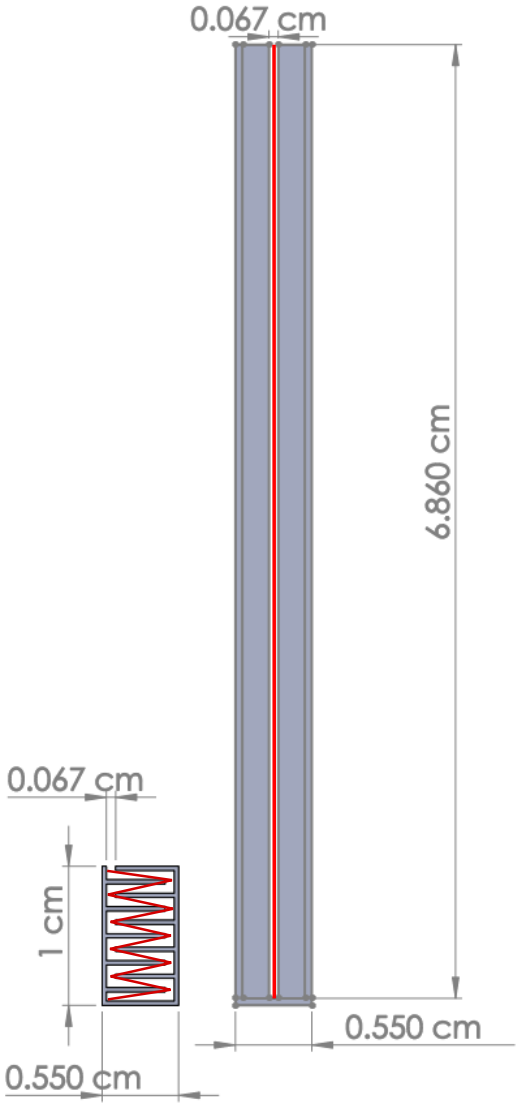

Figure 3.1: Comparison of a coiled space metamaterial to a quarter-wave resonator with the same uncoiled effective length.

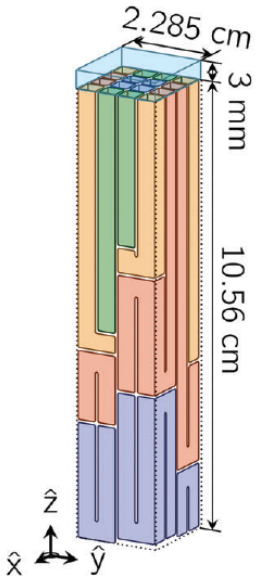

Figure 3.2: Yang's coiled space structure. The transparent blue block on top represents a sponge placed on top of the structure. Figure adapted from Yang et al. [16].

straight. The sponge on top of the structure reduces the oscillations at the mouth of the channels. They compare the absorption of this structure with that of a micro-perforated plate, and determine that this structure absorbs significantly better than the plate for a wider range of frequencies [16].

Yong Li and colleagues also desired to create a thin perfect absorber, but they used a perforated plate covering a structure coiling in the x-y plane, as shown in Fig. 3.3, instead of the y-z plane, as demonstrated by Yang et al. Modeled after a conventional perforated plate system discussed in Section 2.2.1.2, Li's structure takes the distance behind the perforated plate and coils it horizontally. The result is an extremely thin structure that produces perfect absorption while only measuring approximately $\lambda/223 = 12.2$ mm thick.

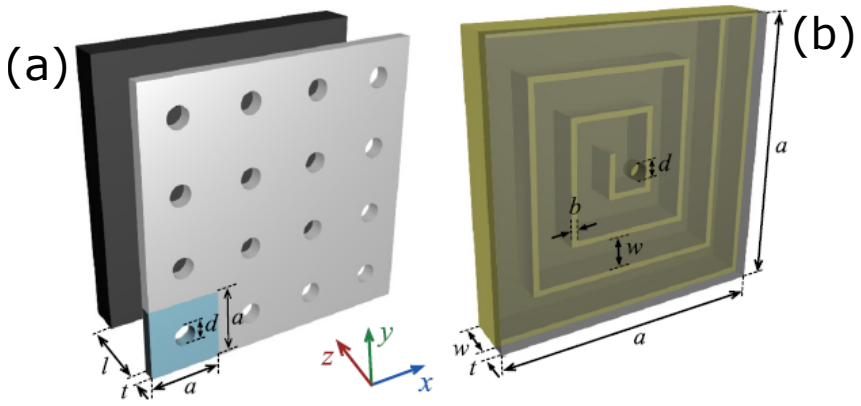

Figure 3.3: Li's coiled space structure consists of a perforated plate with a hole in the center, which leads into a coiled space air cavity underneath. (a) shows a conventional perforated plate in front of a hard surface. (b) shows Li's coiled space design, which coils space horizontally underneath a perforated plate to create a sub-wavelength structure capable of perfect absorption. Figure adapted from Li et al. [17].

While the effective length of the chamber cannot be calculated analytically, it can be derived from the reflection coefficient in the simulations by considering the structure as a quarter-wave resonator and finding the quarter-wave resonance. The drawback of this particular design is that while it produces perfect absorption, the absorbing performance is limited to a frequency band around resonance, much like quarter-wave and Helmholtz resonators [17].

A similar design was proposed by Zhang et al. [18], who designed a coiled space absorber similar to the work of Li and colleagues; both coiling in the x-y plane, the plane of the surface where the AMS is mounted, allowing for a very thin absorber, as shown in Fig. 3.4). However, instead of coiling the chamber circularly, they fold horizontally. Due to the straight paths within

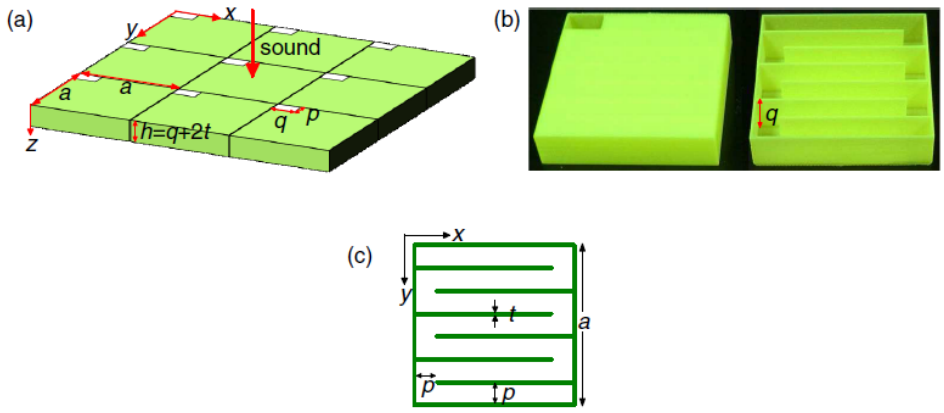

Figure 3.4: Zhang's coiled space metamaterial absorber, where (a) shows an array of unit cells with an incident plane wave normal to the surface, (b) shows a 3D fabricated unit cell: the left side is the complete unit cell, whereas the right side is the unit cell with the top cover removed to show the coiled space chamber underneath. The dimensions of the interior channels is given in (c). Figure adapted from Zhang et al. [18].

Zhang's structure, the effective length can be computed in a straightforward manner, and thus the frequency of peak absorption can be estimated from simple analytical functions of the geometry. With a single unit cell, these structures achieve near perfect absorption, and can be tuned to absorb at any frequency by varying the height, width, and effective length of the coiled space. However, Zhang takes it a step further and demonstrates almost perfect absorption over a broadband range of frequencies by combining multiple units together, as shown in Fig. 3.5 [18].

All of the designs presented above achieve near perfection absorption using coiled space structures. Yang's and Zhang's structures approach perfect absorption over a wide range of frequencies, whereas Li's structure is focused

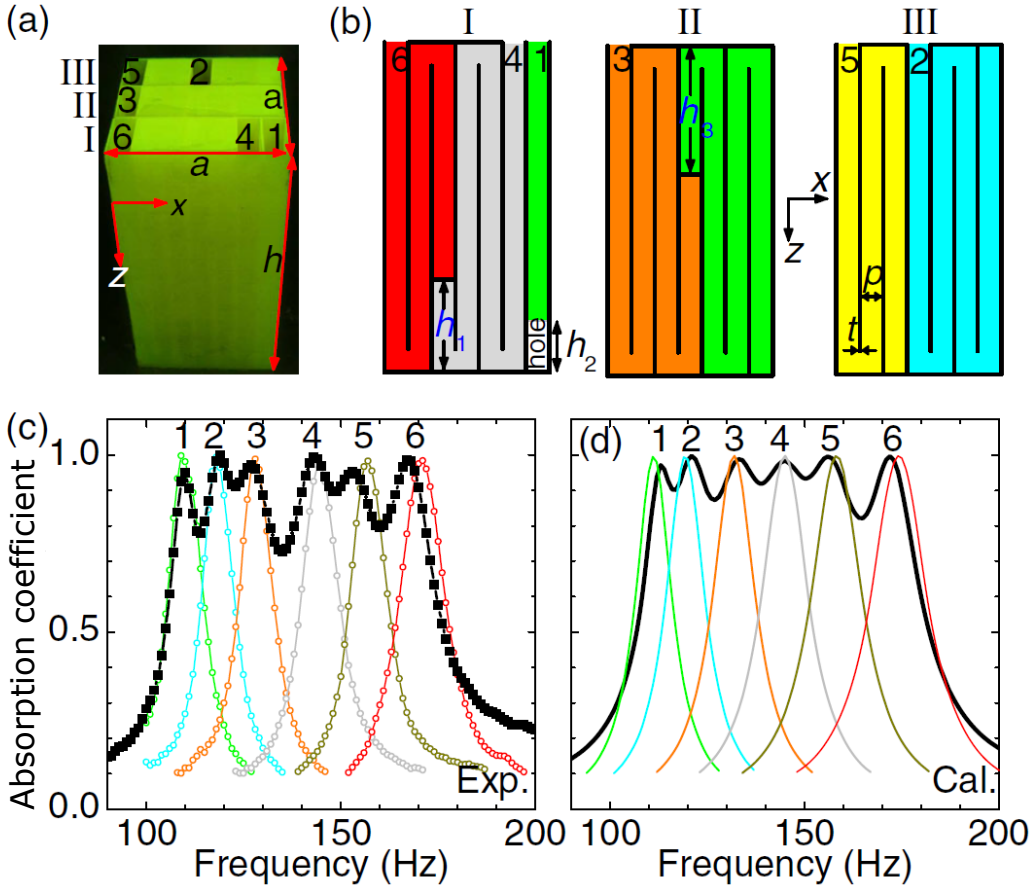

Figure 3.5: Zhang demonstrates how to make a broadband absorber by stacking multiple unit cells, where (a) shows the stacked unit cell made up of the coils in (b), (c) shows the measured absorption of the unit cell (black) as well as each individual colored coil section from (b), and (d) gives the calculated absorption of the unit cell (black) and the individual channels (colored). Figure adapted from Zhang et al. [18].

on a narrowband of frequencies, and is therefore analogous to quarter-wave resonator absorbers. Since Yang strictly desires to create a sub-wavelength broadband perfect absorber, his proposed design would make a poor diffuser. Both Zhang and Li's designs, however, show narrowband absorption, and could possibly be used as the elemental units of acoustic diffusers. However, neither Zhang nor Li address the potential of using their proposed structures to create acoustic diffusers. Their proposed designs could be used to induce a phase change that could match that of the individual wells in a QRD, but the absorption of each unit cell could adversely affect its ability to be used as a diffuser. Current metamaterial diffuser designs are reviewed in the next section.

3.1.2 Metamaterial Diffusers

In contrast to absorbers, diffusers attempt to incoherently scatter incident sound wave energy without absorbing it, thereby maintaining the energy in the room but reducing coherence in reflected waves. This creates a perception of warmth and envelopement in the room [3]. The most common diffuser, the Quadratic Residue Diffuser, was introduced in the previous chapter. The following metamaterial diffuser designs attempt to mimic the response of the QRD, while solving one of its biggest issues: size. While the metamaterial designs introduced in the literature do not specifically use coiled space, they do explore the idea of folding space to make the diffusers thinner and smaller. This section will look at two designs proposed in open literature: the first by Zhu and collegues, who uses resonant T-shaped structures to achieve sound

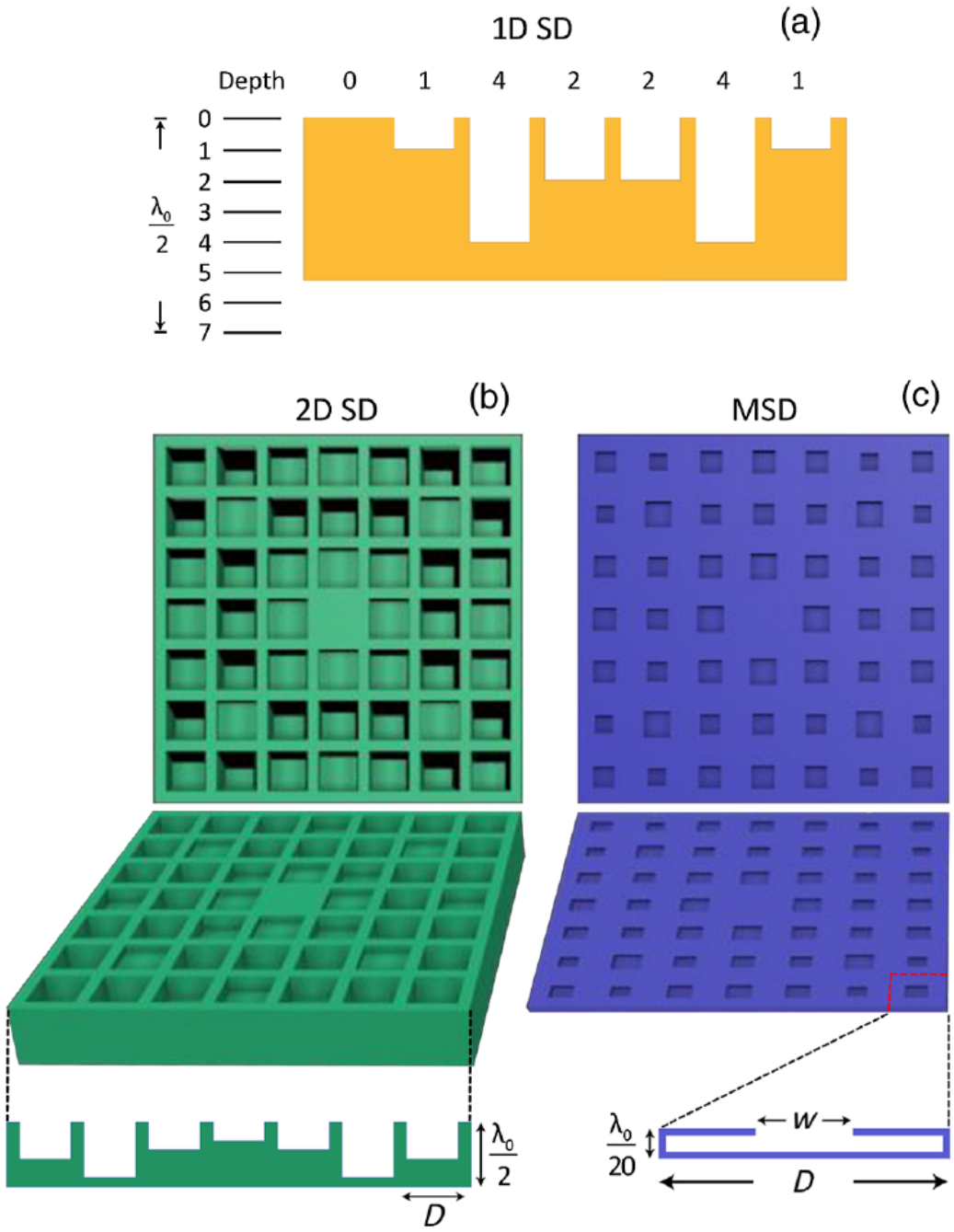

Figure 3.6: Zhu's metamaterial diffuser compared to a Schroeder diffuser, where (a) shows a cross section of a 1D Schroeder, and (b) compares a 2D Schroeder diffuser to (c) Zhu's diffuser. Figure adapted from Zhu et al. [19].

diffusion [19], and the next by Jiménez et al., who uses Helmholz resonators [20].

Zhu's diffuser is based on a T-shaped cavity, as shown in Fig. 3.6. While this design looks like a Helmholz resonator, Zhu reasons that its cavity width and neck are larger than those of traditional Helmholz resonators, and thus the lumped element model does not apply [19]. Zhu does not specify how the phase shift of each well is calculated, but merely states that the phase of each unit cell matches that of the well depth at the same location in the QRD. This design is thus able to produce almost a full 2π radian phase shift between the incident and reflected signals by only varying one parameter, the width w, while having an in-plane thickness of approximately $\lambda/20$ of the design frequency. This depth compares very favorably to $\lambda/2$ of the design frequency like the QRD. Zhu then compares the response of the metasurface-based Schroeder diffuser (MSD) with that of the QRD for both normal and oblique incidence, proving that the MSD matches the response of the QRD fairly closely for both the specific cases that are presented. In the supplemental material, Zhu explores the thermo-viscous losses of the MSD structure, and concludes that the losses are small and do not affect the scattered field [19]. However, all these simulations were only done for one frequency, and do not capture the response of the MSD over a range of frequencies. Whether or not the MSD performs the same as a traditional QRD over a wide range of frequencies is therefore an open research question. In addition, while the absorption may be negligible at the design frequency, the absorption may be

much greater at other frequencies, specifically when approaching the resonance frequency of the T-shaped well. These points are not addressed by Zhu et al [19].

Jiménez also determines the phase of each well in the QRD and matches this to the design, but in contrast to Zhu, Jiménez uses true Helmholz resonators inset into a slotted panel, as shown in Fig. 3.7. The phase of the reflected wave can be modified by tuning the geometry of the Helmholtz resonator and the thickness of the slits. Jiménez's design demonstrates the ability to match the response of diffusers based on multiple sequences: primitive root sequence, the quadratic residue sequence, and a ternary sequence at a single frequency. Unlike Zhu, however, Jiménez is able to demonstrate diffusion over a broad range of frequencies with this design by extending the bandwidth of the optimization procedure. Jiménez does provide absorption data, and it shows that while the broadband absorption is fairly low (0.2), it is still significantly higher than that of a regular QRD.

These two metadiffuser designs provide proof that it is indeed possible to create a sub-wavelength diffuser using metamaterials. However, neither of them use coiled space, merely citing that coiled-space-based diffusers have much greater thermo-viscous losses. The following sections will detail two designs in particular that seem promising in exploring the use of coiled space metamaterials as diffusers. In particular, the following sections will attempt to shed light on the losses inherent in the coiled space designs that other articles have mentioned.

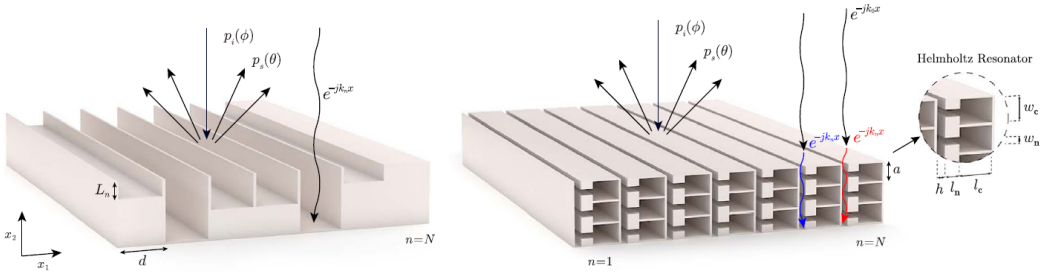

Figure 3.7: On the left is a standard N=7 QRD; on the right is Jiménez's design consisting of slits backed by Helmholz resonators. Figure adapted from Jiménez et al. [20].

3.2 Memoli Bricks

In 2017, Memoli et al. released a paper focusing on the use of metamaterials to achieve acoustic focusing, steering, and even acoustic levitation. Their unit cells, referred to as "bricks," are encoded with a specific phase delay by altering the internal structure, like the previously discussed metamaterial diffusers. They accomplished this by varying specific parameters of the brick geometry, allowing them to change the effective length that the wave travels through the brick, and thus specifying the phase change of the wave being transmitted through the brick. A 3D rendering of these bricks and the encoded phase shift of each individual brick is shown in Fig. 3.8. A representative cross section of the bricks is shown in Fig. 3.9.

Memoli created sixteen bricks, each with different phase shifts, so that together they spanned the phase range from 0 to 2π radians. Because these bricks have a less tortuous internal geometry than previous coiled space metamaterial unit cells, they were able to achieve transmission coefficient mag-

nitudes close to unity, indicating almost no losses. Since previous literature had pointed to the problem of viscous losses due to the tortuous path of existing coiled space metamaterial unit cells, the Memoli brick geometry offers some promise in avoiding thermoviscous losses within the unit cell while still generating the required phase shifts within a spatially compact element.

The phase change accumulated across these elements is varied using only two parameters: b_{l}, the bar length; and b_{s}, the bar spacing, where the geometry is defined in Fig. 3.9. The parameter, p_{r}, the fillet radius, was made to be equal to the bar length when bar length was less than 0.1; above that, p_{r} was set at 0.1. The other parameters shown in Fig. 3.9 are dependent on the design frequency wavelength, λ. The original design was intended to be used to induce a phase change in the transmitted wave. The objective of the present work, the design of a metamaterial diffuser based on QRD sequencing, requires a phase shift in the reflected wave. The pathlength inside the brick is twice as long for a reflected wave than for a transmitted wave. Therefore, the design parameter, λ_0, was made to be half the design wavelength, λ. Since no analytical models were derived to estimate the phase shift associated with a given brick geometry, the finite element software, COMSOL, was used to calculate the transmitted phase of 1200 possible combinations of b_{l} and b_{s}. These phases were then compared to the selected target phases to determine the combination of parameters that would achieve phases as close to the target phase as possible [21]. The research outlined in this paper follows these same steps to determine the appropriate brick parameters that will match the

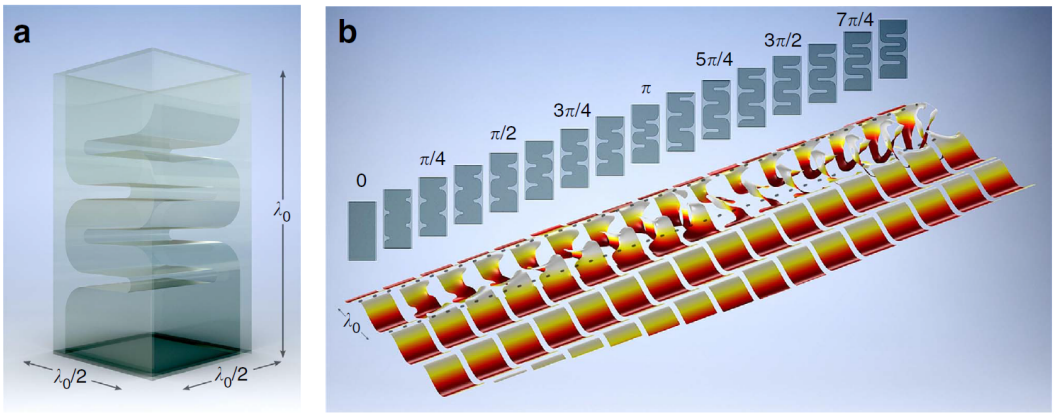

Figure 3.8: (a) 3D Rendering of a brick. (b) Cross-sections of 16 selected bricks and the corresponding phase maps at normal incidence. Figure adapted from Memoli et al. [21].

response of the QRD.

3.2.1 3D Finite Element Analysis of a 1D QRD

Having already determined the depths of each well in an $N = 7$ QRD using the standard approach, the six steps detailed below were used to design a metamaterial QRD that would mimic a Schroeder QRD.

1. Determine the amount of added distance a wave has to travel to reflect off of each block of a standard QRD diffuser as compared to the tallest block in that sequence.

2. Calculate the change in phase of the reflected wave for each block in the traditional QRD design.

3. Run a parametric sweep in a COMSOL simulation using 40 values of

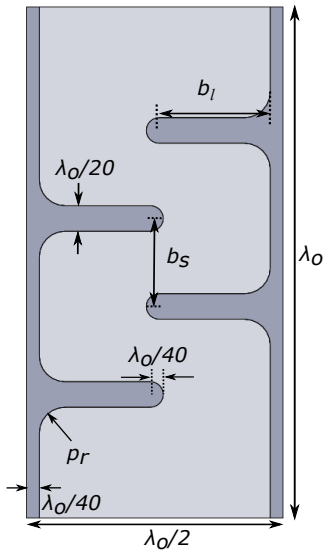

Figure 3.9: Parameters of Memoli's bricks. Figure adapted from Memoli et al. [21].

b_l and 30 values of b_s for predefined ranges, leading to 1200 possible combinations of those parameters.

4. Search for the combinations of b_l and b_s that correspond to the phase shift associated with each well of the standard QRD design.

5. Build each unit cell identified in the previous step and test them in an impedance tube to verify that they perform as expected based on the 3D finite element analysis.

6. Build a QRD using the selected unit cells that will mirror the response of the regular QRD and compare performance in both simulations and in the appropriate experimental space.

H (mm)	D (mm)	ϕ (deg)
20	0	0
15	5	−8.9
0	20	−49.9
10	10	−24.2

Table 3.1: Parameters and phase shift for each well of a standard a 1D N=7 QRD. H is the height of the QRD section, D is the additional distance a wave has to travel to reflect off of each block as compared to the tallest block, and ϕ is the associated phase difference between the incident and reflected fields for each well.

For a N=7 QRD with a design frequency of 5000 Hz, the 1D block height sequence is given by Eq. 2.44, and the block heights are given in Eq. 2.47. The 2D sequence and heights are given in Eq. 2.50 and Eq. 2.53. A 3D finite element model in COMSOL was used to simulate the changes in depth as compared to the tallest block, as shown in Fig. 3.10, and Table 3.1 gives the phase shift for each block in a 1D QRD. Notice that in Fig. 3.10a, the cross-sectional areas of (1) and (2) are different than section (3). Since a QRD is always placed on a wall, which acts like a rigid baffle, this provides a more accurate representation of how an added depth will react to an incident wave.

With the target phases calculated, the next step was to run a parametric sweep in a COMSOL simulation, shown in Fig. 3.10, using 40 values of b_{l} and 30 values of b_{s}, leading to 1200 possible combinations of those parameters. The range of possible values for each parameter were determined based on the work of Memoli et al. [21]. To make the calculation simple, the bar length and bar spacing were defined as some ratio multiplied by λ_0 to make it easier

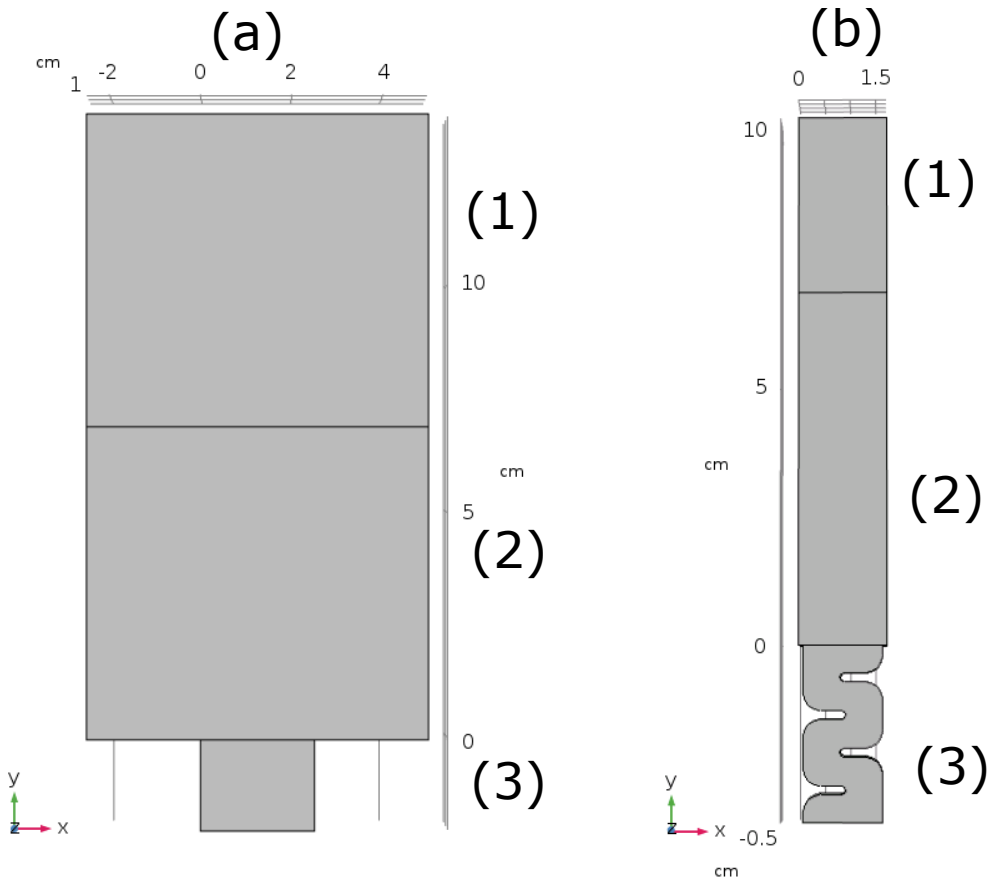

Figure 3.10: (a) Depth sweep simulation in the finite element software COMSOL for 20 mm depth. The extruded depth was made equal to the width, 25 mm. (b) Metamaterial brick simulation in COMSOL. The extruded depth was made equal to the width, 17 mm. The three sections for both (a) and (b): (1) perfectly matched layer, (2) background pressure field, (3) simulated depth (a) or brick (b). The boundaries in all regions are rigid.

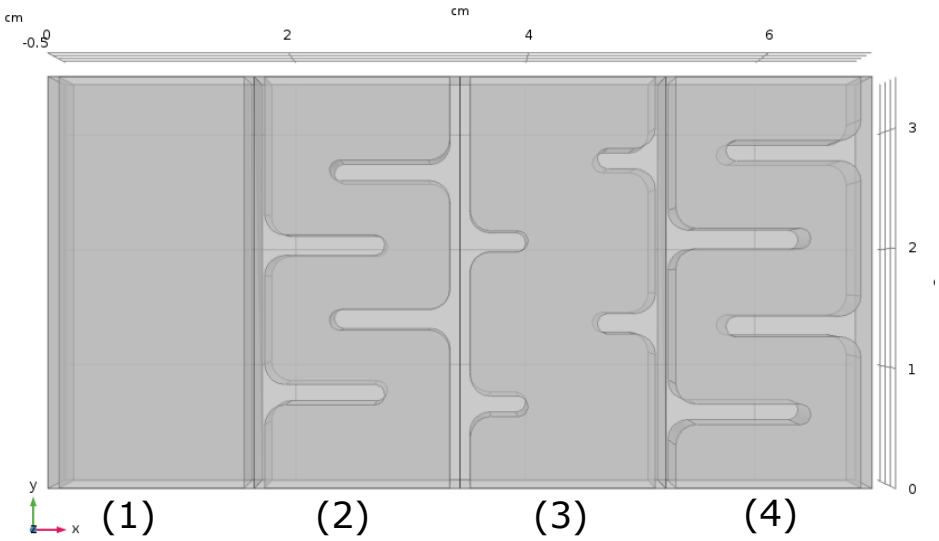

Figure 3.11: Bricks 1-4, replicating a 1D QRD.

to scale to other frequencies. Table 3.2 will thus be presented in terms of the ratios, b_l/λ_0 and b_s/λ_0. Figure 3.11 shows the 4 chosen bricks for the 1D QRD case. Notice that brick 1 is a straight tube. This is because brick 1 is designed to mimic the response of the tallest brick, which is considered the "0" phase configuration. The other bricks increase the pathlength the wave must travel through as compared to this first brick, which in turn leads to a phase change.

With brick parameters thus computed, a QRD created from metamaterial bricks of the type introduced by Memoli et al. [21] can be simulated, constructed and compared to the standard Schroeder QRD, as shown in Fig. 3.12. Notice that the metamaterial brick QRD (Fig. 3.12b) is actually taller than the standard QRD (Fig. 3.12a). This is due to the dimensions of the metamaterial bricks proposed by Memoli et al. [21]. Memoli's design requires that

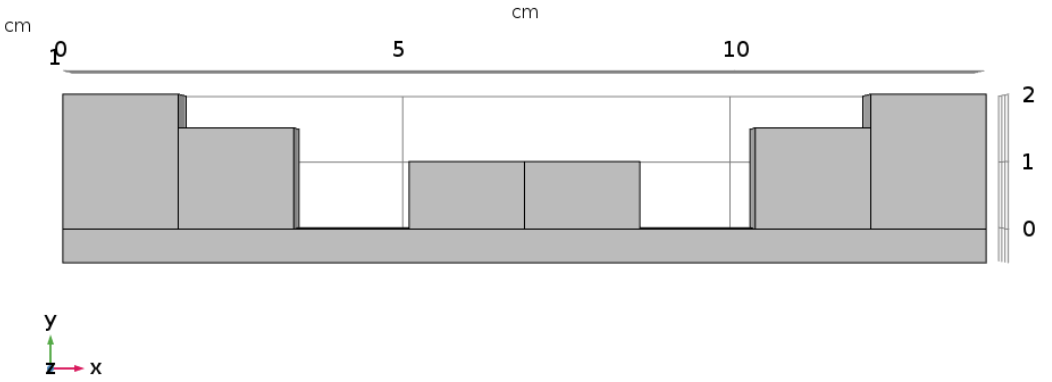

(a)

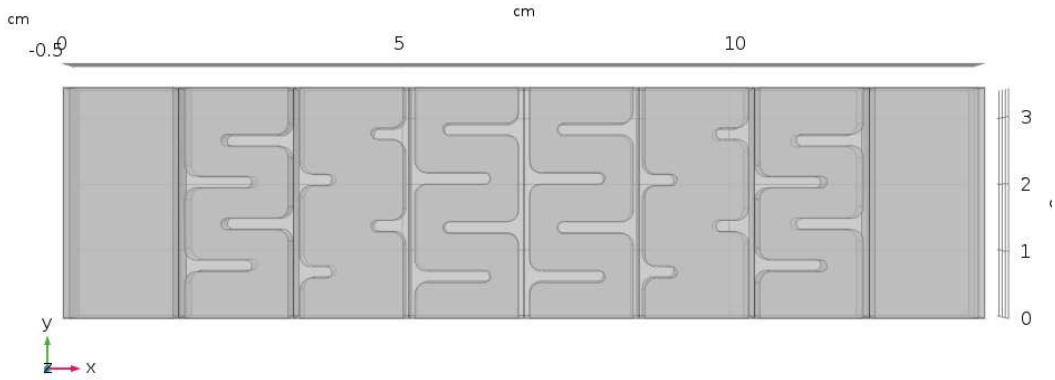

(b)

Figure 3.12: Nominally equivalent diffuser designs using (a) 1D QRD and (b) 1D Memoli brick QRD.

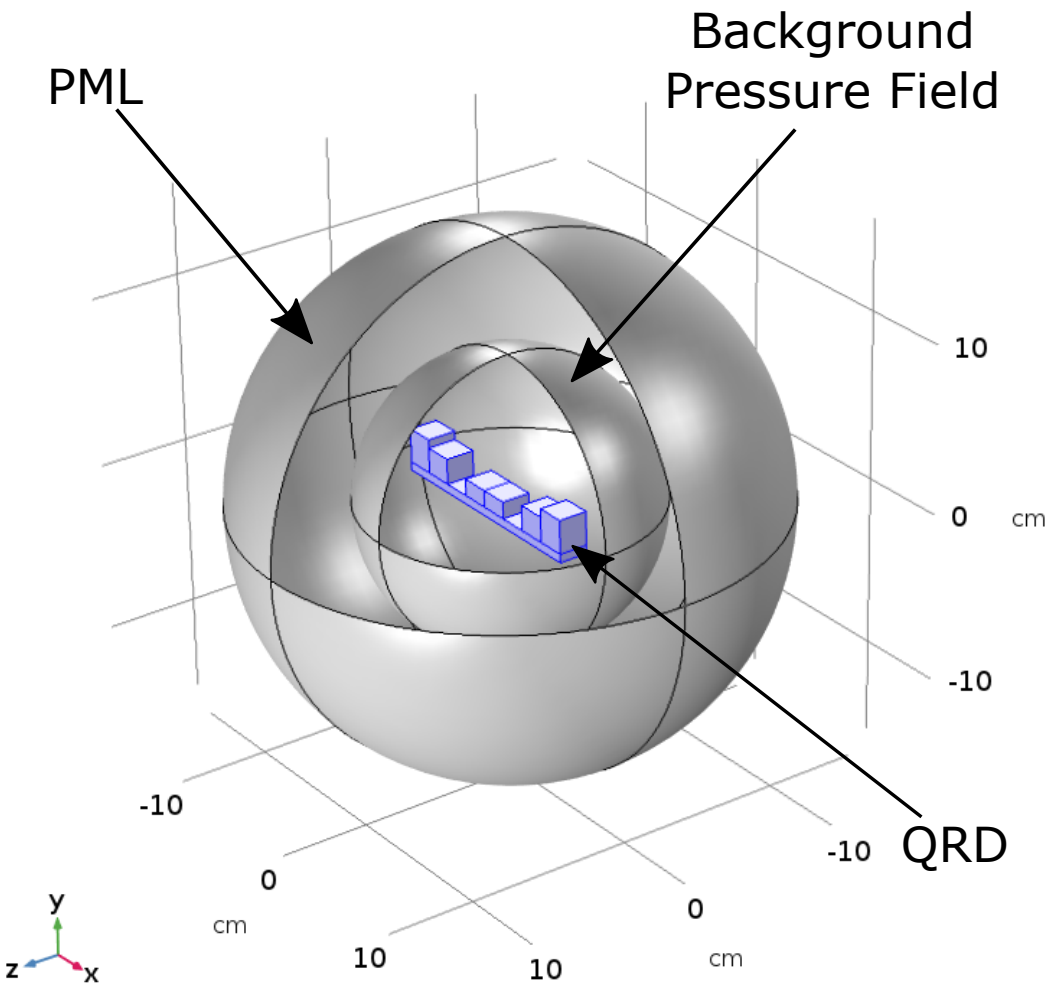

Figure 3.13: 3D QRD finite element simulation in COMSOL with three sections: perfectly matched layer (PML), background pressure field, QRD scatterer. The QRD is modeled with rigid boundaries and is suspended in free space for this model.

D (mm)	b_l/λ_0	b_s/λ_0	ϕ (deg)	ϕ_FEA (deg)
5	0.267	0.182	-8.9	-8.9
20	0.116	0.201	-49.9	-50.0
10	0.303	0.214	-24.2	-24.0

Table 3.2: Brick parameters for a 1D QRD. D is the additional distance a wave has to travel to reflect off of each block as compared to the tallest block, ϕ is the associated phase difference between the incident and reflected fields for each well, and ϕ_FEA is the associated phase difference between the incident and reflected fields for each brick extracted from the finite element simulation.

the bricks be a certain height in order to induce the necessary phase changes to mimic the standard QRD. While this may not be ideal in terms of reducing the required volume on a surface, a metasurface QRD designed in this way still has the desirable trait of having the same thickness at all points on a surface.

Figure 3.13 shows the model used to compute the far field responses for both the standard QRD and the metamaterial brick QRD. For these models, the sound speed was presumed to be 343 m/s, and the density of air was presumed to be 1.21 kg/m^3. Both the QRD and the metamaterial QRD were modeled with rigid boundaries, and thermoviscous effects were ignored.

Remember that the normal block width of a 5000 Hz QRD is 25 mm; however, the dimensions proposed by Memoli require that the width of the brick be 17 mm. In addition to comparing the response of a standard QRD with a 25 mm width with that of a metamaterial brick QRD, the following figures also compare the response of a QRD that has the same block width as the brick QRD (17 mm) to determine whether the period width has an effect on the diffusion pattern.

Figure 3.14 shows the far field scattered sound pressure level (SPL) polar response of a standard N=7 1D QRD design with a well width of 25 mm compared to that of a metamaterial brick QRD with a brick width of 17 mm. SPL is defined as

$$\mathrm{SPL}(\theta) = 20\log_{10}\left[\frac{|P(\theta)|}{P_{\mathrm{ref}}}\right], \tag{3.1}$$

where $P_{\mathrm{ref}} = 20\mu\mathrm{Pa}$ is the reference pressure in air. To more clearly see the difference in pattern, Fig. 3.15 shows the scattered field directivity function, $D(\theta)$, in dB, where [1]

$$D(\theta) = 20\log_{10}\left[\frac{|P(\theta)|}{|P_{\mathrm{max}})|}\right]. \tag{3.2}$$

where $P_{\mathrm{max}} = P(\theta_{\mathrm{max}})$ and θ_{max} is the angle at which the pressure is at its maximum. Figure 3.16 also shows the scattered far field SPL, but compares the response of the metamaterial brick QRD with a QRD of the same block width, 17 mm, instead. Likewise, Fig. 3.17 compares the scattered field directivity function, $D(\theta)$, of a 17 mm well width standard QRD with that of the metamaterial brick QRD.

While the response of the brick QRD is different than the regular QRD in Fig. 3.14, it is arguably better. Specifically, notice that the standard QRD has more defined (sharper and deeper) nulls in its response as compared to the metamaterial brick QRD. The metamaterial brick QRD diffuses more evenly in all directions and does not suffer from the peaks and nulls in the standard QRD's response. The only exception to this is the response of the metamaterial

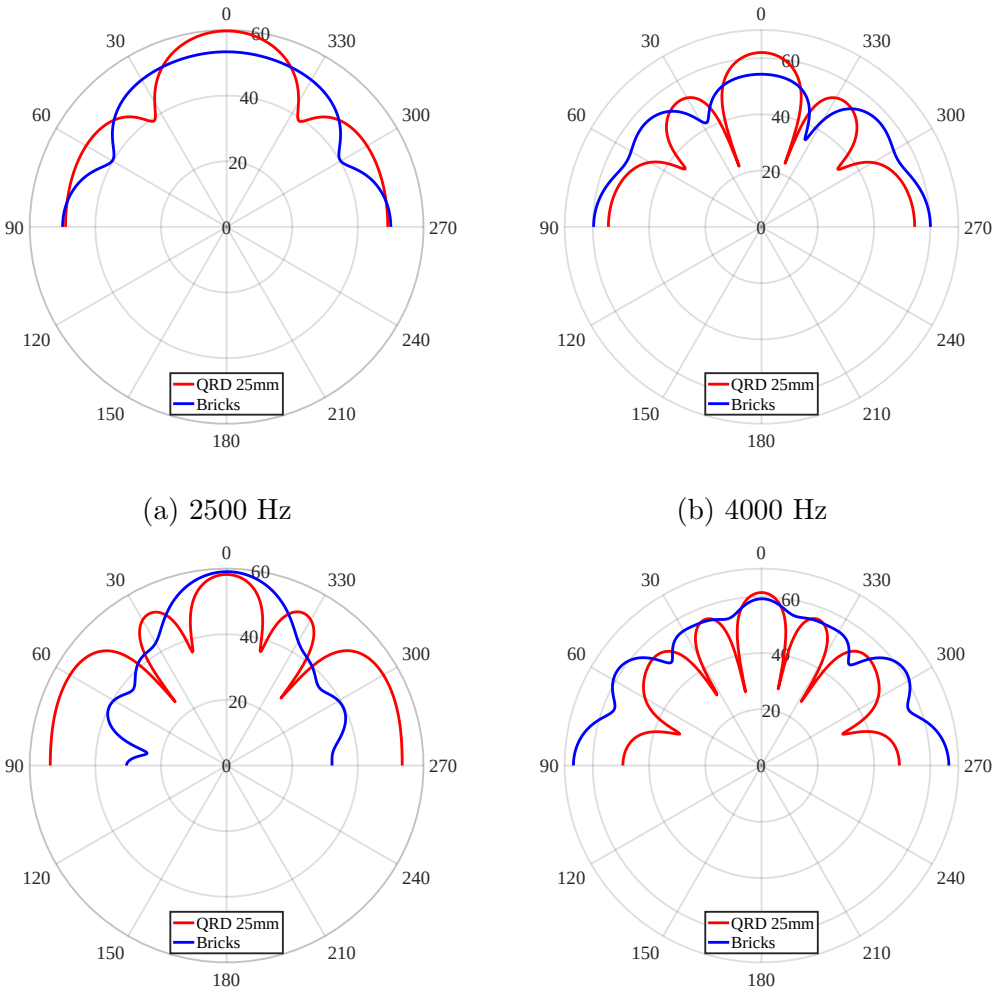

(a) 2500 Hz

(b) 4000 Hz

(c) 5000 Hz

(d) 6000 Hz

Figure 3.14: Far field scattered sound pressure level response of a standard N=7 QRD (25 mm width) and metamaterial brick QRD based on the design described in Table 3.2 at a design frequency of 5000 Hz. The radial grid is in units of dB re 20 μPa.

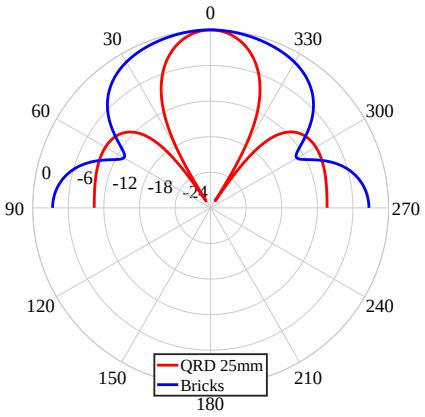

(a) 2500 Hz

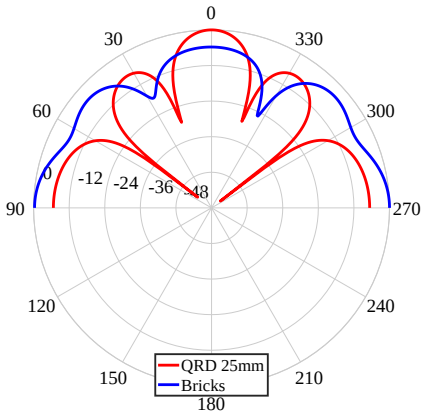

(b) 4000 Hz

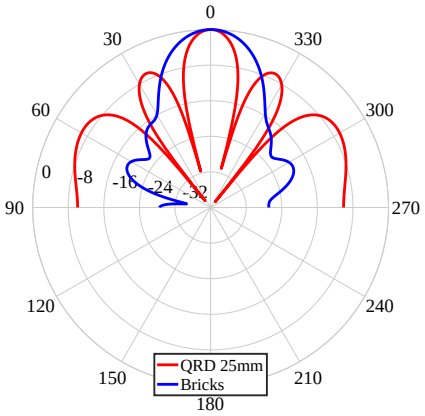

(c) 5000 Hz

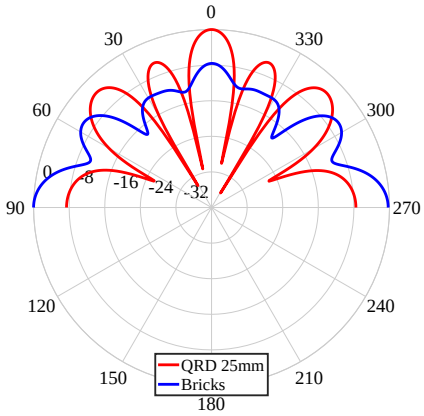

(d) 6000 Hz

Figure 3.15: Scattered field directivity plots (far field SPL of $P(\theta)$ normalized by $P_{\max}$ given by Eq. 3.2) of a standard N=7 QRD (25 mm width) and metamaterial brick QRD based on the design described in Table 3.2 at a design frequency of 5000 Hz. The radial grid is in units of dB.

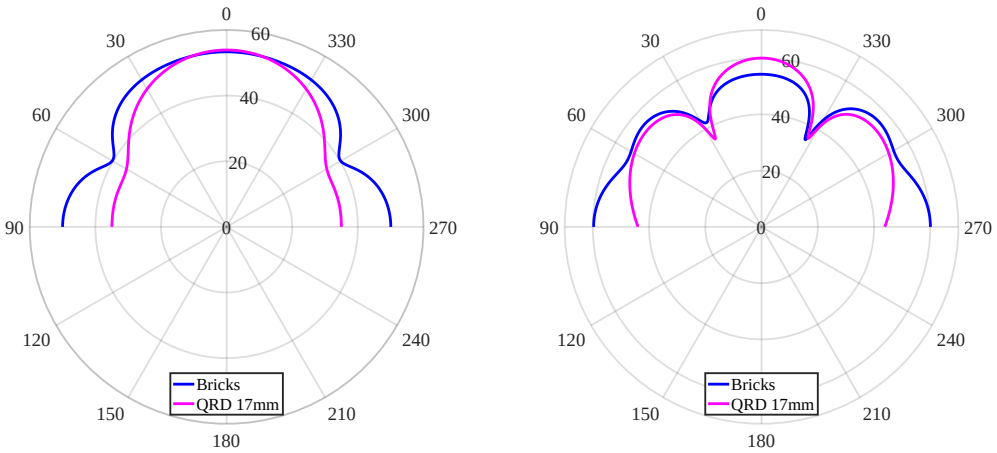

(a) 2500 Hz

(b) 4000 Hz

(c) 5000 Hz

(d) 6000 Hz

Figure 3.16: Far field scattered sound pressure level response of a standard N=7 QRD (17 mm width) and metamaterial brick QRD based on the design described in Table 3.2 at a design frequency of 5000 Hz. The radial grid is in units of dB re 20 μPa.

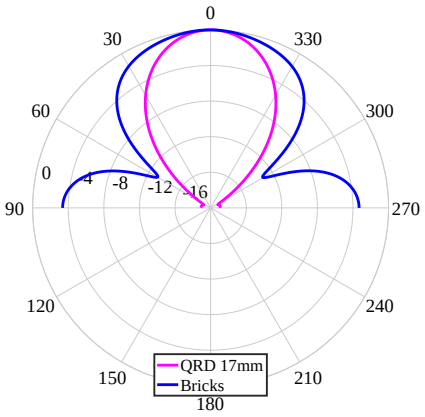

(a) 2500 Hz

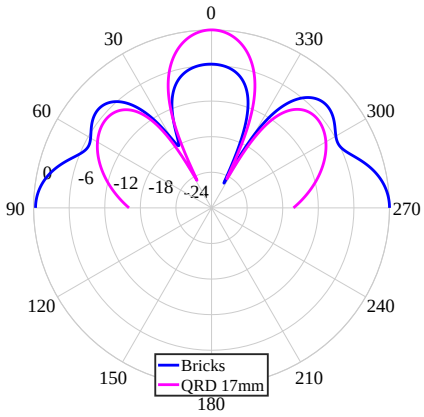

(b) 4000 Hz

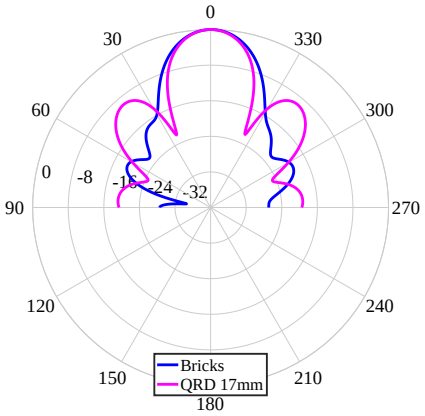

(c) 5000 Hz

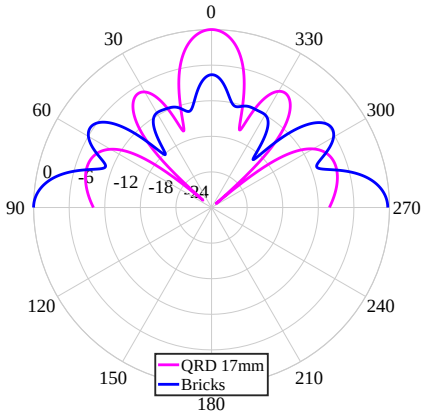

(d) 6000 Hz

Figure 3.17: Scattered field directivity plots (far field SPL of $P(\theta)$ normalized by $P_{\max}$ given by Eq. 3.2) of a standard N=7 QRD (17 mm width) and metamaterial brick QRD based on the design described in Table 3.2 at a design frequency of 5000 Hz. The radial grid is in units of dB.

QRD at 5000 Hz, where one observes that the metamaterial brick QRD clearly does a poorer job diffusing the reflected wave than the QRD does.

Recall that the period width is the length of one period of a QRD. A N=7 QRD at a design frequency of 5000 Hz with block widths of 25 mm has a period width of 175 mm. A N=7 QRD with block widths of 17 mm has a period width of 119 mm. Comparing Fig. 3.14 to Fig. 3.16, it becomes clear that the period width of the QRD plays a role in the diffusion pattern. The response of the 17 mm block width QRD more closely matches that of the metamaterial QRD than the QRD with the 25 mm block width. The smaller QRD also has less defined peaks and nulls and seems to produce a smoother diffusion pattern that is similar to that of the metamaterial QRD. It could be argued that the 17 mm width QRD's performance is better due to this fact, however, as stated in a previous section, it has been proven by Cox and D'Antonio in [3] that QRDs with less than a 25 mm block width encounter serious viscous losses, which are not captured in these models.

Despite some uncertainty in regards to viscous losses, since the models discussed in this section ignored thermoviscous effects, the Memoli brick design has been shown to be a useful metamaterial diffuser design. The next step is to experimentally validate the behavior of the individual bricks.

3.2.2 Description of Experiment and Experimental Results

The goal of the experimental effort presented in this section is to determine the accuracy of simulations and to evaluate their behavior in the presence

of fabrication flaws and losses in both air and the material structure. A plane wave impedance-tube experiment was designed and used to determine the reflected field from each of the bricks calculated in the previous section. The results of these experiments were compared against a new simulation which takes into account the circular nature of the impedance tube, as the previous simulations did not account for this. Both the experimental setup and the simulations will be described in this section.

Metamaterial bricks were fabricated from PLA (polylactic acid) using a Makerbot Replicator 2. They were printed in two separate parts due to fabrication constraints and then joined together in the impedance tube holder, as shown in Fig. 3.18. Figure 3.19 shows several examples of the 3D printed bricks with a pencil included in the photo for scale.

A plane wave impedance-tube experiment was designed and used to extract the magnitude and phase of the reflected field from each of the bricks, thus enabling a comparison of the as-built performance of the bricks with that of the 3D finite element simulation. The impedance tube system is shown in Fig. 3.21. The impedance tube used was a BSWA SW477 impedance tube, which has a built-in source, two microphone ports, and an extension with a rigid termination. Measurements were made using a DataPhysics Quattro dynamic signal analysis system and the associated software SignalCalc ACE, which calculates transfer functions between individual input channels. A schematic of the experimental setup is shown in Fig. 3.20. A source signal was generated by SignalCalc and sent to the output port of the Quattro. A

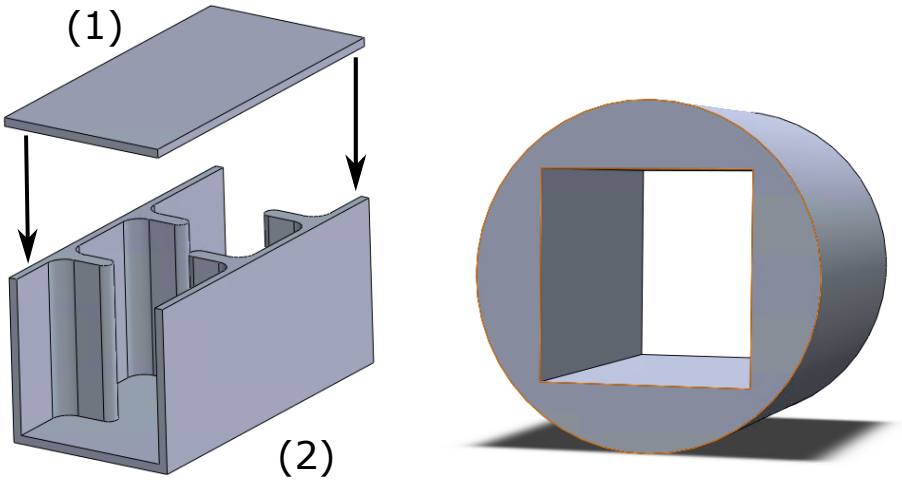

(a) (b)

Figure 3.18: (a) The metamaterial bricks were printed in two separate parts: the top rectangle (1) and the bottom brick (2). Those pieces were then joined together within the impedance tube holder. (b) Impedance tube holder was used to fit the bricks inside the circular impedance tube.

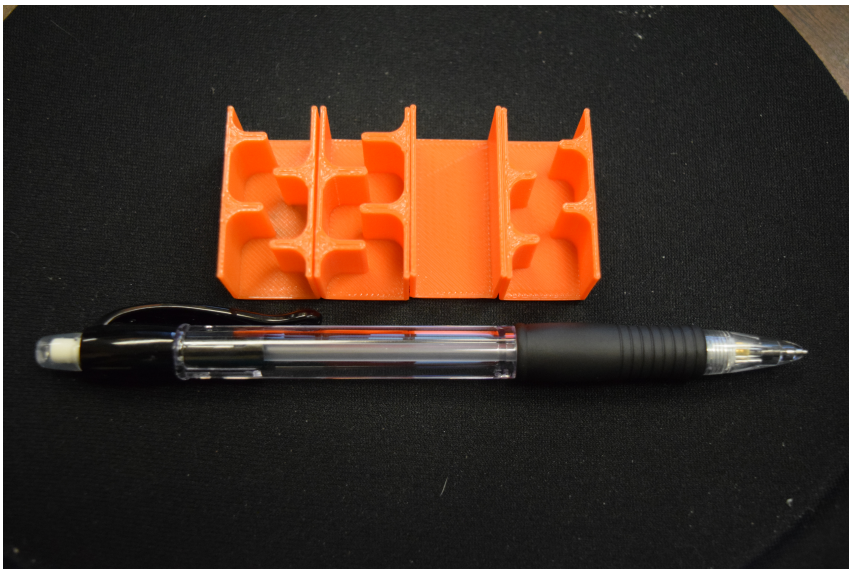

Figure 3.19: Bottom portion of several 3D printed metamaterial bricks.

BNC T-splitter was used to feed both the built-in source of the impedance tube, and Channel 1 of the Quattro system, making it the reference signal for the test. Channel 2 of the Quattro system was used to power the ICP preamplifier of the PCB Piezotronics Inc. 130E21 6.3 mm diameter pressure microphone and acquire the signal. For each measurement, a 1-second-long linear chirp was generated ranging from 200 Hz to 10 kHz. In the frequency band of interest, 1 kHz to 6 kHz, the coherence between the reference and microphone signals was not less than 0.993, indicating that the system was not distorting and that sufficient signal-to-noise was present. The bricks were held within the circular impedance tube with a 3D printed circular holder, which was then placed against the rigid termination so that the top of the brick and holder are flush with the surface of the top of the extension, as shown in Fig. 3.22. Both the printed bricks and the holder have a rough surface due to the 3D printing process. There is also a small gap between the outer diameter of the holder and the inner diameter of the tube, and between the inner diameter of the holder and the brick.

Using the single microphone technique as detailed by Chu [22], a microphone was first placed in port 1, and the transfer function measured there is

$$H_{1\mathrm{V}}(f) = \frac{p_1(f)}{V_{\mathrm{src}}(f)}, \tag{3.3}$$

where $p_1(f)$ is the pressure measured by the microphone and $V_{\mathrm{src}}(f)$ is the reference voltage. The same microphone was then moved to port 2 and again

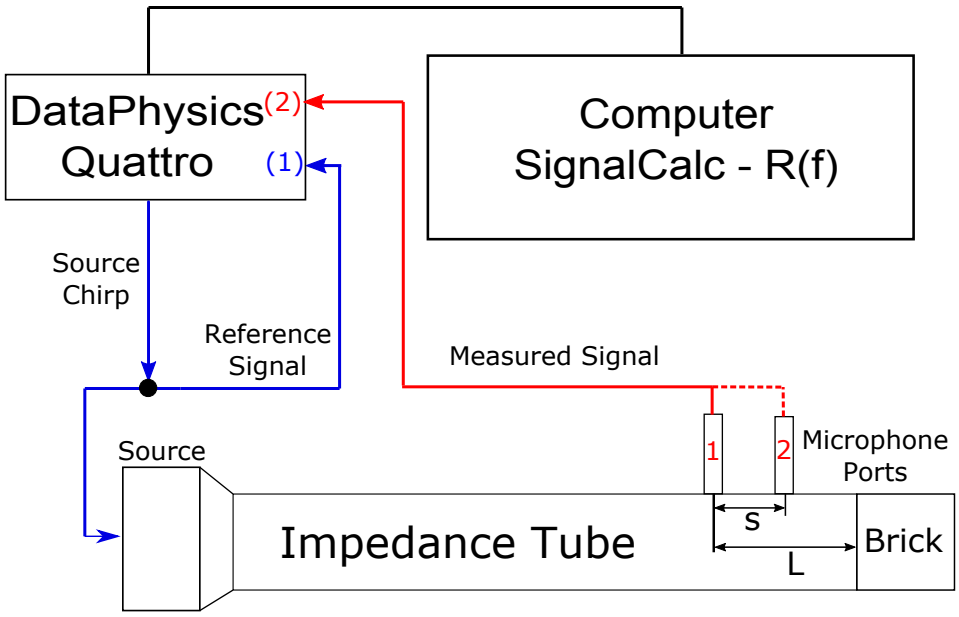

Figure 3.20: A schematic diagram of the experimental apparatus and data acquisition equipment that is used to conduct the tests described in this section.

the transfer function was measured,

$$H_{2V}(f) = \frac{p_2(f)}{V_{src}(f)}. \tag{3.4}$$

For each measurement, the port not occupied by the microphone was plugged with plastic plugs that were included with the impedance tube to minimize the leakage of acoustic energy out of the tube, which leads to inaccuracies in the acquired data.

The reflection coefficient, $R(f)$, can then be calculated using the following relationship [22]:

$$R(f) = \frac{H_{12}(f) - e^{-jks}}{e^{jks} - H_{12}(f)} e^{jk2L}. \tag{3.5}$$

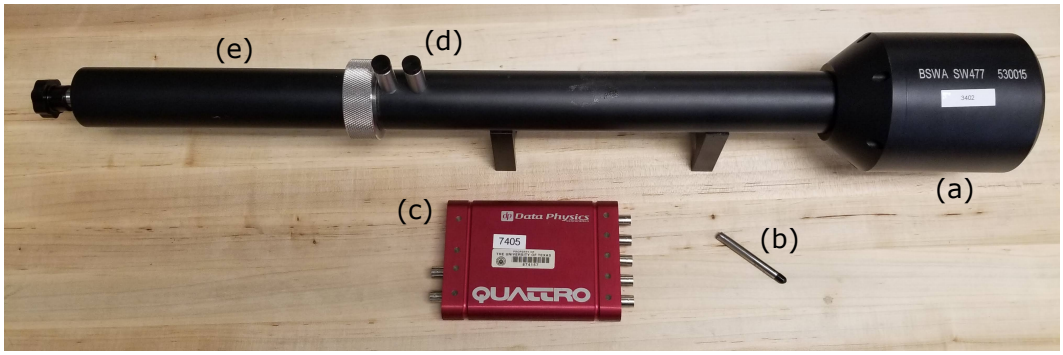

Figure 3.21: Impedance tube system used for measurements, consisting of (a) built-in source, (b) microphone, (c) DataPhysics Quattro dynamic signal analysis hardware, (d) microphone ports, (e) rigid tube extension. The computer for experiment control and data acquisition is not shown in this image.

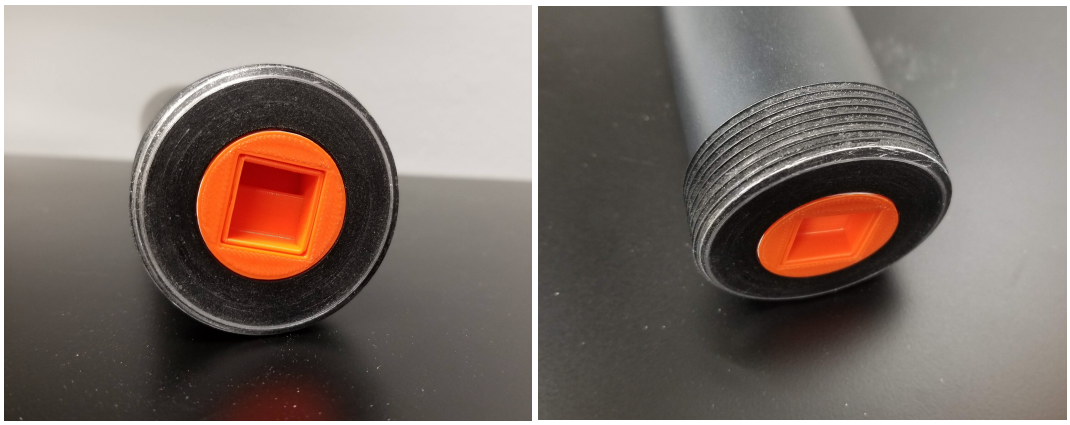

(a) (b)

Figure 3.22: (a) 3D printed brick and holder inside test section of impedance tube. (b) Metamaterial brick flush with mating surface of impedance tube test section.

Here

$$H_{12}(f) = \frac{H_{2\mathrm{V}}(f)}{H_{1\mathrm{V}}(f)} \tag{3.6}$$

is the transfer function between the two microphone locations, f is the frequency, and k is the wavenumber ($k = 2\pi f/c$). The temperature was not measured before the experiment, thus the sound speed of air used for these calculations was $c = 343$ m/s. The distance between the microphone ports was $s = 22.5$ mm, and the distance from the first microphone port to the surface of the brick was $L = 40.7$ mm, as shown in Fig. 3.20. The absorption coefficient, α, was calculated using [3] [1],

$$\alpha(f) = 1 - |R(f)|^2. \tag{3.7}$$

Each of the 4 bricks in the 1D QRD considered in the previous section were fabricated and tested in the impedance tube. Figure 3.23 compares the reflection coefficient magnitude and phase and the absorption coefficient of each brick as measured using the system and measurement method described above. These results show that the as-built metamaterial bricks will absorb considerable amounts of acoustic energy in narrowband frequency regions. Bricks 1 and 4 have an α of almost unity, indicating almost perfect absorption at those frequencies. Because the absorption was only at narrowband frequencies, it was assumed to be the result of a quarter-wave resonance, with the bricks acting as quarter-wave resonators.

The initial simulations detailed in the previous section were unable to capture the behavior observed in the experiment, even when using the ther-

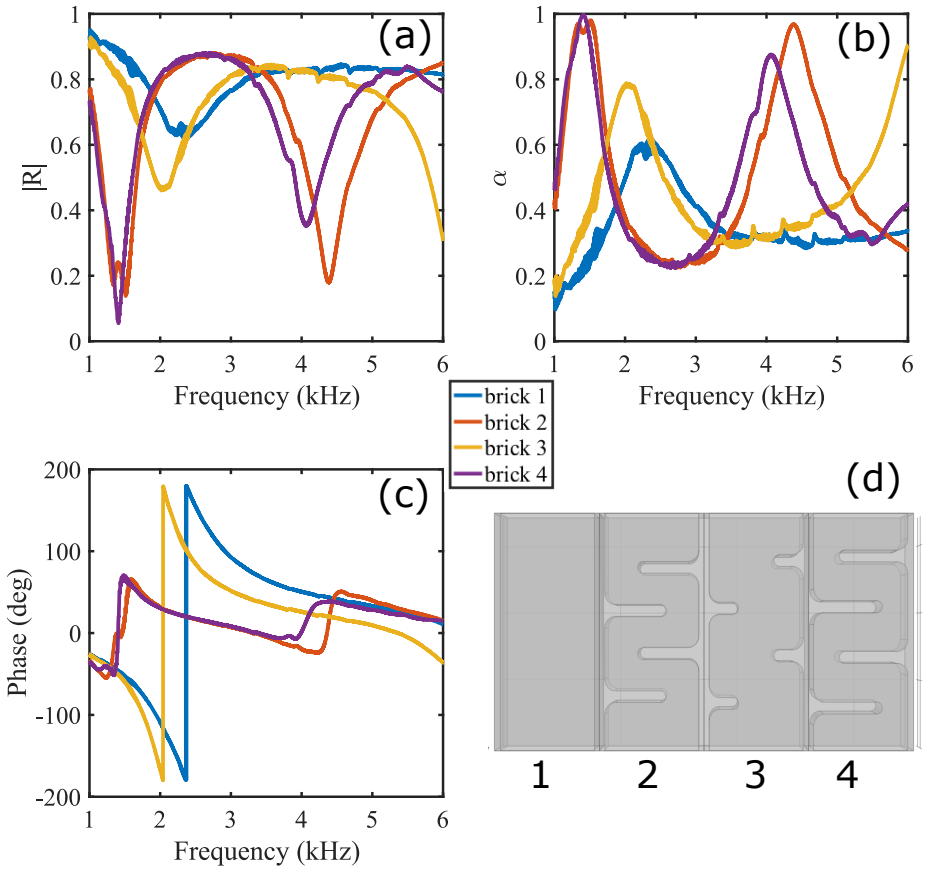

Figure 3.23: Comparison of the experimental results of the four bricks, where (a) compares the magnitude of the reflection coefficient, (b) compares the absorption coefficient, α, and (c) compares the phase of each of the bricks. (d) shows the four bricks being compared as labeled in the legend. The coherence between the reference and microphone signals for this set of measurements was not less than 0.993 over the entire frequency range.

moviscous acoustics module in COMSOL, which computes both thermal and viscous losses, suggesting that either the simulation did not properly capture the details of the experiment, or that the experimental apparatus was not properly configured to measure the phenomena of interest. The latter point was addressed by performing numerous test iterations and troubleshooting at all stages. The experimental results did not show significant variation from configuration to configuration. It was therefore deduced that it was most likely that the previous simulations did not adequately capture losses in the system as it was implemented. A new simulation was therefore implemented that made use of the "Narrow Regions Acoustics" physical model within the Pressure Acoustics module in COMSOL. This module was created to properly capture the lossy effects of the viscous and thermo-viscous boundary-layer in channels and ducts. The material properties for this model are detailed in Table 3.3.

Further, the refined simulation replicated the impedance tube measurement configuration by making the simulation area circular and by including the presence of the impedance tube holder, as shown in Fig. 3.24. The results of this improved simulation are compared to the experimental results in Figs. 3.25-3.27.

These results are enlightening. For bricks 1 and 3, the simulation predicts the correct frequency for the absorption peak, though not the correct value. The phase is also interesting. While phase is a useful metric for diffuser design, it also interesting because it shows the frequencies at which resonance

Property	Variable	Value	Unit
Temperature	T	293.15	K
Speed of sound	c	343	m/s
Density	ρ	1.21	kg/m^3
Dynamic viscosity	μ	1.814E-5	Pa·s
Bulk viscosity	μ_{B}	0.7μ	Pa·s
Ratio of specific heats	γ	1.4	
Thermal conductivity	k	2.5768E-2	W/(m·K)

Table 3.3: Material properties of air used in the finite element simulations.

Property	Variable	Value	Unit
Density	ρ	1300	kg/m^3
Young's modulus	E	3100	MPa
Poisson's ratio	ν	0.33	

Table 3.4: Material properties of PLA used in the finite element simulations.

Brick	f_{exp} (kHz)	f_{FEM} (kHz)	$\Delta f / f_{\mathrm{exp}}$
1	2.39	2.36	1%
2	1.5	1.3	13%
3	2.0	2.12	6%
4	1.41	1.25	11%

Table 3.5: Percent error of the frequency of peak absorption between the model and experiment for each brick from the results displayed in Fig. 3.26.

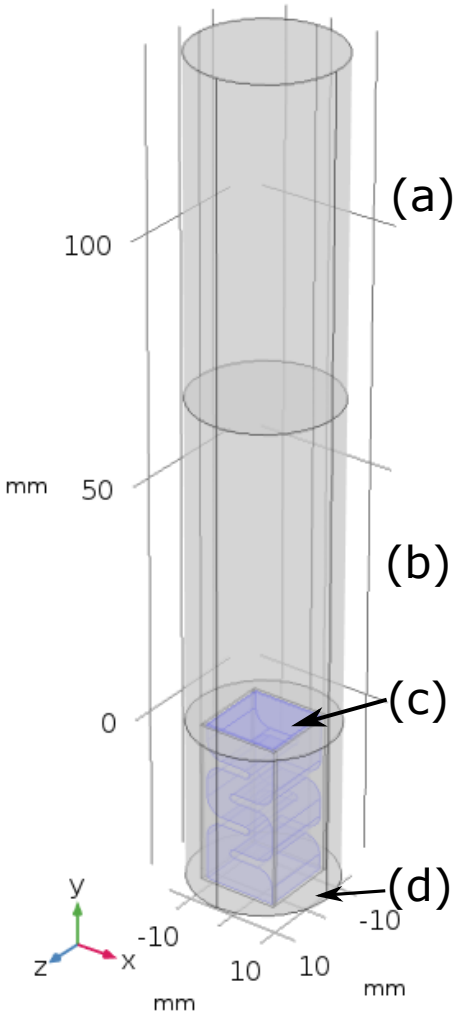

Figure 3.24: Impedance tube simulation with four sections: (a) perfectly matched layer, (b) background pressure field, (c) PLA brick, (d) PLA brick holder. The highlighted blue area is the air channel within the brick where the Narrow Regions Acoustics module is used. Regions (a) and (b) have rigid boundaries.

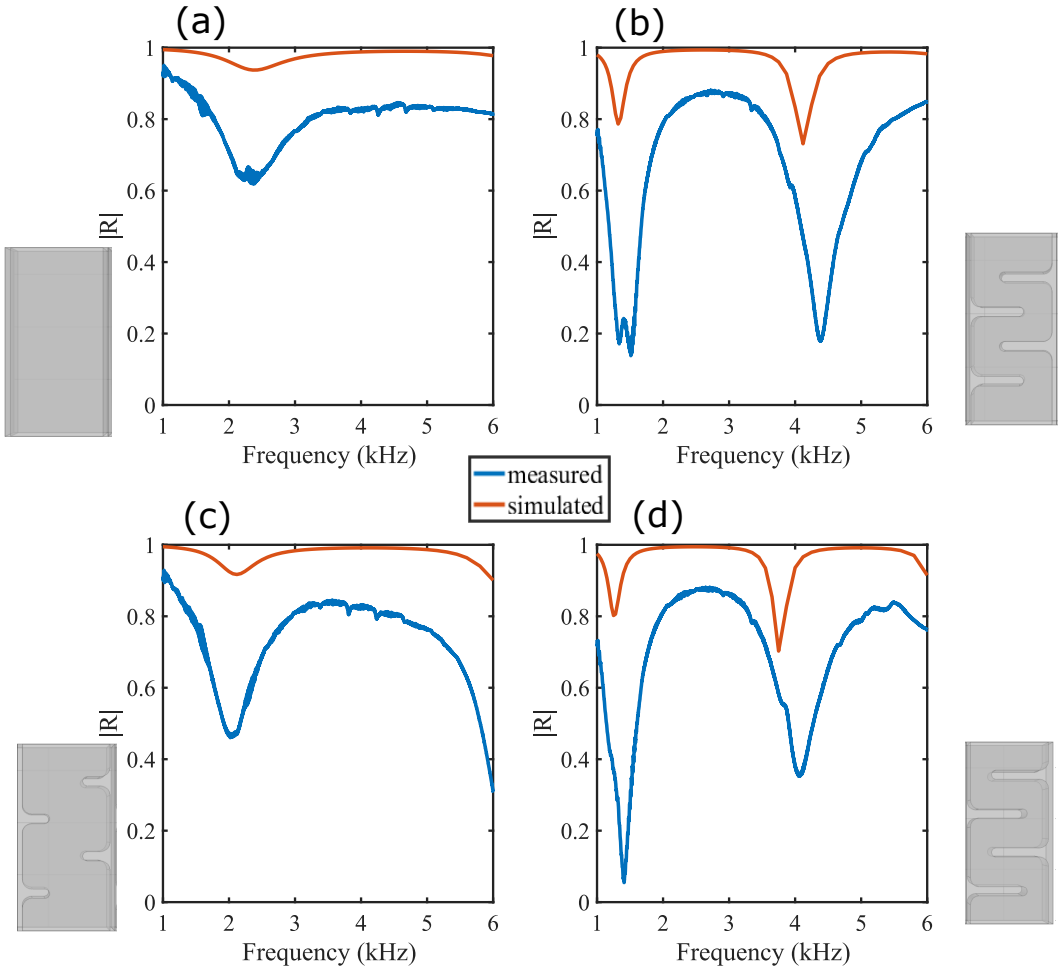

Figure 3.25: Comparison of the measured and simulated magnitude of the reflection coefficient, $|R|$, for each of the four bricks: (a) brick 1, (b) brick 2, (c) brick 3, (d) brick 4. The commercial finite element software, COMSOL, was used to produce these simulated curves, as described in the text. For each brick, the frequency of the measured null is close to the frequency of the predicted nulls. However, the null is more significant in the experimental results than in the simulated results. For bricks 2 and 4 (plots b and d), the simulation more accurately predicts the frequency of the first null than the second.

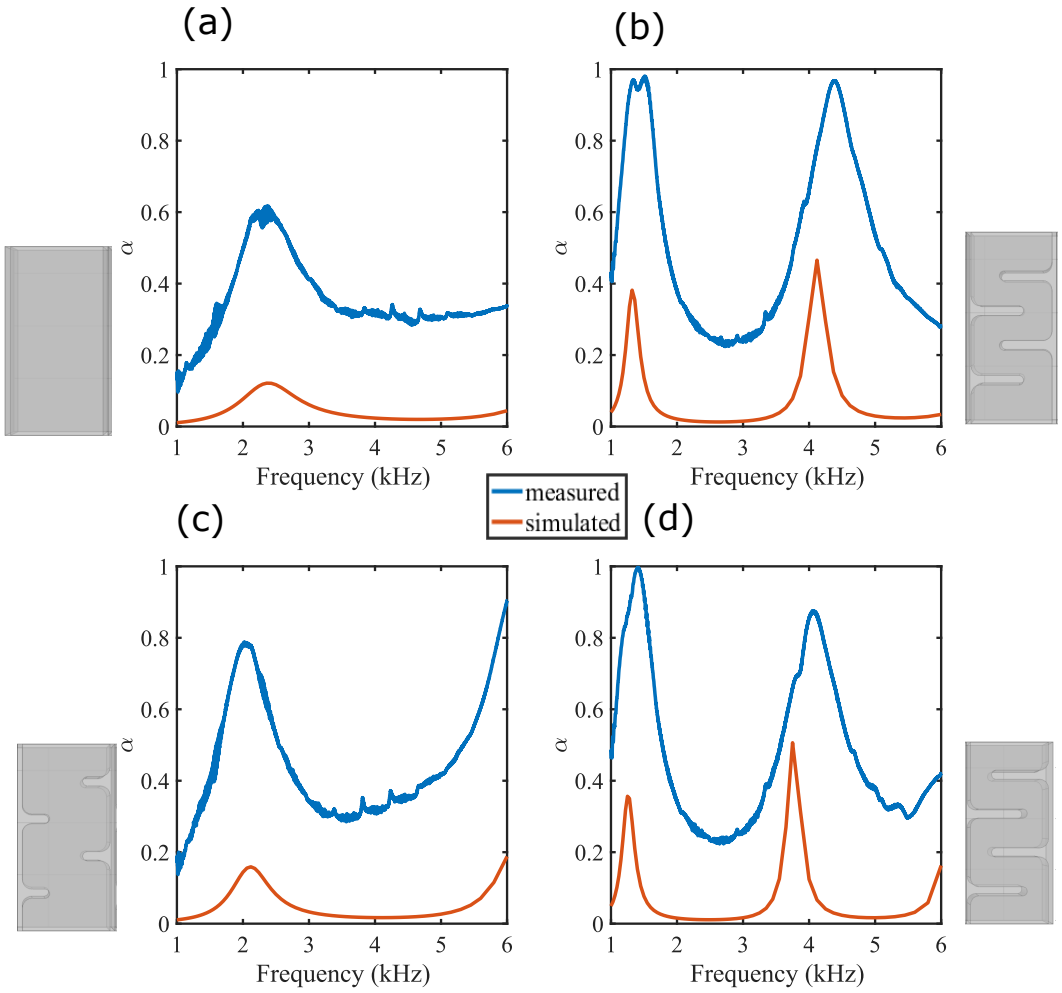

Figure 3.26: Comparison of the measured and simulated absorption coefficient for each of the four bricks: (a) brick 1, (b) brick 2, (c) brick 3, (d) brick 4. The commercial finite element software, COMSOL, was used to produce these results. Similar to Fig. 3.25, the simulation predicts the frequency of the first absorption peak correctly, but not the magnitude of it. Again, for bricks 2 and 4 (plots b and d), the simulation does a better job of predicting the first peak than of the second.

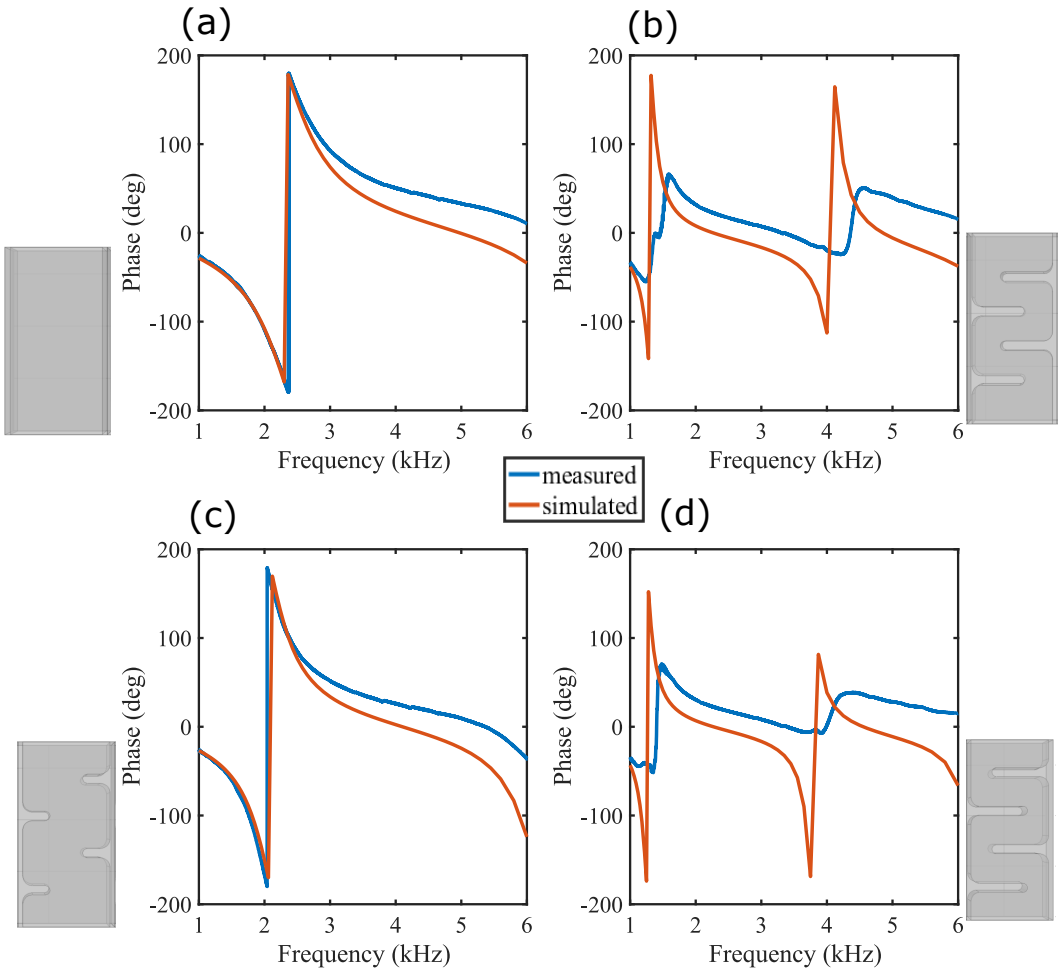

Figure 3.27: Comparison of the measured and simulated phase of the reflection coefficient for each of the four bricks: (a) brick 1, (b) brick 2, (c) brick 3, (d) brick 4. The commercial finite element software, COMSOL, was used to produce these results. Like the previous plots, the simulated and experimental results are in excellent agreement for bricks 1 and 3, but much less so for bricks 2 and 4.

occur. At resonance, the reactive components of a dynamic system cancel out, leading to the phase equaling zero at resonance. For bricks 1 and 3, the measured and predicted phase is in excellent agreement. However, the differences between the measured and predicted phase are significant for bricks 2 and 4. For all bricks, the absorption prediction from the simulation is significantly less than the measured absorption. This could possibility be due to the fact that there are losses in the tube that are not accounted for in the model, such as leakage to the environment through the microphone ports, or the losses in the as-built PLA material. Table 3.5 provides a quantification of the error between the simulation and experiment for the frequencies of peak absorption.

Referring back to Fig. 3.11, bricks 1 and 3 have a more open path, and bricks 2 and 4 have a more tortuous path. According to the initial results of the experiment, there seems to be a relationship between the tortuous path and the model-experiment comparison being so different. To investigate, and to determine whether the discrepancies have to do with the PLA material or the 3D printing process, an additional experiment was conducted in which two bricks, one being more open, and the other having a more tortuous path, were fabricated using two different types of materials: aluminum and PLA. The aluminum sample was fabricated using traditional end-mill machining, and the PLA sample was fabricated using the same 3D printing process as used to create the bricks discussed above. The samples are shown in Fig. 3.28. Experiments to measure the complex reflection coefficient, and thus, the absorption coefficient, were conducted on all four bricks. The bricks were also

Brick	H	W	b_l/λ_0	b_s/λ_0	p_r/λ_0
Open	λ_0	$\lambda_0/2$	0.1667	0.5	0.1
Tortuous	λ_0	$\lambda_0/2$	0.7	0.16111	0.1

Table 3.6: Brick parameters for open and tortuous brick for a design frequency of 5000 Hz with a wavelength of λ. Here, $\lambda_0 = \lambda/2$, H is the height of the brick, and W is the width of the brick. See Fig. 3.9 for a schematic of the brick.

Property	Variable	Value	Unit
Density	ρ	2700	$\mathrm{kg/m^3}$
Young's modulus	E	70000	MPa
Poisson's ratio	ν	0.33	

Table 3.7: Material properties of aluminum used in the finite element simulations.

modeled in COMSOL using both the Acoustics and Solid Mechanics modules, which are coupled using the Acoustic-Structure Interaction multiphysics. The PLA was approximated as homogeneous in the model, even though it is not in the as-built configuration. The experimental and simulated results are compared in Figs. 3.29-3.31. Table 3.7 gives the properties of aluminum used in the simulation, and Table 3.8 shows the percent error between the experimentally obtained frequency of maximum absorption for the aluminum and PLA samples as compared to that of the simulation.

The simulation results for the aluminum and PLA bricks are identical for both bricks; however, the experimental and simulated results are not.

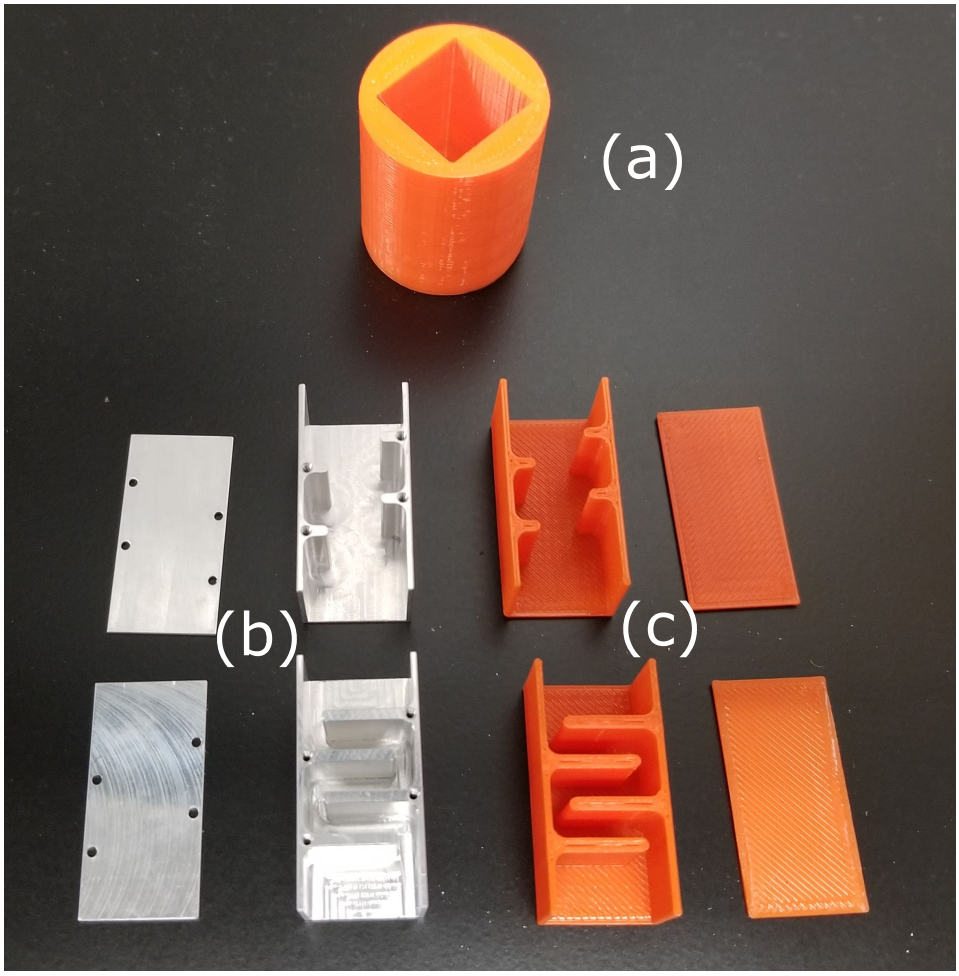

Figure 3.28: (a) PLA brick holder, (b) aluminum bricks, (c) 3D printed PLA bricks. The top row will be referred to as open brick, while the bottom row will be referred to as the more tortuous brick. See Table 3.6 for details on the brick parameters.

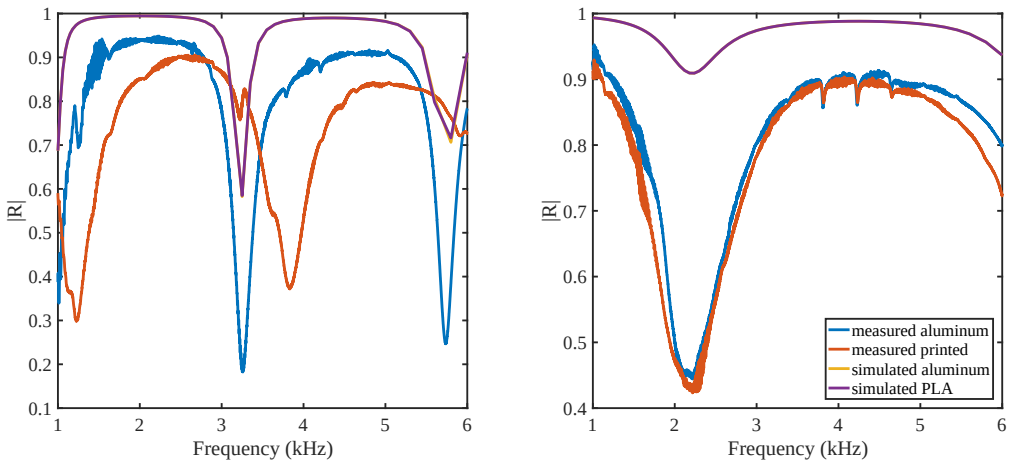

(a) Tortuous brick (b) Open brick

Figure 3.29: Reflection coefficient of aluminum bricks versus PLA bricks, simulated and measured results. The yellow aluminum simulation curve is nearly perfectly overlaid by the purple PLA simulation curve, and thus not visible in the figure.

Brick	f_{FEM} (kHz)	f_{alum} (kHz)	f_{PLA} (kHz)	$\frac{\Delta f_{\text{alum}}}{f_{\text{FEM}}}$	$\frac{\Delta f_{\text{PLA}}}{f_{\text{FEM}}}$
Open	2.24	2.21	2.21	1%	1%
Tortuous	3.25	3.25	3.82	0%	25%

Table 3.8: Percent error of the frequency of peak absorption between the aluminum and PLA bricks for both simulated and measured results displayed in Fig. 3.30.

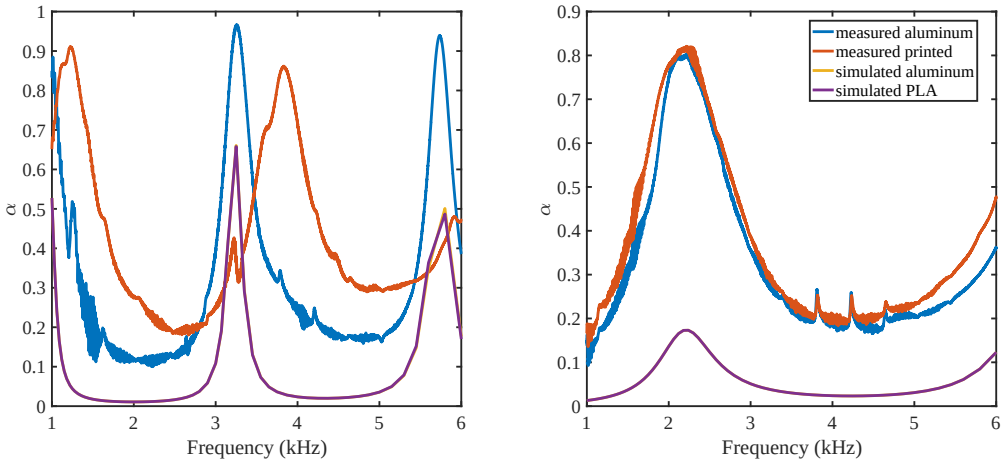

(a) Tortuous brick (b) Open brick

Figure 3.30: Absorption coefficient of aluminum bricks versus PLA bricks, simulated and measured results. The yellow aluminum simulation curve is nearly perfectly overlaid by the purple PLA simulation curve, and thus not visible in the figure.

For the more open brick, the aluminum and PLA experimental results are quite similar, and the simulation is able to predict the frequency of highest absorption with a difference of only 1%, though still not the magnitude of the absorption coefficient. For the more tortuous bricks, the aluminum experimental results match the simulated prediction for the frequency of peak absorption, but the magnitude of the predicted absorption is less than that of the experimental aluminum results. The PLA experimental results show differences in the frequency of peak absorption of 25% as compared to that of the simulated and aluminum experimental results, and the magnitude of the absorption differs as well. Clearly, something about a more tortuous path and the PLA material result in more absorption than is predicted in the simulation.

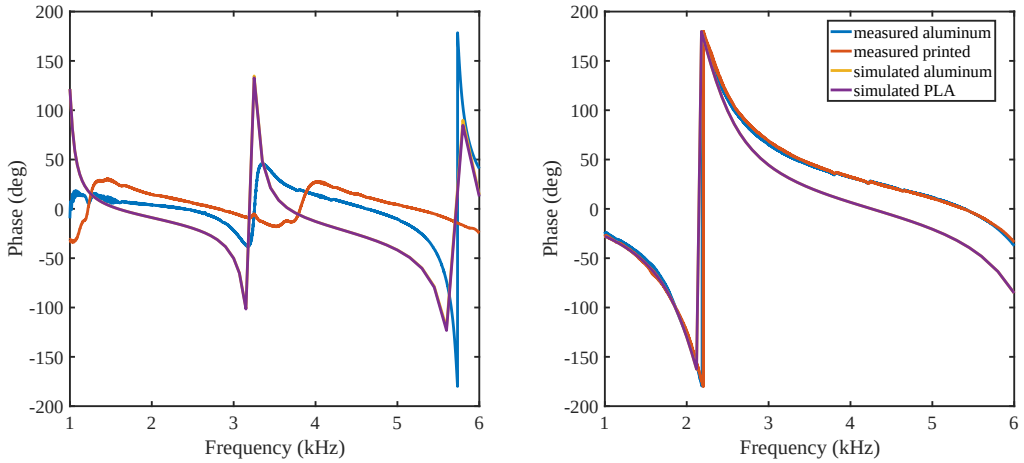

(a) Tortuous brick (b) Open brick

Figure 3.31: Phase of the reflected field of the aluminum bricks versus the PLA bricks, simulated and measured results. The yellow aluminum simulation curve is nearly perfectly overlaid by the purple PLA simulation curve, and thus not visible in the figure.

There are several possible reason for discrepancies described above. Perhaps the compliance of the as-fabricated PLA samples causes the location of the resonance frequency to shift, and the finite element simulation is unable to capture this since the 3D printing process may induce a change the material properties. The 3D printing process also causes the PLA material to be inhomogeneous throughout the structure, which could also change the location of the resonance. The model assumes that the material is homogeneous throughout the structure, and thus is unable to take this into account as well.

Memoli's bricks lack an analytical solution to determine the resonance frequency due to the openness of its design. In addition, the height of the bricks is restricted to around half the wavelength of the design frequency in order to

induce sufficient phase change for the creation of a metamaterial QRD, which makes the bricks taller than a standard QRD. Memoli's bricks are therefore not ideal for creating a thinner diffusing surface. Thus, a decision was made to abandon this design and choose a different one. The coiled space design proposed by Li [23] has both an approximate analytical solution for the phase of the reflected wave, and a height that can be effective even when the overall depth is 1/20th the wavelength of the design frequency. The next section will introduce this design and cover the results of using Li's coiled space design to create metamaterial diffusers.

3.3 Li Coiled Space

Due to the struggles with Memoli's brick design presented in the previous section, a decision was made to refocus on the brick design presented by Li and colleagues. Li et al. detail in [23] coiled space structures whose phase change is based on the width of the structure. Li's design is significantly smaller than Memoli's design: $\mathcal{O}(\lambda/20)$ versus $\mathcal{O}(\lambda/2)$ while still achieving a 180° phase shift. In addition, due to the relative simplicity of the structure, unlike in the more open design created by Memoli et al., an approximate analytical expression exists to estimate the resonance frequency, where one observes a significant phase shift between the incident and reflected waves. However, Li's paper details these bricks only in 2D. Thus, the first step was to verify Figure 1 in Li's paper in 2D, which provides the parameters for the bricks and the phase shift of each brick. Afterwards, the bricks were modeled

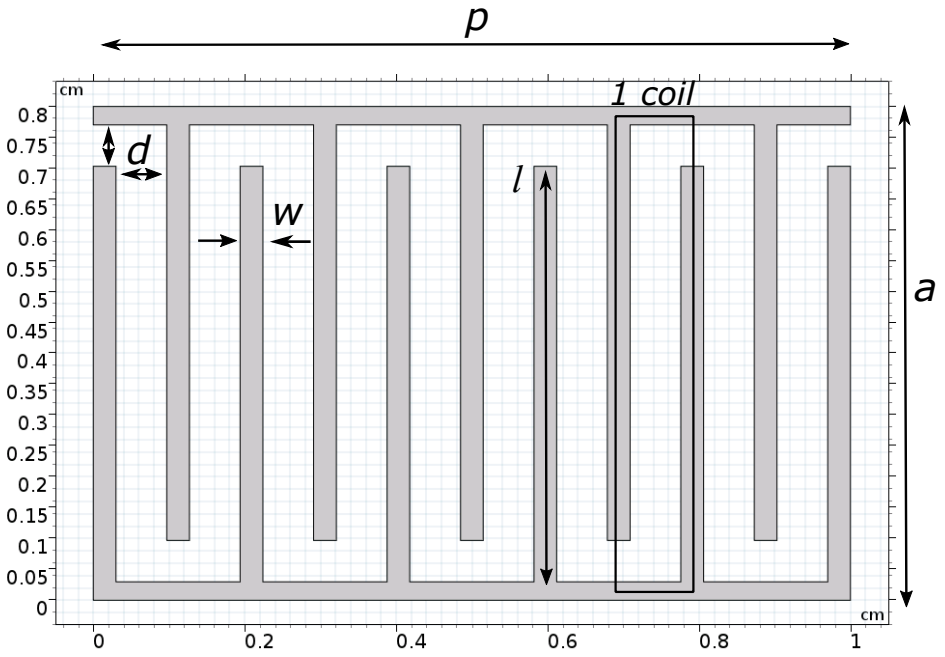

Figure 3.32: Schematic diagram of a brick. See Table 3.9 for parameter details.

with a finite depth to create a 3D object in order to replicate how they would be fabricated in order to create a diffusing surface. These bricks were then modeled in 3D using COMSOL to verify that a 3D system could replicate the results presented by Li and colleagues. This will be detailed in the following sections.

3.3.1 Model Validation

Figure 1 in Li's paper details the parameters and phase changes for the bricks. Most of the structure is based on height, p, with width, a, as the other independent variable, as shown in Table 3.9. To estimate the resonance frequency, an analytical solution was derived for the bricks. From the Memoli

Parameter	Variable	Equation	Value
frequency	f		1750 Hz
width	a		0.4–0.8 cm
coils	N		10
wavelength	λ	c/f	0.196 m
height	p	$\lambda/19.6$	1 cm
channel width	d	$0.067p$	0.067 cm
bar width	w	$0.03p$	0.03 cm

Table 3.9: Brick parameters proposed by Li [23]. See Fig. 3.32 for a schematic of the brick.

brick experiments, it has been determined that a coiled space structure acts as a quarter-wave resonator. The effective length, L_{eff}, is thus 1/4 of the resonance frequency wavelength, λ_{res},

$$L_{\text{eff}} = \frac{\lambda_{\text{res}}}{4}, \tag{3.8}$$

and the resonance frequency, f_{res}, can be determined using

$$f_{\text{res}} = \frac{c}{4L_{\text{eff}}}. \tag{3.9}$$

The reflection coefficient, R, can be calculated analytically using the effective length in Eq. 3.10,

$$R = \frac{j\cot(kL_{\text{eff}}) + \frac{d}{a}}{j\cot(kL_{\text{eff}}) - \frac{d}{a}}. \tag{3.10}$$

In order to verify that the finite element simulations were in agreement with the archival literature, the parameters of coiled space structures were

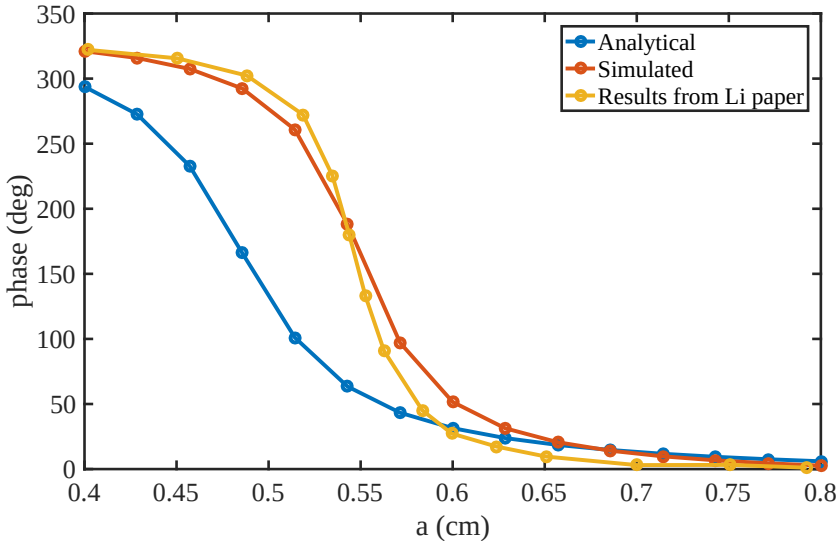

Figure 3.33: Width, a, vs phase (deg) plot comparing analytical, simulated, and Li's solution.

replicated in both a COMSOL simulation and the analytical model. A sweep was conducted across the widths, 0.4–0.8 cm. Using the Plot Digitizer program [24], the data from the plot in Li's work was extracted and plotted on the same plot as the simulations and the analytical results in Fig. 3.33. The COMSOL simulation most closely resembles Li's results, though the analytical model approaches both the other results as the width, a, increases. This discrepancy could possibly be due to the fact that the analytical result models a true quarter-wave resonator using the effective length of the brick, and not the actual structure of the brick. The coiled space structure of the brick could induce more viscous and thermoviscous boundary layer losses than that of a straight quarter-wave resonator. Figure 1 in Li's paper also contains a plot of

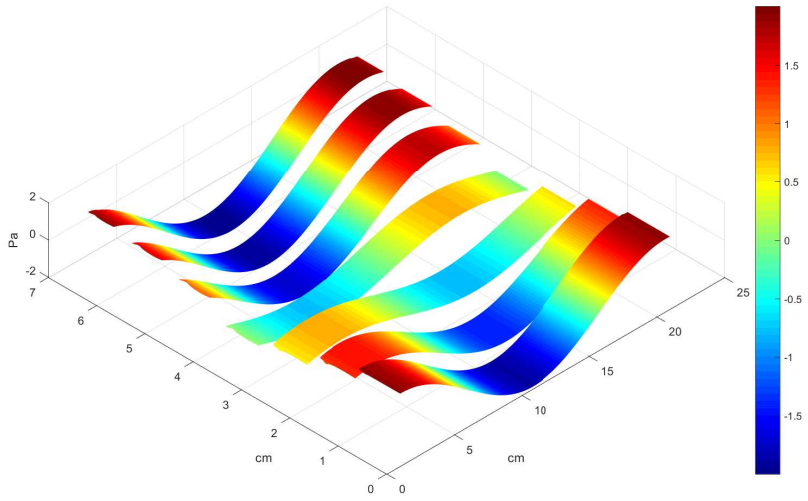

Figure 3.34: Height expression plots of the total pressure field showing the phase shift of each of the eight bricks. The colorbar is in units of Pascals.

the pressure strips of each of the 8 bricks. These are also replicated using a COMSOL simulation in Fig. 3.34.

Having verified that these bricks are indeed able to change the phase of the reflected wave, the bricks are extended into 3D and modeled using a COMSOL simulation.

3.3.2 3D Finite Element Analysis

The original bricks had two independent variables, frequency, f, and width, a, with the height of the brick tied to frequency. In addition, the channel width, d, was both the opening into the brick, and the width of the channel. In order to vary the number of coils within the brick, the channel width inside

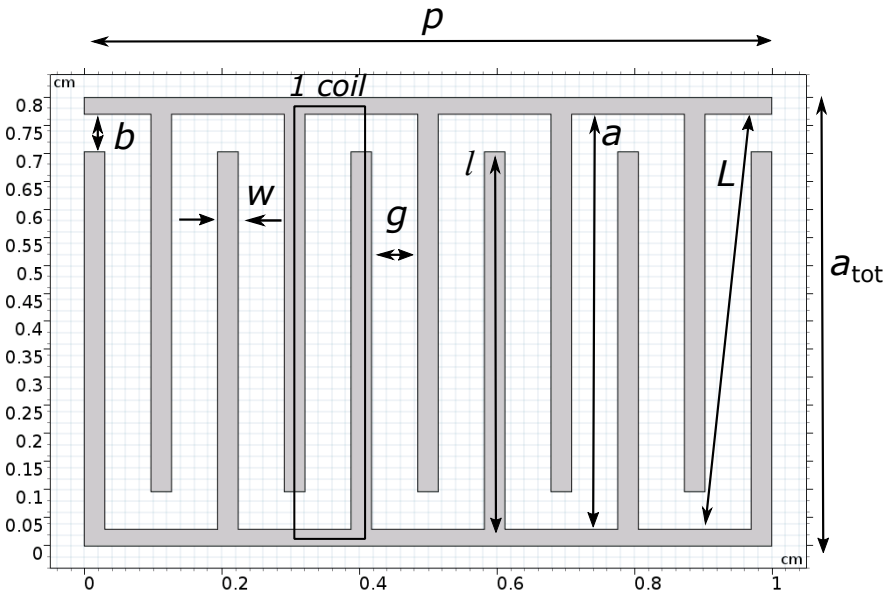

Figure 3.35: Schematic diagram of a brick. See Table 3.10 for parameter details.

the brick must change. Thus, several new parameters were introduced and are detailed in Table 3.10 and Fig. 3.35.

Since the approximate pathlength can be computed analytically, the absorption and phase response of the bricks can be calculated for one frequency, then easily scaled to find the needed values by normalizing the depth and width by wavelength. An arbitrary frequency of 1500 Hz was chosen, and the simulated bricks are shown in Fig. 3.36. The normalized results are shown in Figs. 3.37 through 3.39 for the different number of coils.

From these figures, it is clear that as the number of coils increases, the increase in width does not affect the phase or absorption coefficient, as both of those approach zero at greater widths. There is also an increase in absorption

Parameter	Variable	Equation
height	p	
total width	a_{tot}	
coils	N	
bar width	w	$0.03p$
inner width	a	$a_{\text{tot}} - 2w$
channel width	b	$0.067p$
bar length	l	$a - 2w - b$
bar spacing	g	$\frac{p-(N+1)w}{N}$
pathlength	L	$\sqrt{a^2 + (g+w)^2}$
effective length	L_{eff}	NL

Table 3.10: Additional brick parameters are added to Table 3.9. The pathlength, L, and effective length, L_{eff} were not included in Li's paper and added for the purposes of the research in this thesis.

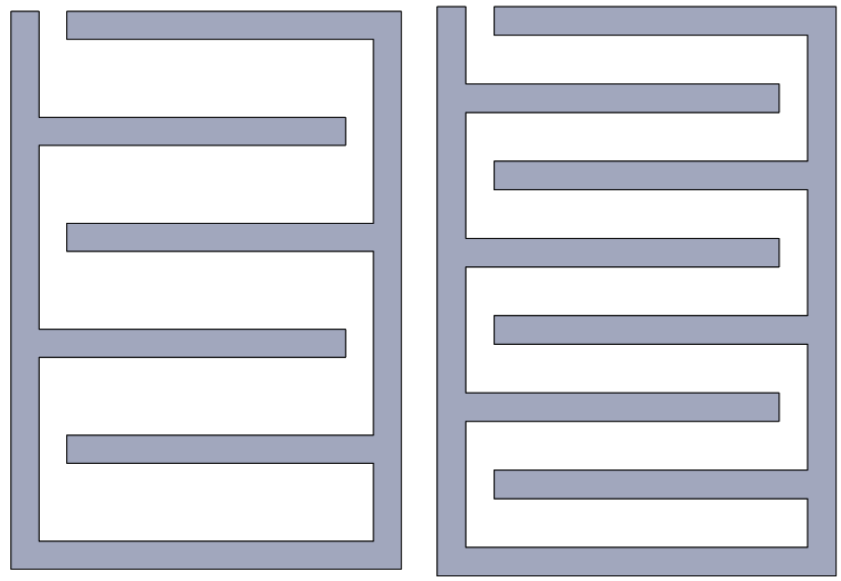

(a) 5 coils

(b) 7 coils

(c) 9 coils

(d) 10 coils

Figure 3.36: A cross section of the simulated bricks showing the difference in geometry for bricks with different numbers of coils. The simulated results of these bricks are shown in Figs. 3.37 and 3.39.

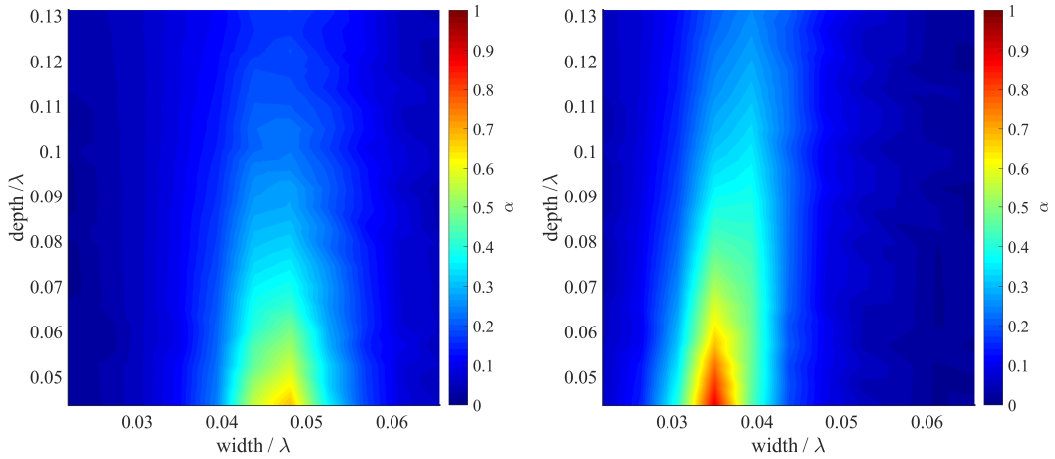

(a) 5 coils

(b) 7 coils

(c) 9 coils

(d) 10 coils

Figure 3.37: Absorption coefficient of the bricks shown in Fig. 3.36 with parameters normalized by wavelength.

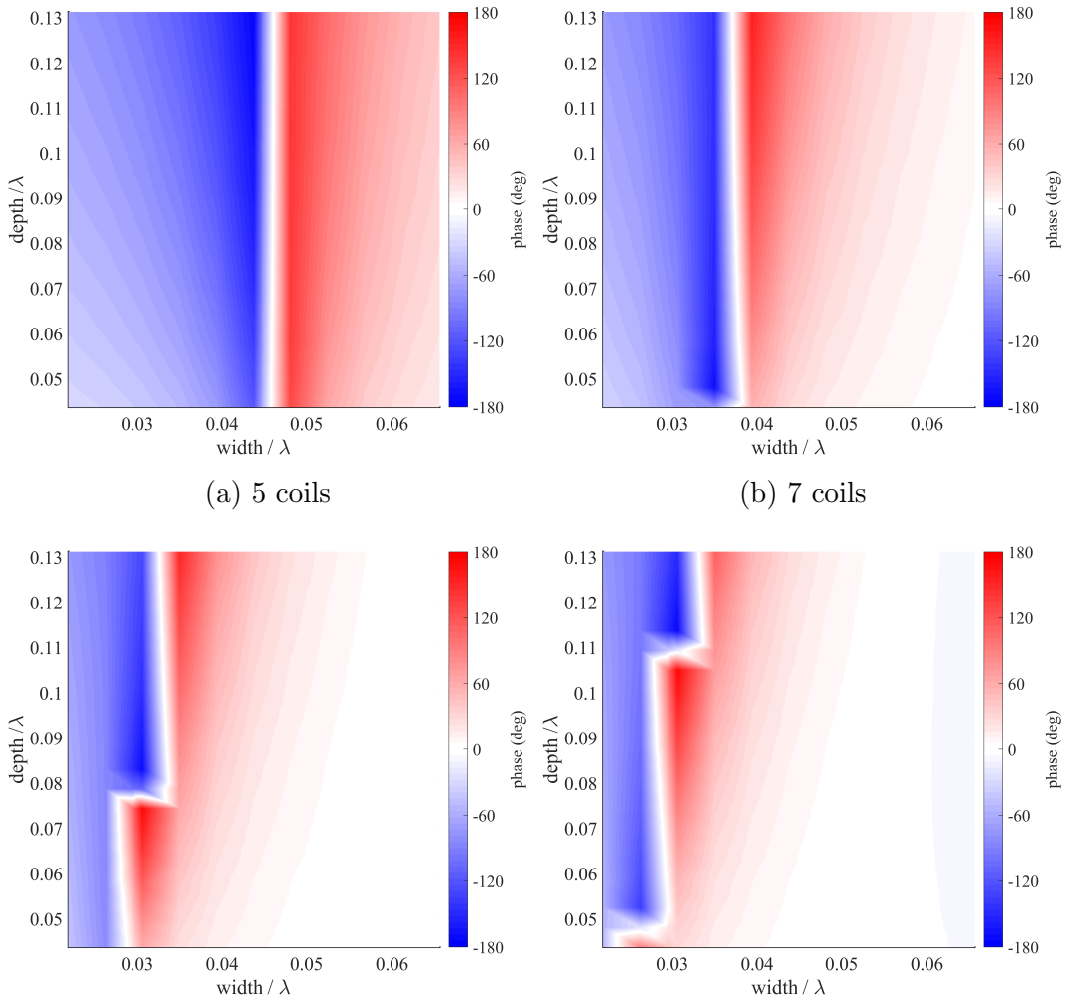

(a) 5 coils

(b) 7 coils

(c) 9 coils

(d) 10 coils

Figure 3.38: Reflected wave phase of the bricks shown in Fig. 3.36 with parameters normalized by wavelength.

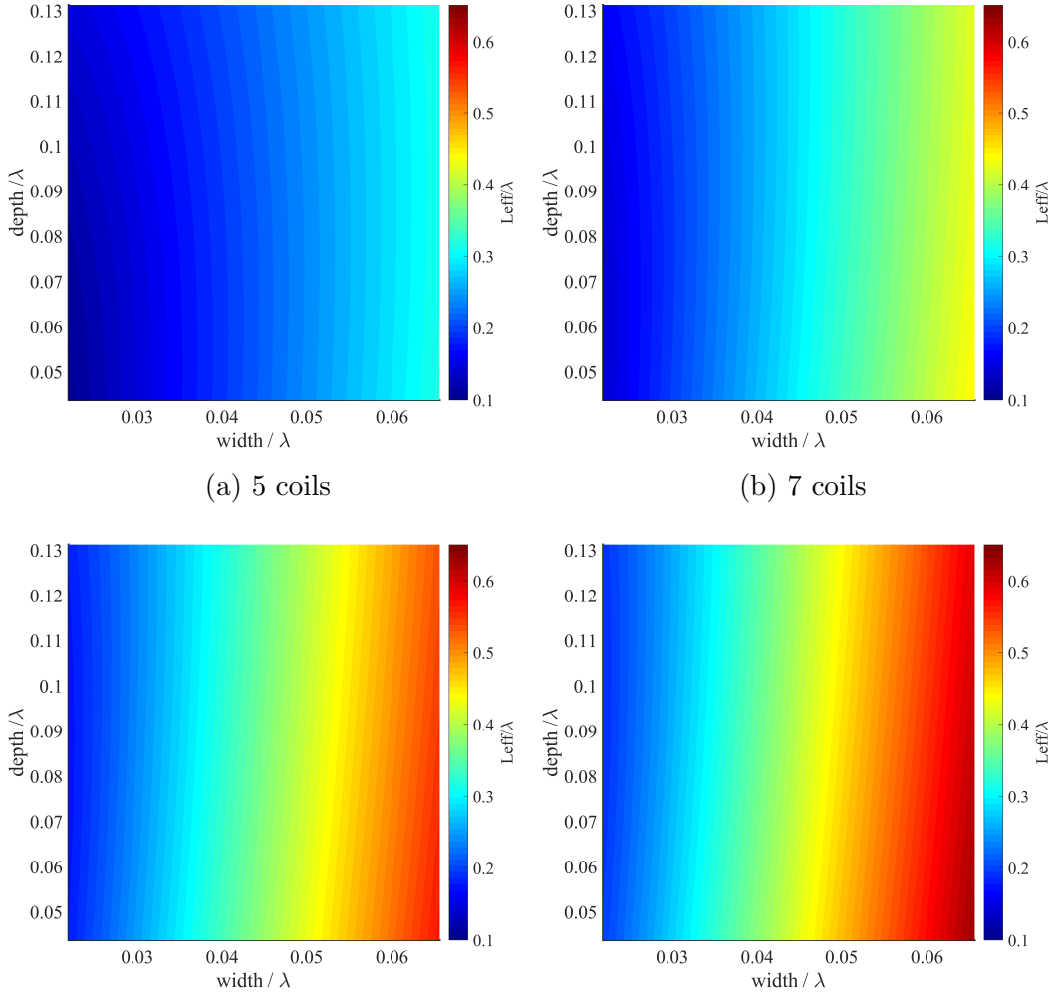

(a) 5 coils

(b) 7 coils

(c) 9 coils

(d) 10 coils

Figure 3.39: Effective length of the bricks shown in Fig. 3.36 with parameters normalized by wavelength.

in the bricks with more coils. Figure 3.39 shows that the width contributes the greatest to an increase in the effective length, whereas the depth contributes less.

In order to keep about the same dimensions as Li's structures, a decision was made to switch the design frequency to 2000 Hz. In addition, in order to make bricks that are 3D printable, the beam width must be at least 1 mm. Thus, the minimum height of the brick was set to be 2 cm, and the bar width was set to be 5% of the height. For ease of calculation, the channel width was also set to be 5% of the height. For clarity, the new values are given in Table 3.11. Equation 2.44 is again used to find the blocks heights of a 1D QRD with a design frequency of 2000 Hz, which are given by

$$h_n = [50 \quad 38 \quad 0 \quad 25 \quad 25 \quad 0 \quad 38] \text{ mm} \tag{3.11}$$

The phase shift for each depth is given in Table 3.12. A parametric sweep was conducted as before, except this time, there are three independent variables: height, width, and coils. This sweep will attempt to find a combination of variables that will produce the same phase shift values as those listed in Table 3.12 at 2000 Hz; the results are listed in Table 3.13.

Now that the brick parameters have been chosen, another simulation was run which calculates the response of the bricks for a range of frequencies, the results of which are plotted in Fig. 3.41. These figures show the simulated resonance frequency for each brick, which are then compared to the analytically calculated resonance frequency. The simulated and analytically calculated

Parameter	Variable	Equation
height	p	
total width	a_{tot}	
coils	N	
bar width	w	$0.05p$
inner width	a	$a_{\text{tot}} - 2w$
channel width	b	$0.05p$
bar length	l	$a - 2w - b$
bar spacing	g	$\frac{p-(N+1)w}{N}$
pathlength	L	$\sqrt{a^2 + (g+w)^2}$
effective length	L_{eff}	NL

Table 3.11: New brick parameters. The only difference between this and Table 3.10 is that both the bar width, w, and the channel width, b, are now $0.05p$.

brick	D (mm)	ϕ (deg)
1	0	0
2	12	-20
3	50	67.3
4	25	-64

Table 3.12: Phase shift for each depth at 2000 Hz, where D is the additional distance a wave has to travel to reflect off of each block as compared to the tallest block, and ϕ is the associated phase shift between the incident and reflected waves.

brick	p (cm)	a_{tot} (cm)	N	ϕ (deg)	ϕ_{FEM} (deg)
2	2	1.4	9	-20	-19.7
3	2.4	0.7	9	67.3	65.5
4	2	0.5	6	-64	-64.2

Table 3.13: Brick parameters, where p is the height, a_{tot} is the width, N is the number of coils, ϕ is the target phase, and ϕ_{FEM} is the phase derived from the finite element simulation.

brick	f_{analyt} (Hz)	f_{FEM} (Hz)	$\Delta f_{/} f_{\text{analyt}}$
2	782	710	9%
3	1814	1700	6%
4	3276	3070	6%

Table 3.14: Comparison of the analytical and finite element resonance frequency of each brick and the percent error between these two models.

resonant frequencies are compared in Table 3.14. They match fairly well, with an error of less than 10%. Notice that brick 2 has the most absorption peaks, due to the fact that it has the longest effective length, which lowers the frequency of first resonance. For a quarter-wave resonator, resonance occurs at odd multiples of the quarter-wavelength, which explains the multiple peaks. It is curious that the absorption of brick 4 is less than the other bricks. Brick 4 has the least amount of coils, and thus has a more open structure than the other bricks, somewhat reminiscent of the Memoli brick design. It is possible that thermoviscous losses play a bigger much role in the absorption of the other bricks than brick 4.

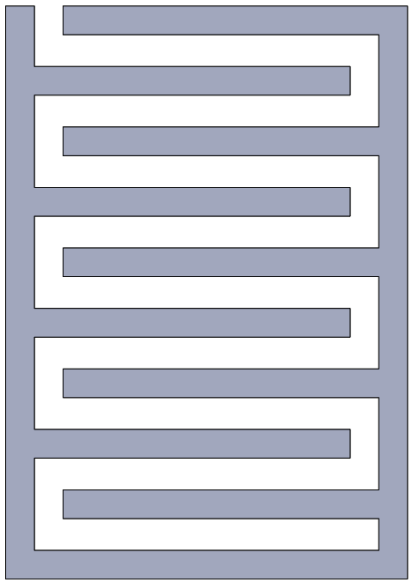

(a) Brick 2

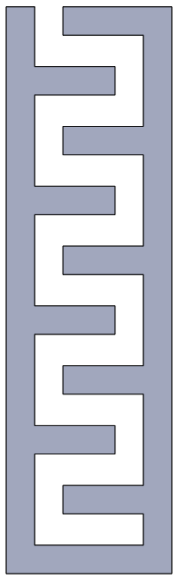

(b) Brick 3

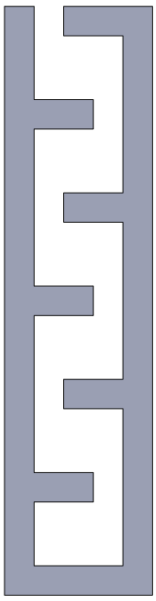

(c) Brick 4

Figure 3.40: Li Bricks 2-4. See Table 3.13 for brick parameters.

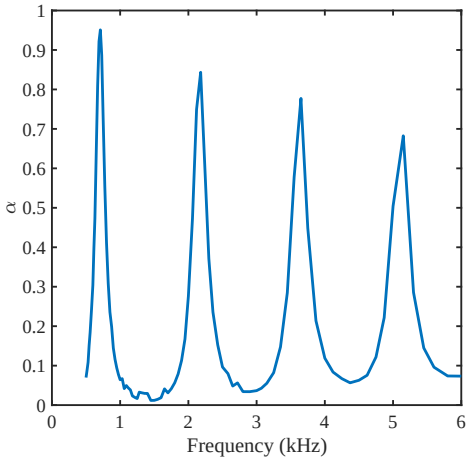

(a) Brick 2

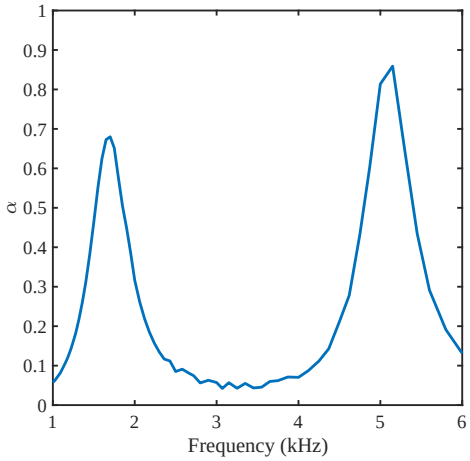

(b) Brick 3

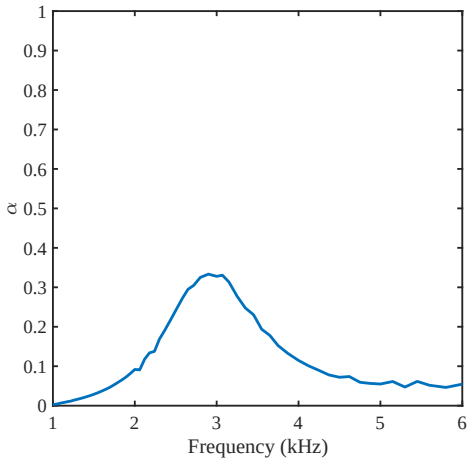

(c) Brick 4

Figure 3.41: Absorption, α vs frequency plots for bricks 2-4. Brick 2, shown in plot (a), has the greatest effective length and thus the most absorption peaks.

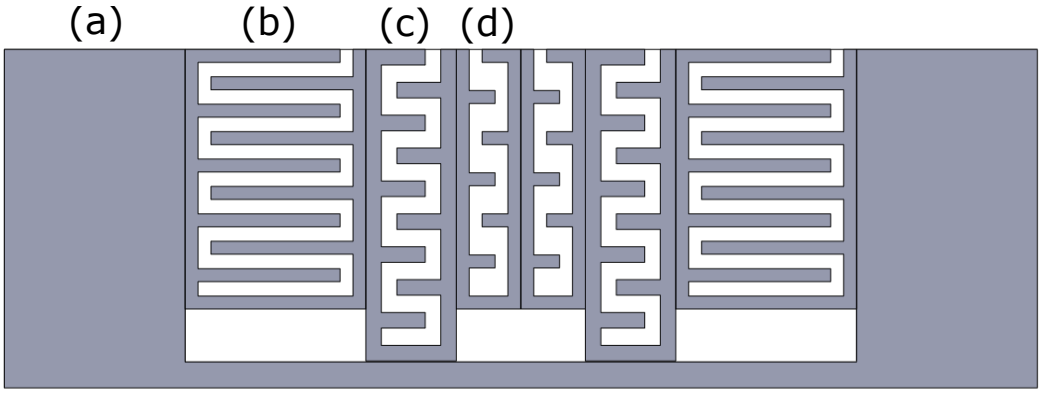

Figure 3.42: A cross section of a metamaterial brick QRD using Li's bricks, where (a) shows the rigid section that simulates the zero phase block of a standard QRD, and (b), (c), and (d) show bricks 2, 3, and 4, respectively. A rigid panel goes on either side of the bricks to create a rigid boundary on either side of the channels.

The next step was to simulate a metamaterial brick QRD and compare its response to that of a standard QRD. Unlike the Memoli brick QRD, this Li brick QRD replaces brick 1 with a rigid surface, instead of a straight open tube. This decision was made due to the fact that the bricks already produce almost perfection absorption at certain frequencies. Adding a straight tube as in the previous section, which is a quarter-wave resonator, would only produce more absorption. Thus, a rigid boundary was added to the each end of the brick QRD to simulate the zero phase QRD well. Figure 3.42 shows a cross section of the metamaterial QRD, Fig. 3.43 shows the full metamaterial QRD, and Fig. 3.44 shows the 3D COMSOL simulation used to measure the far field scattered SPL plots in Fig. 3.45, and the directivity plot in Fig. 3.46. Figure 3.45 was calculated using Eq. 3.1, and Fig. 3.46 was calculated using Eq. 3.2.

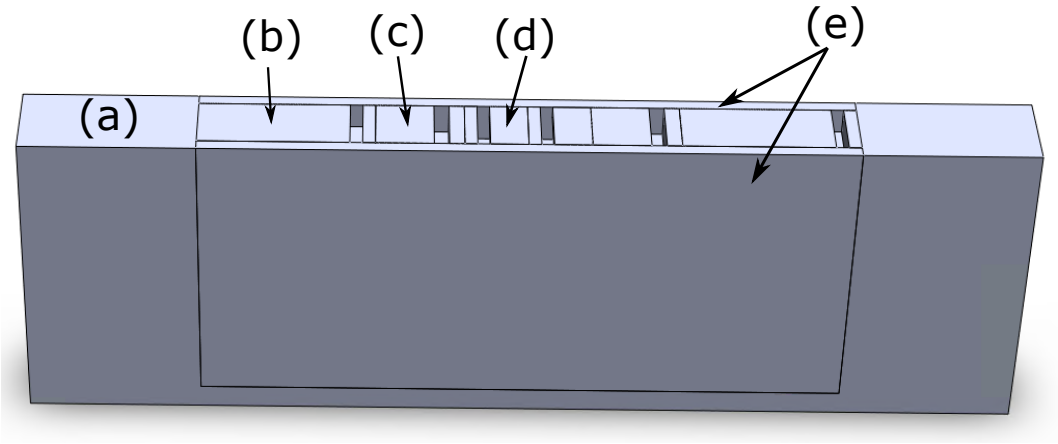

Figure 3.43: The full metamaterial Li brick QRD, where (a) is the rigid surface that corresponds to the zero phase well of the standard QRD. The geometries in (b), (c), and (d) are bricks 2, 3, and 4, respectively, and (e) shows the rigid panels on either side of the bricks.

The far field scattered SPL plots in Fig. 3.45 show that the Li brick QRD absorbs more of the energy of the incident wave, as the scattered pressure levels are around 20 dB lower that of the standard QRD. However, the Li brick QRD's scattered field is more evenly dispersed and does not suffer from the nulls and lobes of the standard QRD. Figure 3.46 more clearly shows this as the directivity of the standard QRD and the metamaterial brick QRD is compared for multiple frequencies.

While the Li bricks are unable to directly replicate the response of the QRD, they can still be a viable method of creating a metamaterial diffuser. Because these bricks have an approximate analytical solution for the phase of the reflected wave with an error of less than 10%, they can be easily designed. In addition, the geometry of the bricks allows them to achieve a full 2π radian

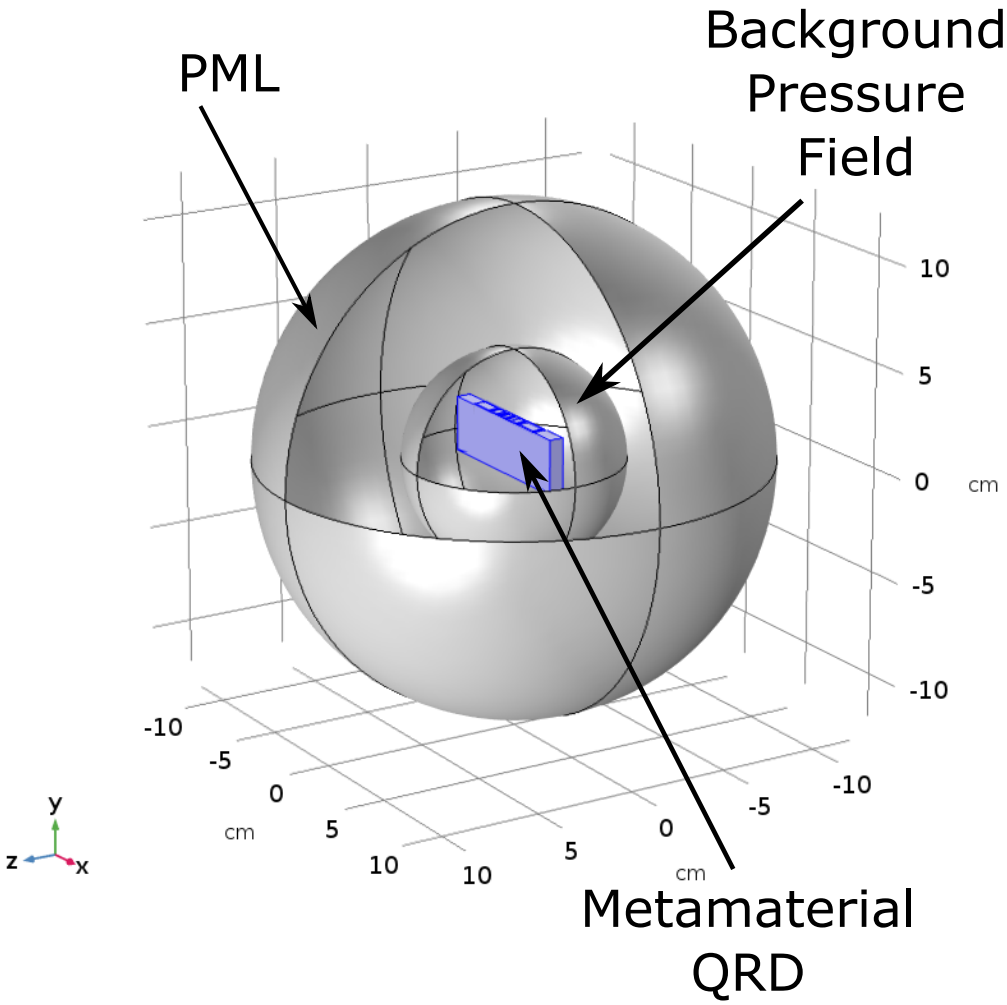

Figure 3.44: 3D metamaterial brick QRD simulation with three sections: perfectly matched layer, background pressure field, metamaterial brick QRD scatterer. The QRD is modeled with rigid boundaries and is suspended in free space for this model.

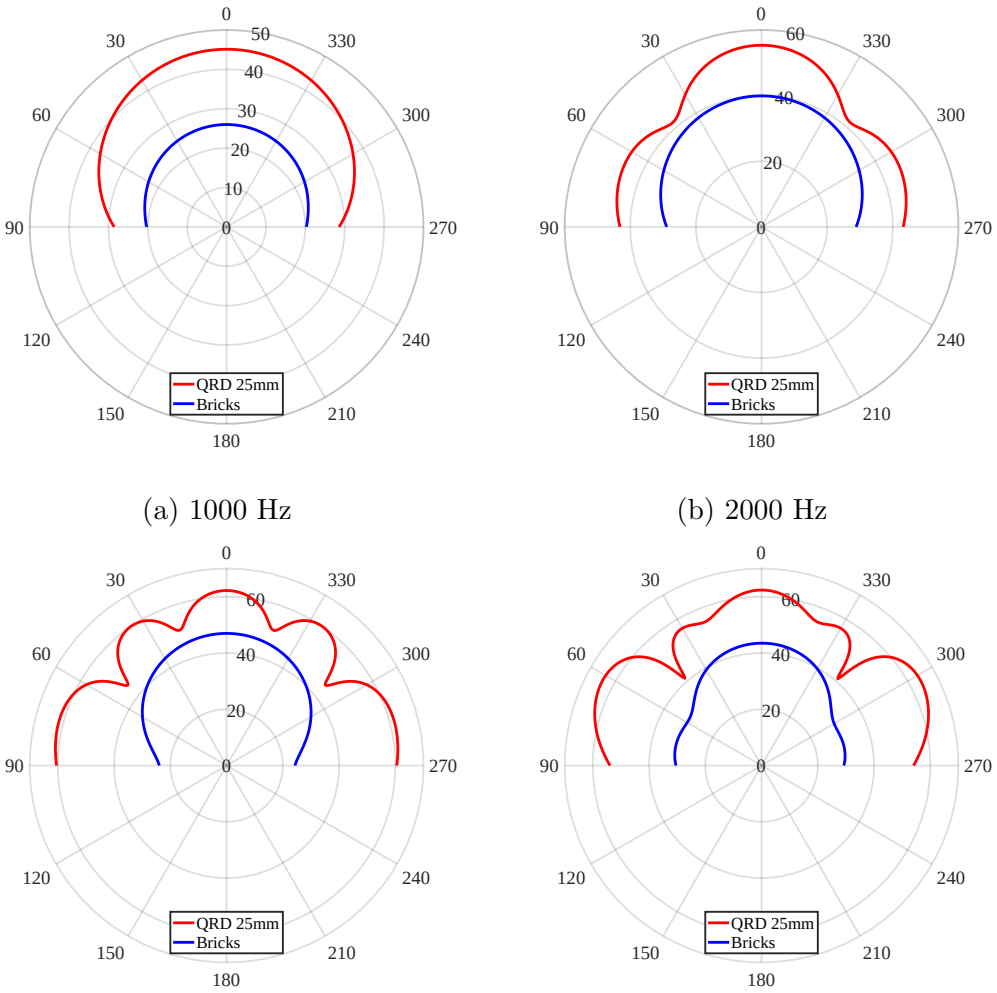

(a) 1000 Hz

(b) 2000 Hz

(c) 4000 Hz

(d) 5000 Hz

Figure 3.45: Far field scattered sound pressure level response of a standard N=7 QRD (25 mm width) and metamaterial brick QRD based on the design of Li et al. described in Table 3.13 at a design frequency of 2000 Hz. The radial grid is in units of dB re 20μPa.

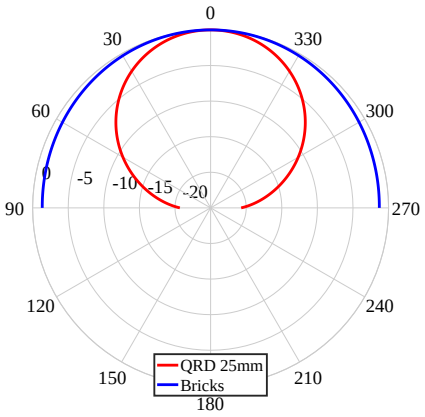

(a) 1000 Hz

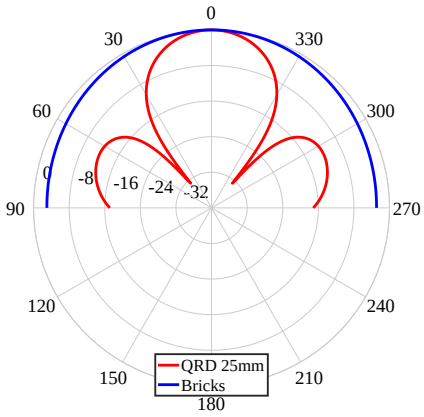

(b) 2000 Hz

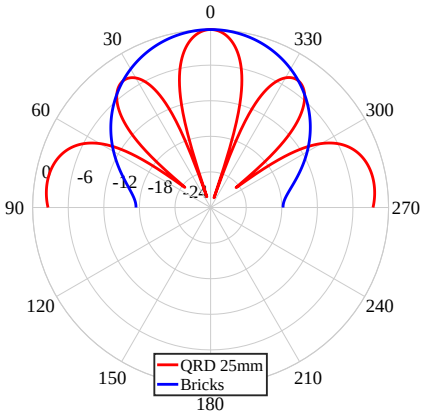

(c) 4000 Hz

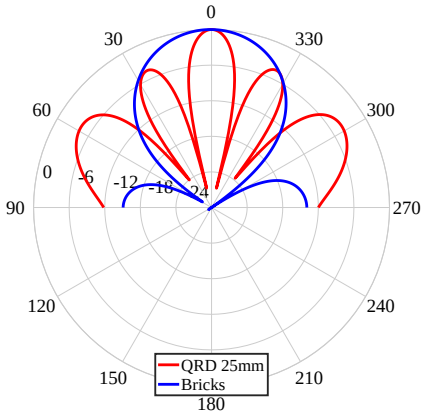

(d) 5000 Hz

Figure 3.46: Scattered field directivity plots (far field SPL of $P(\theta)$ normalized by $P_{\max}$ given by Eq. 3.2) of a standard N=7 QRD (25 mm width) and metamaterial brick QRD based on the design of Li et al. described in Table 3.13 at a design frequency of 2000 Hz. The radial grid is in units of dB.

phase shift when the depth is only 1/20th of the wavelength of the design frequency, which is significantly thinner than that of standard QRD. However, the downside to using the Li bricks to create a metamaterial QRD is that they have significant losses, as shown in Fig. 3.41 and Figs. 3.45. While this is a drawback in some cases, it may be beneficial for cases where both diffusion and absorption are desired.

3.4 Summary

Memoli et al. proposed a metamaterial brick that had a less tortuous internal geometry, and which were encoded with a specific transmitted wave phase delay. For the purposes of the researched outlined in this thesis, these bricks were then modified to encode a specific reflected wave phase delay and used to replicate the response of a 1D QRD. The metamaterial brick QRD and the standard QRD were then simulated using the commercial finite element software COMSOL. The far field scattered pressure results were compared and the metamaterial brick QRD arguably performed better, with less defined lobes and nulls. The metamaterial bricks were then experimentally tested in an impedance tube to determine the reflected field from each of the bricks, from which the magnitude and the phase of the reflected wave were extracted. The experimental and simulated results were compared, and it was determined that the bricks were acting like quarter-wave resonators, and thus the absorption was due to the quarter-wave resonance. While the simulation was unable to predict the significant amount of absorption observed in the experimental

results, the frequencies of absorption were predicted somewhat accurately, with errors ranging from 1% for the open bricks, and 12% for the more tortuous bricks.

To determine whether the 3D printed PLA material was causing the excess absorption, two aluminum bricks, one with a more open path, and one with a more tortuous path, were then simulated, fabricated, and tested. The aluminum brick results were compared against those of the 3D printed PLA bricks. The simulated PLA and aluminum bricks exhibited the same properties for both the open path and tortuous path bricks. While the experimental results for the aluminum bricks were also in excellent agreement with the simulated results for both the open and tortuous bricks, the experimental PLA results agreed only for the open bricks, with a significant error of 25% for the tortuous bricks. The cause of the error is thought to be in part due to the 3D printing process, which does not distribute the PLA material in a homogeneous manner throughout the structure. The COMSOL simulations used in this research are currently unable to account for this reality of the fabrication process. It is also possible that the 3D printing process changes the properties of the PLA material, causing the material properties used in the simulations to be inaccurate.

Due to the fact that the Memoli bricks lack an analytical solution, the resonance frequencies must be computed using finite element software, which can be tedious and computationally expensive. In addition, in order to induce the required phase change for a metamaterial diffuser, the height of the bricks

must be greater than that of standard QRD. Because the desire was to create a thinner diffusing surface, a decision was made to change designs to the Li brick design.

The Li bricks have an approximate analytical solution. Table 3.14 shows that the error between the resonance frequency predicted by the analytical model and the finite element simulation is less than 10%. This also allows them to be easily scalable to different design frequencies, as shown in Figs. 3.37 through 3.39. The Li bricks are also able to be designed with a height that is around 1/20th of the wavelength of the design frequency, which is smaller than the height of a standard QRD. Figure 3.45 shows that the Li brick QRD does not suffer from the nulls and lobes of the standard QRD, producing a more even scattered field.

Though neither metamaterial design is able to replicate the response of a standard QRD exactly, both designs show promise. In simulations, the metamaterial QRD based on Memoli's bricks more closely replicated the response of a standard QRD, and was able to overcome the lobes caused by the periodicity of the standard QRD by producing a more even scattering response. However, the geometry of the bricks dictates that the brick QRD must be taller than that of standard QRD at the same design frequency. Li's bricks are easier to design with the ability to calculate an analytical solution. They are also able to be made smaller than a standard QRD, thus creating a thinner diffusing surface. However, both designs suffer from inherent losses caused by the quarter-wave resonance. While this was not discussed in detail

in previous works of literature, it is likely that those designs also suffer from this drawback near resonance, since all resonant wall treatment systems lead to narrowband absorption.

Chapter 4

Conclusions and Future Work

This thesis has attempted to answer the question of whether acoustic metamaterials are viable replacements to typical acoustic surface treatments. Specifically, this thesis considers whether acoustic metamaterial diffusers are able to replicate the response of the QRD while solving its main issues: size and aesthetics. Because the size of the QRD is dependent on the design frequency, the QRD must be very large at low frequencies. In addition, the QRD uses the change in depth between the wells in a period to scatter the reflected wave. This creates an uneven surface, which may not fit in with the aesthetics of a room. Two coiled space metamaterial diffuser designs, one proposed by Memoli [21], and the other by Li [23] attempt to address these issues, while still replicating the response of the QRD.

A coiled space metamaterial diffuser was created using a design proposed by Memoli et al. [21]. The simulation results of this design, while not able to completely replicate the scattering of a standard QRD, showed that it was able to smooth out the scattered response of the standard QRD by producing less defined nulls and lobes. However, the design required for the metamaterial brick QRD to be taller than the standard QRD. Thus, the

metamaterial diffuser based on Memoli's design is unable to create a smaller, sub-wavelength diffuser. It is however, able to create a flat QRD that may better fit in with a room's aesthetics.

A coiled space metamaterial diffuser based on the design proposed by Li et al. [23] was also simulated. In contrast to Memoli's design, Li's design allowed for much smaller and thinner bricks, around 1/20th the wavelength of the design frequency. Like Memoli's design, it also allowed for a flat QRD. However, simulations showed that this design was unable to effectively replicate the scattered response of a standard QRD because it suffered from significant losses.

There is still much to be done to improve the accuracy of the simulations and definitively answer whether either of these designs are viable options to replace the standard QRD. Due to time constraints, a number of tasks were unable to be completed in time for the writing of this thesis. These tasks are detailed below and suggested as future work.

1. **Improve finite element model so that it more closely matches the results of the experiments.**

   An accurate model is important. Models are useful tools that allow for quick measurements and comparisons, but they must be validated experimentally to ensure that they are accurately predicting real world environments. As shown in Chapter 3.2.2, the simulation is able to predict the correct resonance frequency, but not the magnitude of absorption at

those frequencies. The model should be improved so that it can accurately predict both the resonance frequency and the level of absorption at that frequency.

2. **Determine the source of the error between the 3D printed PLA bricks and the aluminum bricks.**

   As shown in Figs. 3.29 through 3.31, the measured frequency of peak absorption for the 3D printed PLA bricks differs significantly from that of the simulations and the aluminum bricks. The source of this error is thought to be caused by the 3D printing process, which may change the PLA material properties. Printed parts also contain an inhomogeneous structure, which may create resonances within the structure of the brick itself and make it behave differently than a solid void-free part made out of homogeneous PLA. This should be investigated further, as the ability to create bricks using the 3D printing process that are functionally the same as aluminum bricks saves a significant amount of time and is significantly cheaper.

3. **Conduct experimental impedance tube testing on the Li bricks, similar to those conducted on the Memoli bricks, to determine the accuracy of those simulations.**

   Once the PLA bricks have been improved so that their response matches those of the aluminum bricks, the Li bricks can be 3D printed and tested experimentally in the impedance tube to determine the accuracy of the

simulations. The tests conducted would be similar to those conducted on the Memoli bricks.

4. **Experimentally compare the scattered response of a 1D standard QRDs to the scattered response of a 1D Memoli brick QRD.**

   While the simulated scattered response of a 1D QRD is compared to that of a 1D Memoli brick QRD and the Li brick QRD, these have not been validated experimentally. If the source of the error between the PLA and aluminum bricks has been corrected and the model further validated, the experiment can be conducted using only the 3D printed bricks, and the results compared against those of the simulations for both metamaterial brick QRDs.

5. **Experimentally compare the scattered field of a 2D standard QRD to that of a 2D metamaterial brick QRD.**

   Once the 1D QRDs have been validated, the 2D QRDs can be simulated in COMSOL, fabricated, and experimentally tested. The results for the simulations should be compared against the experimental results of both the brick QRDs and the standard QRD. Then, the results for each metamaterial brick QRD should be compared against that of the standard QRD, and against the other.

Bibliography

[1] D. T. Blackstock, *Fundamentals of Physical Acoustics*. John Wiley & Sons, New York, 2000.

[2] D. J. R. Andrade, "Acoustic comfort in an auditorium for 100 people." [Online]. Available: http://danielpok13192.pbworks.com/w/page/115658392/Acoustics%202

[3] T. Cox and P. D'Antonio, *Acoustic Absorbers and Diffusers: Theory, Design and Application*. Spon Press, Taylor & Francis Group, London and New York, 2004.

[4] M. Long, *Architectural Acoustics*. Elsevier, San Diego, 2006.

[5] T. Cox and P. D'Antonio, *Acoustic Absorbers and Diffusers: Theory, Design and Application*, 3rd ed. CRC Press, Taylor & Francis Group, Boca Range, FL, 2016.

[6] M. R. Haberman and M. D. Guild, "Acoustic metamaterials," *Physics Today*, vol. 69, no. 6, pp. 42–48, 2016.

[7] M. R. Haberman and A. N. Norris, "Acoustic metamaterials," *Acoustics Today*, vol. 12, no. 3, pp. 31–39, 2016.

[8] G. Ma and P. Sheng, "Acoustic metamaterials: From local resonances to broad horizons," *Science Advances*, vol. 2, no. 2, p. e1501595, 2016.

[9] S. H. Lee, C. M. Park, Y. M. Seo, Z. G. Wang, and C. K. Kim, "Composite acoustic medium with simultaneously negative density and modulus," *Physical Review Letters*, vol. 104, no. 5, p. 054301, 2010.

[10] A. N. Norris, "Acoustic cloaking," *Acoustics Today*, vol. 11, no. 1, pp. 38–46, 2015.

[11] R. Fleury and A. Alù, "Cloaking and invisibility: A review," in *Forum for Electromagnetic Research Methods and Application Technologies (FERMAT)*, vol. 1, no. EPFL-ARTICLE-223081, 2014.

[12] Y. Li, B. Liang, X. Tao, X.-f. Zhu, X.-y. Zou, and J.-c. Cheng, "Acoustic focusing by coiling up space," *Applied Physics Letters*, vol. 101, no. 23, p. 233508, 2012.

[13] A. S. Titovich, A. N. Norris, and M. R. Haberman, "A high transmission broadband gradient index lens using elastic shell acoustic metamaterial elements," *The Journal of the Acoustical Society of America*, vol. 139, no. 6, pp. 3357–3364, 2016.

[14] R. Ghaffarivardavagh, J. Nikolajczyk, R. G. Holt, S. Anderson, and X. Zhang, "Horn-like space-coiling metamaterials toward simultaneous phase and amplitude modulation," *Nature Communications*, vol. 9, no. 1, p. 1349, 2018.

[15] Y. Xie, B.-I. Popa, L. Zigoneanu, and S. A. Cummer, "Measurement of a broadband negative index with space-coiling acoustic metamaterials," *Physical Review Letters*, vol. 110, no. 17, p. 175501, 2013.

[16] M. Yang, S. Chen, C. Fu, and P. Sheng, "Optimal sound-absorbing structures," *Materials Horizons*, vol. 4, no. 4, pp. 673–680, 2017.

[17] Y. Li and B. M. Assouar, "Acoustic metasurface-based perfect absorber with deep subwavelength thickness," *Applied Physics Letters*, vol. 108, no. 6, p. 063502, 2016.

[18] C. Zhang and X. Hu, "Three-dimensional single-port labyrinthine acoustic metamaterial: Perfect absorption with large bandwidth and tunability," *Physical Review Applied*, vol. 6, no. 6, p. 064025, 2016.

[19] Y. Zhu, X. Fan, B. Liang, J. Cheng, and Y. Jing, "Ultrathin acoustic metasurface-based schroeder diffuser," *Physical Review X*, vol. 7, no. 2, p. 021034, 2017.

[20] N. Jiménez, T. J. Cox, V. Romero-García, and J.-P. Groby, "Metadiffusers: Deep-subwavelength sound diffusers," *Scientific Reports*, vol. 7, no. 1, p. 5389, 2017.

[21] G. Memoli, M. Caleap, M. Asakawa, D. R. Sahoo, B. W. Drinkwater, and S. Subramanian, "Metamaterial bricks and quantization of metasurfaces," *Nature Communications*, vol. 8, p. 14608, 2017.

[22] W. T. Chu, "Transfer function technique for impedance and absorption measurements in an impedance tube using a single microphone," *The Journal of the Acoustical Society of America*, vol. 80, no. 2, pp. 555–560, 1986.

[23] Y. Li, B. Liang, Z.-m. Gu, X.-y. Zou, and J.-c. Cheng, "Reflected wavefront manipulation based on ultrathin planar acoustic metasurfaces," *Scientific Reports*, vol. 3, p. 2546, 2013.

[24] J. A. Huwaldt, "Plot digitizer," October 2015. [Online]. Available: http://plotdigitizer.sourceforge.net/